SHARC Buoy

Robust firmware design for a novel, low-cost autonomous platform for the Antarctic Marginal Ice Zone in the Southern Ocean

Jamie Nicholas Jacobson

Department of Electrical Engineering
University of Cape Town
Rondebosch, Cape Town
South Africa

March 2021

MSc.(Eng.) thesis submitted in partial fulfilment of the requirements for the degree of MSc. in Electrical Engineering in the Department of Electrical Engineering at the University of Cape Town

Keywords: IoT; Firmware; Southern Ocean; Sea Ice; Remote Sensing; Autonomous; Platform

Declaration

I, Jamie Nicholas Jacobson, hereby:

1. grant the University of Cape Town free licence to reproduce the above thesis in whole or in part, for the purpose of research;
2. declare that:
   (a) this thesis is my own unaided work, both in concept and execution, and apart from the normal guidance from my supervisors, I have received no assistance except as stated in my bibliography and acknowledgements.
   (b) neither the substance nor any part of the above thesis has been submitted in the past, or is being, or is to be submitted for a degree at this University or at any other university.

Jamie Nicholas Jacobson

Department of Electrical Engineering
University of Cape Town

Saturday 6th March, 2021

Abstract

SHARC Buoy

Jamie Nicholas Jacobson

Saturday 6th March, 2021

Sea ice in the Antarctic Marginal Ice Zone (MIZ) plays a pivotal role in regulating heat and energy exchange between oceanic and atmospheric systems, which drive global climate. Current understanding of Southern Ocean sea ice dynamics is poor with temporal and spatial gaps in critical seasonal data-sets. The lack of in situ environmental and wave data from the MIZ in the Antarctic region drove the development of UCT's first generation of in situ ice-tethered measurement platform as part of a larger UCT and NRF SANAP project on realistic modeling of the Marginal Ice Zone in the changing Southern Ocean (MISO). This thesis focuses on the firmware development for the device and the design process taken to obtain key measurements for understanding sea ice dynamics and increasing sensing capabilities in the Southern Ocean.

The buoy was required to survive the Antarctic climate and contained a global positioning system, temperature sensor, digital barometer and inertial measurement unit to measure waves in ice. Power was supplied to the device by a power supply unit consisting of commercial-grade batteries in series with a temperature-resistant low dropout regulator, and a power sensor to monitor the module. A satellite modem transmitted data through the Iridium satellite network. Finally, flash chips provided permanent data storage. Firmware and peripheral driver files were written in C for an STMicroelectronics STM32L4 ARM-based microcontroller. To optimise the firmware for low power consumption, inactive sensors were placed in power-saving mode and the processor was put to sleep during periods of no sampling activity.

The first device deployment took place during the SCALE winter expedition in July 2019. Two devices were deployed on ice floes to test their performance in remote conditions. However, due to mechanical and power errors, the devices failed shortly after deployment. A third device was placed on the SA Aghulas II and successfully survived for one week while continuously transmitting GPS coordinates and ambient temperature. The second generation featured subsequent improvements to the mechanical robustness and sensing capabilities of the device. However, due to the 2020 COVID-19 pandemic, subsequent Antarctic expeditions were cancelled resulting in the final platform evaluation taking place on land. The device demonstrates a proof of concept for a low-cost, ice-tethered autonomous sensing device however, additional improvements are required to overcome severe bandwidth and power constraints.

Acknowledgements

The creation of this work would not be possible without the contributions of the following people:

Keith Machuchon for designing the buoy stand and for offering insight into past deployments with the trident buoy.

Do Yeou Ku for developing the circular buffer algorithm and for all her advice which helped guide the development of the firmware into its current form. Additionally, thank you to Tilen Majarle of https://stm32f4-discovery.net/ whose tutorials and guides helped with the initial stages of firmware development. I would also like to acknowledge the driver code for the MPU6050 IMU written by Adafruit in C++ for the Arduino which provided the basis for the STM32L4 driver code in C.

Yusuf Heylen for contributing towards development and integration of the IMU.

Nicholas Bowden for creating the C library for the Flash chips.

Jason Cloete for developing the circuit board for the first prototype of the device.

Ben Adey for his work on developing a power budget for the system.

Anran Chen for his contribution towards developing a compression algorithm for raw inertial time-series data.

James Irvine and Hannah Harrison-Saayman for their contribution towards testing the current monitor and flash chips.

Michael Noyce for his work on developing an integrated PCB for future versions of the project.

Robyn Verrinder and Justin Pead for designing the prototype circuit boards for the first version of the device.

Thank you to my supervisors Robyn Verrinder, Amit Mishra and Marcello Vichi whose insight and wisdom help guide this project to fruition.

To Jarryd Son and Nadir Vorajee who initated the project and helped guide me through the initial phases.

Thank you to the UCT-UDE sea ice team for teaching me about the importance of sea ice in an ever changing climate. Also special mention to Ehlke Hepworth and Ashley

Womack for their role in deploying the buoys. Also to Sebastian Skatulla for leading the sea ice team and helping coordinate the SHARC Buoy activities. I'd also like to thank Marc de Vos from the SAWS for his insight and input that guided the project.

Thank you to the UCT mechnatronics lab for giving me the support, assistance and friendships that got me through the long development process.

To Sasha Gold for always supporting me and helping me when I need it. To Joseph Miller; your friendship helped lift me up when I was down.

To my family for supporting me and putting up with rooms and tables filled with cluttered hardware. You all gave me the strength to undertake this project.

Finally, a project would not be complete without coffee and people to drink it with. For that I'd like to thank Charlie Lin for sharing in this journey from start to finish.

The financial assistance of the National Research Foundation (NRF) towards this research is hereby acknowledged. Opinions expressed and conclusions arrived at, are those of the author and are not necessarily to be attributed to the NRF.

Dedicated to the captain and crew of the SA Aghulas II whose bravery and wit helped bring science to the edge of the earth and back.

Contents

List of Figures

List of Tables

Chapter 1

Introduction

1.1 Background to investigation

1.1.1 Antarctic sea ice and the Marginal Ice Zone

Antarctica plays host to ocean-atmospheric processes, which are significant drivers of global climate. These interactions are strongly influenced by sea ice coverage and extent, which acts as a boundary layer between the atmosphere and ocean (Parkinson, 2004). Sea ice reflects incoming solar radiation which, otherwise, would be absorbed by the ocean influencing ocean temperature and salinity (Parkinson, 2004). Additionally, sea ice expanse has been shown to insulate the ocean and reduce evaporation while regulating heat flux, and gaseous exchange (DeConto & Pollard, 2003) providing a stable habitat for the diverse ecosystem that inhabits the region (Arrigo & Thomas, 2004) (see Figure 1.3). Sea ice provides a damping effect on oceanic kinetic energy as it regulates the mass and movement of waves around the Southern Ocean (Parkinson, 2004; Roach et al., 2020). High winds, cyclone frequency and prominent wave activity perturbs the ice preventing it from congealing at the ocean edge. This result in a region of semi-consolidated ice masses known as the Marginal Ice Zone (MIZ) (Wadhams et al., 1987).

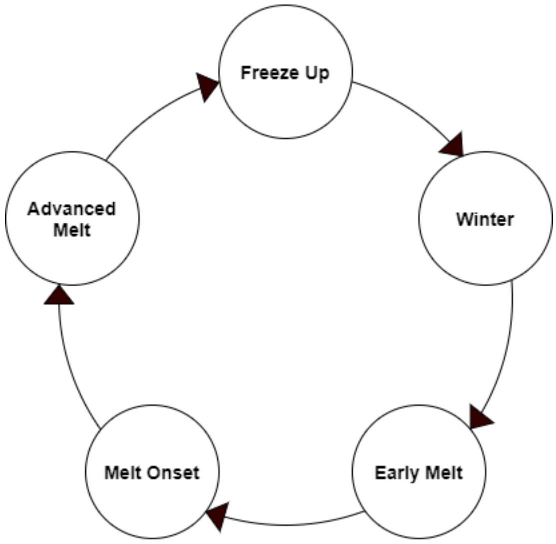

Figure 1.1: Diagram showing the lifecycle of Antarctic sea ice as observed using remote sensing based on Barber (2005). The cycle begins with the congealing of the ocean surface known as Freeze Up with peak ice formation during Winter, the second half of the cycle is characterised by various stages of melt with complete sea ice retreat occurring in the Summer.

Sea ice formation in the Southern Ocean begins when the surface layer of the ocean congeals causing ice crystals to form. These crystals combine to form frazil ice; the concentration of which increases as the heat from the ocean is removed by the atmosphere (Arrigo & Thomas, 2004). As the wind and wave activity begin to calm, frazil ice combines into grease ice, which grows into pancake ice floes (Arrigo & Thomas, 2004). This growth period is known as "freeze-up" and forms the first stages of the sea ice life cycle (Barber, 2005). Additionally, strong winds in the Marginal Ice Zones cause the floes to drift over long distances (Alberello et al., 2019). These winds, coupled with high ice floe density result in collisions between floes causing them to break apart (Steer et al., 2008) resulting in brash ice (Carsey, 1992). During the winter months, newly formed ice grows a layer of snow (Barber, 2005) and is termed "first year ice"[1]. Brine is present between the ice fragments and the layer of snow is affected by the level of precipitation (Barber, 2005).

[1] First year ice is newly consolidated ice that has been growing for less than one winter's growth period (Carsey, 1992).

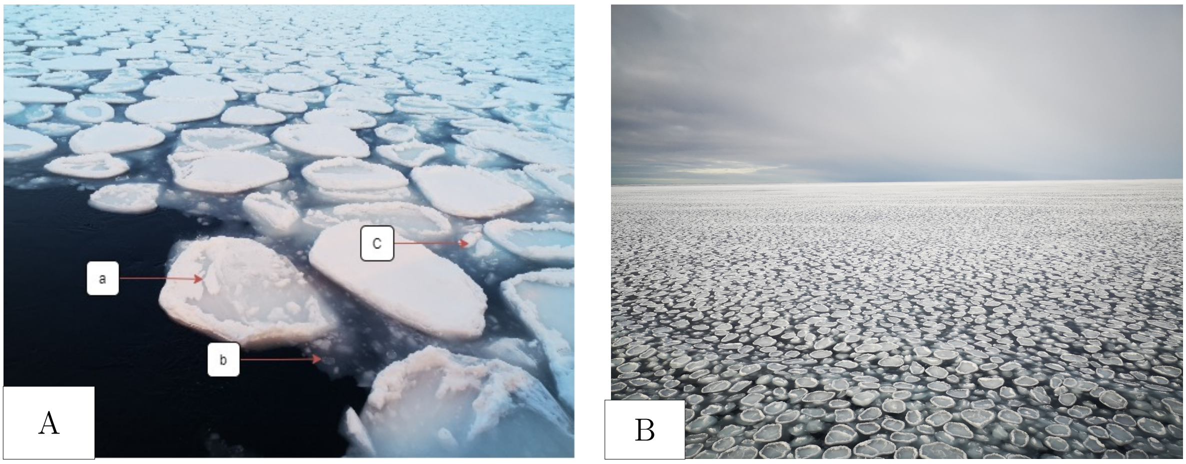

Figure 1.2: (A) Diagram showing different types of ice present in the Marginal Ice Zone including (a) pancake ice floes (b) frazil ice and (c) brash ice. Some ice floes exhibit snow growth along the ridges while other floes exhibit flooding. Photo taken from the SCALE 2019 winter expedition during the early sea ice formation period by the author. (B) Sea ice in the Southern Ocean MIZ during July 2019, where pancake ice is the predominant concentration while brash ice is the smallest. Swell waves can also be observed propagating through the region. Photo taken during the early sea ice formation period during the SCALE winter cruise July 2019 by the author.

Finally, the seasonal cycle closes with three phases of melting. Early melt marks the transitional period where moisture is continuously present in snow cover on the sea ice (Barber, 2005). The level of moisture in the snow increases through "melt-onset" brought on by the transition from summer to winter and increasing ocean/atmospheric temperatures (Barber, 2005). Eventually, the snow and ice surface begin to melt rapidly during the "advanced melt" phase resulting in complete desalination of the ice floes followed by the breaking up of the sea ice sheets (Barber, 2005).

The result of these processes is a region of semi-consolidated ice, which extends an estimated 19 million km^2 from the Antarctic continent (Maksym et al., 2012). These ice floes increase in size through gradual heating, fusing the floes into packed ice (Arrigo & Thomas, 2004). Sea ice concentration in the MIZ covers an observed range of 100% of total ice concentration from summer to winter (Alberello et al., 2019). However, Alberello et al. (2019) further show that this cover is an unconsolidated mixture of different ice types rather than a single ice cover therefore showing that this metric may not represent the true concentration of sea ice on a high resolution scale. The variability of the MIZ, coupled with the strong storms and weather patterns, drive the strongest atmospheric-ocean-sea ice interactions in the region. Alberello et al. (2019) further highlight that knowledge of MIZ sea ice dynamics is required to model the response to storms as well as predict the regional response to changes in climate.

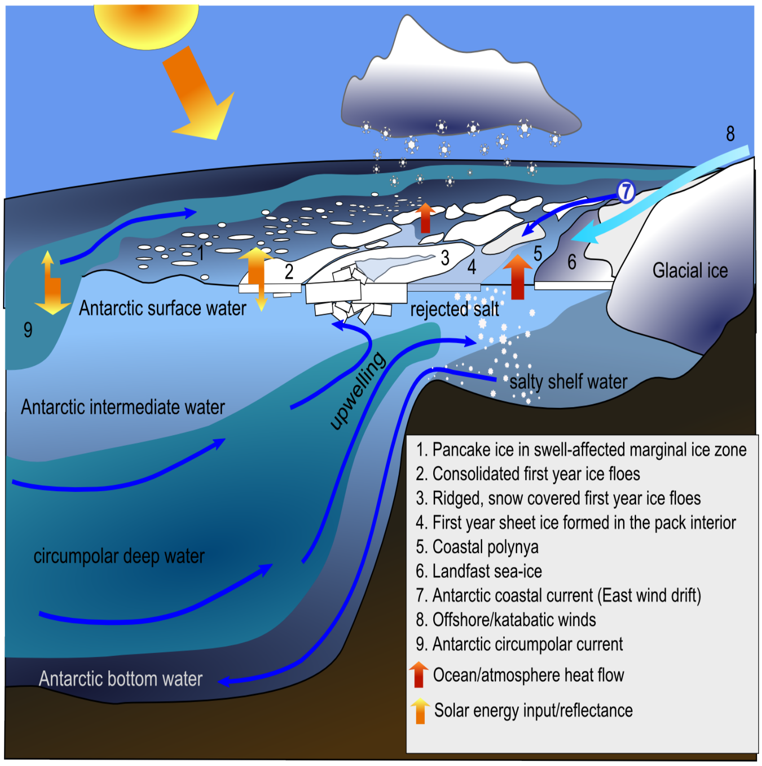

Figure 1.3: Diagram showing the expanse of sea ice in the Southern Ocean. Packed ice forms closer to the continent in calmer conditions while strong oceanic currents, winds, wave action and extreme temperatures result in the formation of semi-consolidated ice in the marginal ice zone (1 to 5). Here, ice formation is highly seasonal expanding to a maximum in winter and retreating to a minimum in summer. Sea ice acts as a boundary layer influencing heat and gaseous exchange between the atmosphere and ocean. Figure taken from Steer (2016).

1.1.2 Observations of the Marginal Ice Zone

Antarctic sea ice has gained recognition for playing a critical role in global climate systems (Kennicutt et al., 2016). There has been growing interest by the global scientific community in Antarctic research since the first International Polar Years (Kennicutt et al., 2016). International collaborations have sought to formalise Antarctic Research and unite efforts under common goals (Kennicutt et al., 2016) with the formation of the Scientific Committee on Antarctic Research (SCAR), which has resulted in increased sampling in the MIZ. However, data from the marginal and packed ice zones are under-sampled and poorly represented (Vichi et al., 2019). Very little in situ data exist to fully understand the environmental conditions surrounding the key metamorphic phases of sea ice in the Antarctic MIZ. Current climate models and observations exist based on data sets from the Arctic (Vichi et al., 2019), which, when applied to Antarctic sea ice, fail to accurately capture the dynamics of the region on a high-resolution scale. Sea ice expeditions have traditionally taken place during the summer months when the sea ice extent is at a minimum (Kennicutt et al., 2016). This results in temporal and spatial gaps in seasonal measurements, which fail to characterise sea ice expanse during the fundamental formation periods (Maksym et al., 2012). Additionally, these data are critical for understanding

Southern Ocean sea ice dynamics and observed phenomenon in the Marginal Ice Zone such as waves-in-ice (Kohout et al., 2014). Furthermore, polar oceanic and atmospheric measurements are critical for understanding the local climates since the high cyclonic activity in the region affects the heat and moisture delivery to higher latitudes (Vichi et al., 2019).

Almost all data collected from in situ measurements in the region are taken during seasonal manned expeditions. Only 22 countries have access and shipping capabilities to initiate expeditions to the region. Additionally, these expeditions require vast resources and complex logistical operations. Furthermore these missions are time sensitive and cancelled expeditions create gaps in seasonal data sets. The harsh seasonal climate causes certain, vital areas of the MIZ and packed ice zones to become inaccessible during winter months. As a result, missions only occur during certain seasons resulting in temporal gaps. Attempts have been made to fill in these gaps using data from Arctic climate programs e.g. Lee et al. (2012). However, these attempts fail to characterise the region and accurately capture seasonal variability. For example, in 2016, an anomaly in the sea ice extent was detected where the ice retreated 48% faster than the mean rate (Turner et al., 2017). Vichi et al. (2019) have shown the region to be a hot-spot for cyclonic activity, which regularly impacts ice formation within the marginal ice zone. However these interactions are not captured by current climate models (Vichi et al., 2019).

Figure 1.4: Photo taken in the Marginal Ice Zone from on-board the SA Aghulus II during the SCALE winter expedition in 2019 by the author. The vessel is anchored in consolidated ice with the UCT [2]-UDE[3]sea ice team performing ice coring activities on the surface of the ice.

Therefore, a call to increase sensing in the region has arisen to fill in the gaps of these temporal data sets (Kennicutt et al., 2019). A review by Kennicutt et al. (2016) highlights a need to revolutionise Antarctic science to overcome these challenges. As part of the plan, SCAR identified technology as playing a pivotal role in Antarctic research. Air, sea and space-borne technologies can replace manned-expeditions which can provide in

[2]University of Cape Town
[3]University of Duisburg-Essen

situ monitoring on a macro and micro scale (Kennicutt et al., 2016). Technology can provide a potential solution to long-term monitoring. Robust, power-efficient solutions that are capable of performing long-term functions in a non-invasive manner are required to reduce the need for implementing new infrastructure.

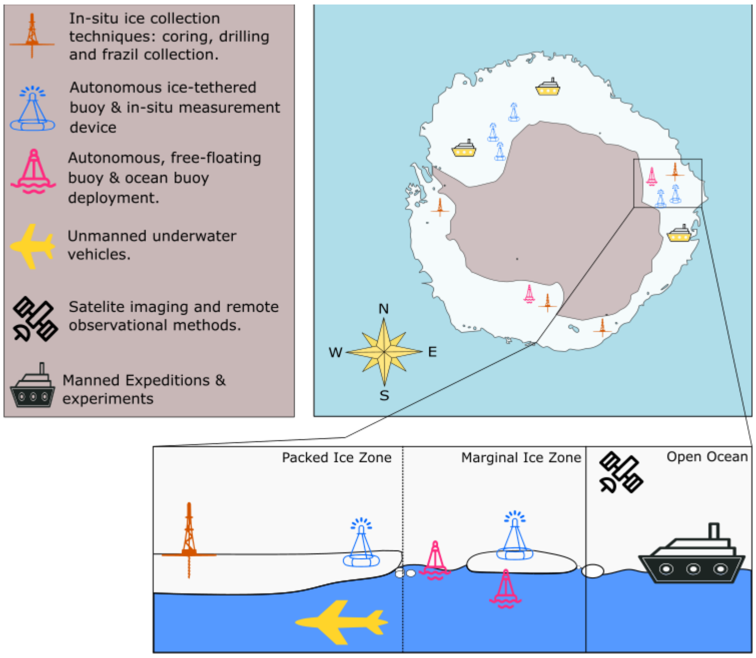

Figure 1.5: Diagram showing the current state of Antarctic sea ice measurement technologies for each level of observation as well as the estimated deployment location. Diagram taken when sea ice extent is at a maximum. This diagram is derived from the technology implementation strategy identified from the 2016 SCAR roadmap (Kennicutt et al., 2019)[4] and has been adapted to show sea ice observational techniques.

1.1.3 Overview of the existing technology and devices

Modern technology has seen an increased use in remote monitoring of the continent (Kennicutt et al., 2016). For example, satellite imaging is the most prevalent technology for monitoring sea ice in both the Arctic and Antarctic regions. It provides large-scale mapping of sea ice extent, thickness, snow cover at the cost of a low spatial resolution (Alberello et al., 2019; Galin et al., 2011; Turner et al., 2017). These techniques allowed for the detection of the rapid sea ice retreat recorded in 2016 (Turner et al., 2017) and are very useful for large-scale representation. However, satellite imaging is severely constrained by its resolution (Emery et al., 1997). Pixel sizes of synthetic aperture radar (SAR) images are in the order of 10 to 100 m (Galin et al., 2011) where, for example, snow thickness can vary down to the cm. Furthermore, cloud cover can compromise the measurements resulting in missing data. Finally, these measurements require validation against data models, which tend to underrepresent climate in the region (Emery et al.,

[4]Figure made using icons from Flaticon.com, Buoy by hunotika from the Noun Project, oil rig by Mourad Mokrane from the Noun Project, Plane by jokokerto from the Noun Project.

1997; Galin et al., 2011). Hence, a need arises for the development of in situ technology that can provide accurate, detailed information down to the highest possible resolution and allow for long term, large scale monitoring of ocean-ice-atmosphere processes. Hence we turn to autonomous platforms as a solution.

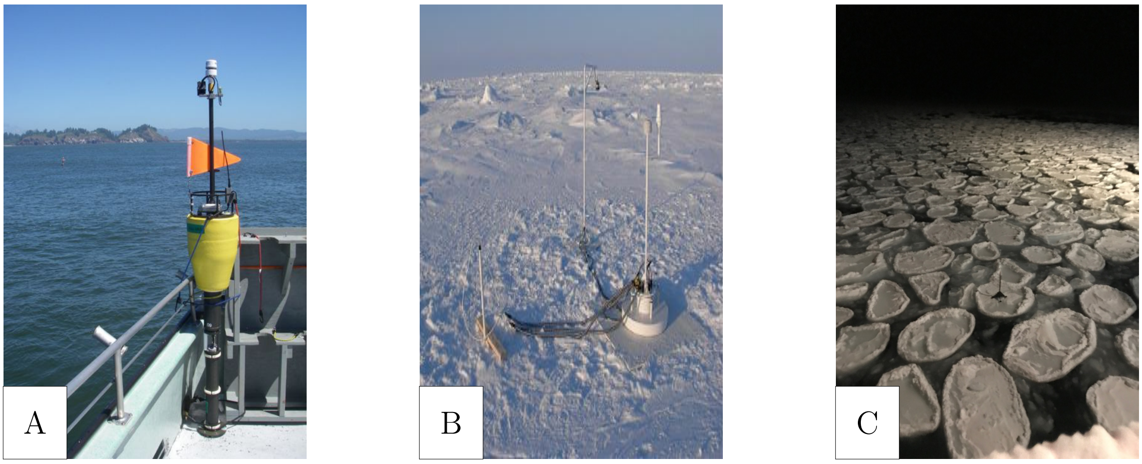

Figure 1.6: Practical examples of instruments used to collect in situ measurements in the sea ice region. These comprise: (A) the Surface Wave Instrument Float Tracking (SWIFT) buoy developed by the University of Washington (Thomson, 2012); (B) the Ice Mass Balance (IMB) buoy developed by Dartmouth College [(Planck et al., 2019) image source: (USACE, 2014)]; and (C) the Southern Hemisphere Antarctic Research Collaborative (SHARC) buoy developed by the University of Cape Town (photo courtesy of R. Verrinder).

Delivering a remote system capable of long-term functionality is a high priority for Antarctic science (Kennicutt et al., 2016) and will accrue robust, reliable, time-sensitive data-sets to populate these models. This will bring climate models in line with current observations and will allow for a quantified, thorough description of a local phenomenon, for example, the role of ocean swells in ice formation in the Marginal Ice Zone (Doble & Bidlot, 2013; Doble et al., 2017). A successful system should have the following characteristics[5]:

1. Autonomous or sustained deployment capabilities
2. Adequate remote sensing capabilities
3. Improved, robust power supplies
4. Real-time data collection, transfer and analysis
5. Survivable under extreme weather conditions

However, the current state of modern Antarctic observational technology is underdeveloped; current prototypes are too expensive and difficult to obtain by the scientific community (Kennicutt et al., 2016). Many institutions have initiated projects to develop

[5]Taken from a collective survey distributed during the Antarctic Roadmap Challenge in 2016 (Kennicutt et al., 2016).

autonomous systems such as buoys (examples shown in Figure 1.6) and unmanned surface vehicles (USVs) such as Wave Gliders (Liquid Robotics, 2016), which have been utilised successfully in Antarctic and Arctic oceanographic studies (Swart et al., 2020). For example, SWIFT buoys deployed in the Arctic Marginal Ice Zone were used to validate Marine Radar measurements of sea ice drift in the Beaufort Sea (Lund et al., 2018). However, these systems are extremely niche and require a technical crew to deploy and retrieve the buoys. The devices are generally proprietary with fixed sets of sensors and fewer sensing capabilities rendering the device inflexible to the needs of scientists (Rabault et al., 2017). Rabault et al. (2019) note the growing use of open source hardware and off-the-shelf technology in modern systems. Off-the-shelf components have reached a state where the components are well documented and specified to withstand the requirements for polar systems (Rabault et al., 2019). Open-source hardware has allowed for the free exchanging of designs allowing scientists to build their own devices without needing to design and test prototypes (Rabault et al., 2019). As a result, there has been a growth in literature on open access devices with designs and code bases readily available on code sharing sites such as GitHub[6]. Hence, inclusion of cost-effective technology as a solution is a growing trend.

Additionally, these devices have shown promise in the field. Rabault et al. (2019) developed an open-source multi-sensing autonomous system and Kohout et al. (2015) developed a multi-sensing system with off-the components. The devices were deployed in the Arctic and Antarctic Marginal Ice Zones. The buoys developed by Kohout et al. (2015) encountered technical issues resulting in a total of 39 days survivability with two buoys lost immediately after deployment, one buoy surviving for nine days and another for 17.5 days (Kohout et al., 2015). The devices were deployed again in the Ross Sea by Kohout et al. (2020) in April 2020 where a buoy lasted for 66 days (Kohout et al., 2020). The buoys developed by Rabault et al. (2019) included solar panels to recharge the batteries. However these systems survived for only 12 days during the spring. Other systems deployed in the region are the MetOcean buoys (Metocean, 2016), Surface Wave Instrument Float Tracking (SWIFT) (Thomson, 2012) buoys and Trident buoys (Trident Sensors, 2021). These systems, however, are expensive and do not have the sensing capabilities specifically for sea ice dynamics. Full details of these remote sensing technologies are discussed later in Chapter 2. Consequently, this presents a problem for in situ sea ice observations in that multiple systems are required to collect desired data for models with a need for back up systems in case of failure.

Therefore we are presented with a unique opportunity to design a series of novel ice-tethered autonomous systems to increase remote sensing at an affordable rate. The goal of the project is to design a proof of concept system with expandable, modular capabilities capable of running off a single power module for seasonal periods and part of the South African National Antarctic Programme (SANAP), and it is led by the Marine and Antarctic Research centre for Innovation and Sustainability (MARIS) at the University of Cape Town (UCT), in collaboration with the SAWS. The focus of this collaboration is to better understand sea ice lifecycle in the Southern Ocean. Hence, the proposed system aims to provide a low-cost, easy to deploy environmental data measurement system that can be expandable to operate in a network allowing for a single-system deployment

[6]For example: see Rabault et al. (2019) Github repository at https://github.com/jerabaul29/LoggerWavesInIce_InSituWithIridium.

strategy. In this thesis, the firmware design of a novel ice-tethered buoy for the Antarctic Marginal Ice Zone is presented. The goal is to develop a robust software system for a platform built using off-the-shelf components to monitor ice drift, atmospheric conditions and waves-in-ice measurements over a full seasonal cycle.

Figure 1.7: Novel ice drift, environmental monitoring and wave measurement autonomous platform: the Southern Hemisphere Antarctic Research Collaboration (SHARC) Buoy. Developed by the University of Cape Town. Photo by R. Verrinder.

1.2 Problem statement

This project aims to design a prototype system to monitor environmental conditions that lead to the formation of ice floes in the Marginal Ice Zone. The goal of the project is to increase in situ sensing in an affordable manner while allowing for easy access to the technology and data. Conclusion of this project will result in a fully automated system that can be deployed on an ice floe in various locations in the Marginal Ice Zone up to the packed ice boundary layer. Transfer of data from the system will occur using the available infrastructure in the region to reduce costs and make the system as non-invasive as possible. Furthermore, the resulting system will run off a portable power source with limited charging capability to survive for at least one month. By identifying and engaging with key stakeholders in the project, we aim to design a system using off-the-shelf components and synthesize components into a low-cost, high-performance solution with the final deliverable being a deployable system for the next South African Antarctic expeditions to the Marginal Ice Zone. Thereby creating the following project objectives:

1. Perform a literature review of the current state of remote sensing in the Southern Ocean, analysing the techniques and strategies implemented by each system.

2. Engage with key stakeholders to create a set of user requirements for the system, translate these requirements into system specifications, identifying critical subsystems and synthesising them into a high-level system.
3. Identify a suitable network for remote communication as well as the corresponding communication module.
4. Select suitable hardware components and develop a robust set of libraries and unit tests for each system.
5. Identify the energy requirements and select a suitable power source.
6. Identify a processor/set of processors that meet the requirements for the system and develop firmware in C using a Hardware Abstract Layer (HAL).
7. Connect the subsystems to a motherboard and place the system in an enclosure capable of protecting the system from the harsh climate.
8. Evaluate the platform against a serious of unit tests, robustness tests and hardware tests.
9. Deploy the system in the Marginal Ice Zone and monitor performance.

1.2.1 Project initiation

The project was initiated in 2018 with input from the following stakeholders.

Table 1.1: Legend showing the key stakeholders in the initiation of the project as discussed in the phases below. Legend includes name, reference number and department/institution.

Reference:	Name:	Institution	Department
1	Jarryd Son	University of Cape Town	Electrical Engineering
2	Nadir Vorajee	University of Cape Town	Electrical Engineering
3	Prof Amit Mishra	University of Cape Town	Electrical Engineering
4	A/Prof Marcello Vichi	University of Cape Town	Oceanography
5	A/Prof Sebastian Skatulla	University of Cape Town	Civil Engineering
6	Marc de Vos	South African Weather Service	N/A

Concept phase

The concept design was performed by Son (1) and Vorajee (2) under the supervision of Prof Mishra (3). The design was presented at the first meeting on the 11 September 2018 to the principle stakeholders A/Prof Vichi (4) and A/Prof Sebastian Skatulla (5). The proposed device was presented as an upgraded version of the Trident sensing buoy with expanded sensing capabilities. During the meeting, it was agreed to deploy and test the system during the Winter and Spring SCALE expeditions in 2019. The provisional dates for these cruises were: July 2019 and November 2019 respectively. A follow up meeting occurred on the 4th October 2018 where de Vos (6), (South African Weather Service

(SAWS)) expressed interest in the research and the development of the project. de Vos (6) provided additional context for the project and presented current work conducted by SAWS.

Procurement phase

A preliminary user requirement was conducted by Son and Vorajee (1, 2). From there, suitable components for each of the subsystems were selected with orders being placed on the 19th December 2018. This order included sensors, a Ublox GPS reciever, Zigbee short range communication modules, Rock7 Iridium satelite communication modules, STMicroelectronics STM32F1 microcontroller and inertial measurement units (IMUs).

Handover phase

The project was handed over to Jamie Jacobson under the supervision of Robyn Verrinder on the 8th February 2019, officially commencing the prototyping phase of the project.

1.2.2 Scope

This thesis focuses on the firmware design for the buoys. The outcome of this study will be a robust set of firmware and unit tests to validate the firmware against. The project timeline takes place from February 2019 to December 2020 with key deliverable dates being:

1. 18 June 2019 - SCALE Winter Cruise (Version 1.0 Complete)
2. 12 October 2019 - SCALE Spring Cruise (Version 1.0 Revisions)

As this thesis focuses on software development of the project, hardware design is not included in this study and future designs are discussed as recommendations. This includes the mechanical structure and the electronic modules. However, this study includes the selection of devices, which are evaluated against the technical specifications. Additionally, the hardware modules are described.

System testing is conducted on a subsystem software level and the full system. The testing procedures are described in Tables B.2 to B.10.

Large scale calibrations are not included in the project scope due to tight timeline constraints. Finally, the design, implementation and calibration of an IMU-based wave measurement algorithm are not explored in this project. The IMU however, will be validated and verified by sampling enough data to fit into a single Iridium transmission packet.

1.2.3 Limitations and constraints

The largest limitation to the project is time constraints. The project timeline coincides with the SCALE research cruise using the winter and spring expeditions for buoy deployment thereby limiting the time frame for development. Additionally, the firmware development is limited to the capabilities of the selected processor.

The firmware development is heavily constrained by the hardware selected for the platform. Peripheral drivers were written for modules that were agreed upon by the project members. Additionally, the IMU, processor, environmental sensor and satellite modem components were pre-selected in 2018. The firmware is thus constrained by design choices originally made in 2018 and early 2019 for the first version of the system. However, these designs were revised for subsequent versions of the buoy from September 2019. As a result of these constraints, the devices were designed without previous knowledge of the environment and with a limited number of sensors. Finally, the selected processor has a limited number of communication peripherals which influenced the types of sensors that were selected.

The communications network in Antarctica is severely limited and the most reliable form of remote communications is the Iridium satellite network. The amount of data that can be transmitted is limited in terms of bandwidth, data costs, packets structure and reliability of transmission. Testing for Antarctic conditions is restricted by available testing facilities, therefore, rigorous environmental tests may only be conducted during the expeditions.

The first prototype was deployed with a limited number of sensors due to development constraints. Mechanical failures resulted in the buoys ceasing operation within an hour of deployment during the 2019 SCALE Winter cruise. Further development occurred in 2020 to increase the sensing capability of the buoy. However due to the 2020 COVID-19 outbreak, all expeditions were cancelled for the year and therefore final system testing in the Antarctic MIZ was not possible. Attempts were made to deploy the devices on other expeditions from other countries. However, shipping delays were encountered preventing the device from reaching the expedition team on time. Currently, a prototype version has been sent onboard the SA Agulhas II to the SANAE IV base on the Antarctic continent where testing is expected to take place in late February 2021. This falls outside the time frame of this dissertation. Instead, the buoy will be tested on the home continent with low temperature tests being conducted in a commercial -20° C freezer. Currently, two buoys are on board the RV Polarstern and should be deployed in mid-March 2021 alongside with the Alfred Wegener Institute (AWI) buoys.

1.2.4 Assumptions

The following assumptions were made during the development of the firmware for the buoy. The device has sufficient power to access any of the sub modules if required. Devices that pass a connection test, are considered "online" and capable of producing reliable data. The processors are the ARM-based STMicroelectonics STM32L4 and STM32F4 microcontrollers and do not come preloaded with any real time/operating system. Development will take place using the Hardware Abstract Layer (HAL) driver files and all hardware that has been selected is rated for the environmental conditions described in Section 1.1. A system/subsystem is considered valid if it passes a suite of acceptance tests and verified if it meets the functional requirements. Devices that are not active need to be placed in power down mode. Finally, the system is considered complete if it can complete a single measurement cycle from power on without the assistance of any auxiliary equipment.

1.3 Plan of development

The plan of development describes how the project was conducted through the various stages. A literature review was conducted to analyse the current state of in situ monitoring technology in the region. Then, a problem statement was defined by engaging with project stake holders and developing a set of user requirements. The user requirements were used to formulate acceptance tests and technical specifications which were used to guide subsystem design and selection. Then, the firmware stage was initiated with the development of API libraries for each module of the device. These were then synthesised and sequenced into a software system defined by short periods of activity and long periods of inactivity. This was used to optimise the device for low power consumption. The system was tested by performing a power consumption test, which was used to evaluate the power characteristics. The device was set outside to run a full transmission cycle. Finally the results were analysed and used to validate the buoy as a viable tool for remote Antarctic monitoring.

1.4 Report structure

Table 1.2: Description of report structure including key phases of the project and significance

Chapter	Phase	Description
Chapter 2	Literature review	Description of the state of Antarctic climate modeling is discussed, including stochastic modeling processes and current sampling techniques using un-manned instrumentation. From this review, the key measurement objectives of each system are identified and an analysis of the state of the art will be used to identify the usefulness and areas where SHARC Buoy can provide a solution.
Chapter 3.1 to 3.3	System development	An analysis of project stakeholders is provided as well as an assessment of their needs. Then, a set of user requirements is developed and ranked in order of importance. The functional requirements selected will guide the device selection and, ultimately, be used to evaluate the performance of the final system. This lead to the identification of the critical subsystems shown in table 3.7 and a final system topology choice. A set of technical specifications were derived for subsystem hardware selection and a suite of acceptance tests were written to ensure the components conformed to the desired specifications.

Chapter 3.4 to 4.3	Platform overview	Description of the mechanical and electronic components that were selected for the device. The specifications of each component and price are given. The final system consists of a Ublox Neo-7M GPS, Rockblock 9603 Iridium modem, environmental sensor (BMP280), MPU6050 Inertial Measurement Unit and INA219 power monitor. Flash chips were selected as a permanent storage solution for data during phases of inactivity. The components were synthesised on a stack of three PCBs shown in Figure 4.5. A separate power module is shown in Figure 4.4. An overview on the assembly of the project is given to close the section.
Chapter 5	Software overview	A complete overview of the software design process is provided. The key features and focus of the software are outlined along with the firmware structure as shown in Figure 5.1. The project structure includes a breakdown of files, structure and driver files. The configuration of the processor for this application is shown as well as various peripherals and configurations used to set the device up for execution. Then a brief discussion about power mode and system selection ensued to provide clarity on the power-consumption optimisation process. Then a description of the firmware is given. A decision was made to implement a state machine. Here, a finite set of routines were defined and a description of the sequencing was given. Finally an over view of the flow of data from the device to the user was provided.
Chapter 6.1 to 6.2	Testing	In this section, the tests conducted on the platform and the system are given. These include subsystem acceptance test, full system tests, power tests and preliminary deployment test results from the 2019 SCALE winter expedition.
Chapter 6.3	Final evaluation	The results of subsystem acceptance tests are used to validate the system. The outcome of the project is compared to the functional requirements to determine the system's performance and verify that the project goals have been met.
Chapter 6.4	Discussion	This section provides a discussion of the results and key findings. The discussion focuses on the limitations of the power module and the outcome of the power test. Additionally, the performance of the device during the deployment test is discussed. An in-depth analysis of additional subsystem limitations is provided along with the performance of the firmware in spite of these limitations. The section concludes with a comparison of the buoy against other devices in the field.
Chapter 7	Conclusion	The outcome of the project is presented and a conclusion is made about the project outcomes, goals and whether the firmware was able to achieve them.
Chapter 8	Recommendations	Improvements and recommendations are provided for future work on the project. These include tests that could not be conducted, research and focus areas as well as hardware/ software improvements.

Chapter 2

Literature review

As highlighted in section 1.1, there is a great desire by research scientists for in situ instruments to provide observation data which fills spatial and temporal measurement gaps in Antarctic sea ice monitoring in the Southern Ocean as shown in Figure 2.1. This chapter investigates the current use of autonomous monitoring technology used by research scientists in this region focusing on progress made to improving in situ observations and highlighting areas for improvement.

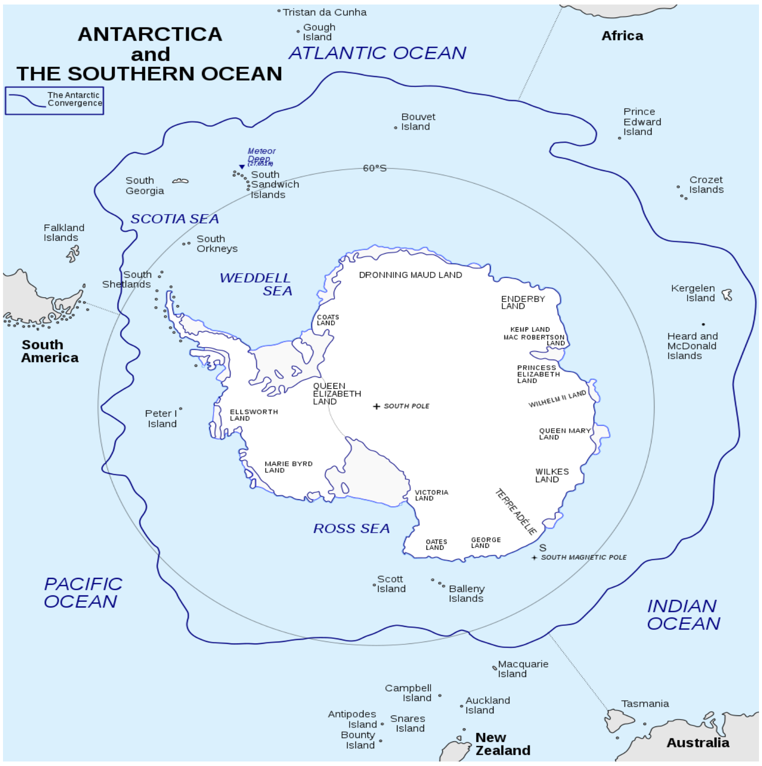

Figure 2.1: Map of the Southern Ocean surrounding the Antarctic continent. Image created by Hogweard (2015) and licensed by CC BY-SA 3.0.

In this review, a system-level analysis is provided where the objectives of each buoy are in the contexts of the requirements for new remote sensing technology as highlighted by Kennicutt et al. (2016). This includes an analysis on how these devices operated in remote conditions and the communication techniques employed in spite of a lack of infrastructure. The system-level analysis concludes with a discussion of the device measurement objectives, their performance in the Antarctic sea ice region and how this performance compares to their deployment in the Arctic region.

Next, a subsystem level analysis is given discussing how each device met their measurement objectives, what technology was used and how this technology works. Additionally, a comparison of different techniques for each subsystem is provided amongst devices with similar components and, where possible, a discussion of their accuracy is given. This section also highlights the critical measurement objectives of each device to understand which sub-modules are the most important for remote sensing. Finally, the processing architecture is discussed in the context of how it was implemented in the devices, what purpose it serves and how the data requirements for each device's sensors were met.

2.1 In situ climate sensing technologies

Autonomous instrumentation has seen increased use for in situ observations in the polar sea ice regions (Kennicutt et al., 2016). These devices have typically been developed by the commercial sector (Rabault et al., 2017) from companies such as Trident (Trident Sensors, 2021), MetOcean (Metocean, 2016), Seabird (Sea Bird Scientific, 2021) and Sea Technology Services (STS) (Sea Technology Services, 2021). Additionally, academic institutions have also developed in situ measurement devices such as the University of Washington's SWIFT buoy (Thomson, 2012) or University of Dartmouth's Seasonal Ice Mass Balance (SIMB) buoy (Polashenski et al., 2011). While these technologies have the benefit of reliability, they are often expensive (Rabault et al., 2017) and inflexible to the specific needs of polar scientists. Technology has reached a point where low-cost and open source alternatives are well documented and reliable enough to be integrated into customised solutions (Rabault et al., 2019).

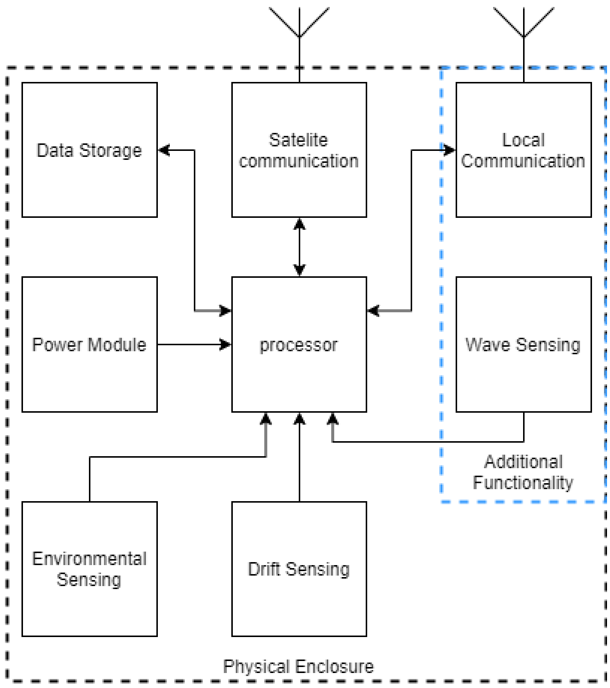

Figure 2.2: A block diagram of a typical device for in situ polar sea ice measurements. Each device contains modules for environmental sensing and drift sensing connected to a processor. This can be a microcontroller or microprocessor. Additionally, a data storage module (such as an SD card) is included to store data during the operation. Some devices include modules for local communication or wave sensing units. Finally, a remote communication module is included to transfer the data to a research centre or a user. The electronics are placed inside a physical enclosure for protection against the polar climate while a portable power module supplies the device during its operation.

In this section, a comparison of data collection devices used in the polar regions is presented as well as description of their design, operation and deployment. Where possible, certain specifications have been converted into standardised formats. To ensure a fair evaluation, data were collected from the latest technical publication of each platform, where possible. These publications may not contain all relevant data. In these cases, the data entries have been marked with a "Not reported" or "NR".

Eight platforms were selected for the comparison and are shown in Figure 2.3 with each device designed by a private company or an institution. The key collaborators as well as the name of the institution are provided in Table 2.1. Where a buoy name is not given, the device will be named after the key contributor to the project. These systems have been selected due to their prevalence in global polar/oceanographic science as well as notability in publications. Device performance is evaluated in the context of the requirements set out by Kennicutt et al. (2016) for an autonomous in situ measurement device shown in Section 1.1.

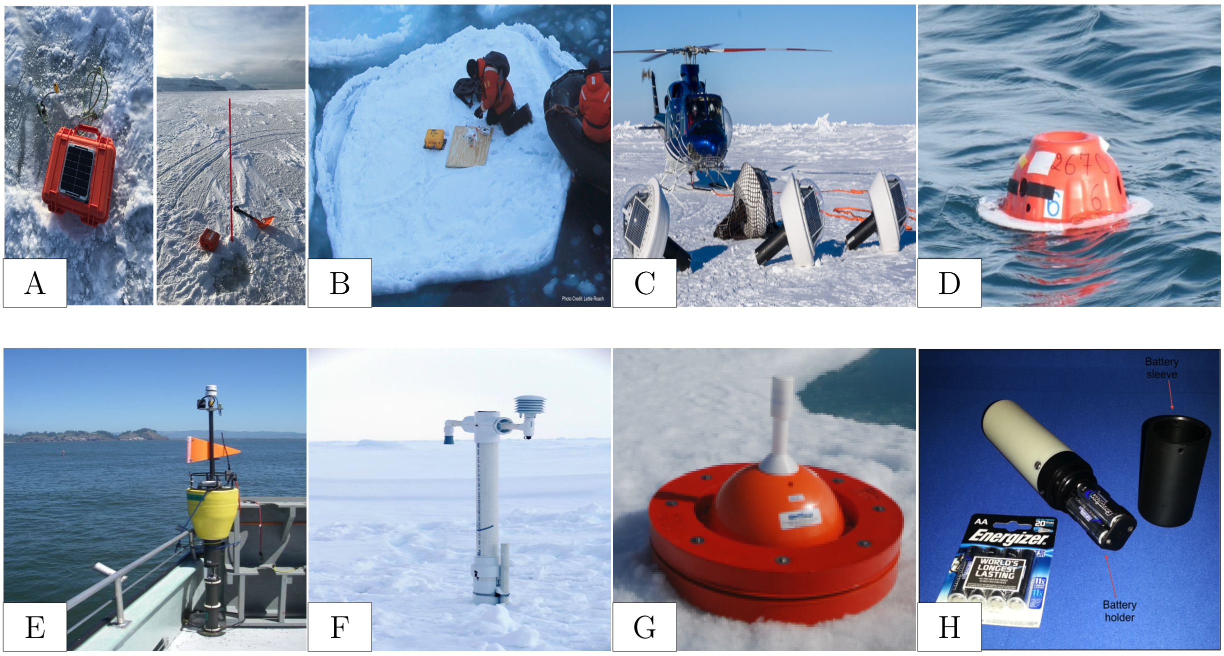

Figure 2.3: Devices used for the comparison of autonomous instruments deployed in the sea ice region. Each device has been selected for its notability in published work as well as prevalence in sea ice and wave interactions in the Marginal Ice Zones. These devices are: (A) Wave in Ice Buoy developed by Rabault et al. (2017), (B) Wave in Ice Observational System by Kohout et al. (2015), (C) Novel Wave Directional buoys by Doble et al. (2017), (D) Surface Kinematic buoy by Guimarães et al. (2018), (E) Surface Wave Instrument Float Tracking buoy by Thomson (2012), (F) Seasonal Ice Mass Balance buoy by Meng et al. (2014) and Polashenski et al. (2011), (G) Polar ISVP by MetOcean (Metocean, 2016), (H) Trident buoy by Trident (Trident Sensors, 2021).

A device that has sufficient autonomy and sustained capabilities will operate remotely with no human intervention. Therefore, the operating period of each device si compared. This is the period between deployment and final transmission where the buoy is active. Additionally, the techniques for remote communication for each buoy are examined in terms of data rates, coverage and transmission strategy to determine the techniques used to achieve remote communication effectively including a brief overview of available satellite networks. Then, to measure the sensing capabilities of each device, the measurement objectives are discussed as well as the hardware modules and software used to determine information. To compare the real time data collection, transfer and analysis, the device's processing strategy and storage strategies are considered. Data transfer techniques are analysed with the remote communication section. Finally, device performance in the polar regions is evaluated through the success of each deployment, device deployment time, data integrity is compared as well as devices that failed and the causes of those failures.

Table 2.1: Devices used for the comparison including the device name, lead developer and the institution. These consist of both commercial and institutional devices for in situ sea ice and wave measurements.

Device Name	Developed By	Institution
Waves in Ice Buoy (WIIB)	Jean Rabault	University of Oslo, Norway (Rabault et al., 2019)
Waves in Ice Observational System (WIIOS)	Alison Kohout	National Institute of Water and Atmospheric Research (Kohout et al., 2015), New Zealand
Novel Directional Wave Buoys (NDWB)	Martin J. Doble	Polar Scientific (Ltd.), United Kingdom (Doble et al., 2017)
Surface Kinematic Buoy (SKIB)	Pedro Veras Guimarães	Université de Bretagne Occidentale, France (Guimarães et al., 2018)
Surface Wave Instrument Float with Tracking (SWIFT) Buoy	Jim Thompson	University of Washington Applied Physics Laboratory, United States of America (Thomson, 2012)
Seasonal Ice Mass Balance Buoy (SIMB)	Donald K. Perovich	Dartmouth College (Planck et al., 2019)
Polar ISVP	MetOcean	MetOcean
Trident Buoy	Trident Sensor	Trident Sensor

2.2 System level overview

2.2.1 Remote communication

On the Antarctic continent, remote communication is critical for ongoing scientific activities allowing for data to be transmitted from instruments to research stations and camps (Lee et al., 2016). These activities are further supported by high speed, high bandwidth communication networks such as fibre links (Jabbar, 2001). However, these networks have been implemented on a small scale to support permanent field camps (Lee et al., 2016) on the continent. Lee et al. (2016) show that communication from polar stations and field sensors to the rest of the world occurs using satellite constellation networks. These constellations are classified as geostationary earth orbit (GEO)(Jabbar, 2001) such as Inmarsat (Inmarsat, 2021) and Intelsat (Intelsat, 2021) or low earth orbit (LEO) such as ORBCOMM (ORBCOMM, 2021), Iridium (Iridium, 2021), Globalstar (Globalstar, 2021). GEO satellites consist of 2 to 8 satellites orbiting the equator (Jabbar, 2001). As a result, the network coverage is strong for mid-latitudes and weak for low latitudes. However, these satellites cover large areas providing longer connectivity (of up to 6.5 hours) (Lee et al., 2016). LEO satellites cover less surface area and have a smaller connectivity window (10 to 30 minutes). However, these constellations consist of more satellites. Additionally, the Iridium satellite network is the only LEO network thats reach covers the polar region (Jabbar, 2001) and allows for longer network connectivity. The constellation consists of 66 satellites (Lee et al., 2016) and is well optimised for marine applications making it suitable for Southern Ocean sea ice activities. Iridium is a satellite network with global coverage and a variety of modems for various IoT uses. The company offers four main data services. Each service places constraints on the data transmission rates, bandwidth and modem selection. Each modem runs a data service that dictates the transmission rates, bandwidth and protocols. Table D.1 shows the available network services. Furthermore, a full description of these modems is shown in Table 2.2.

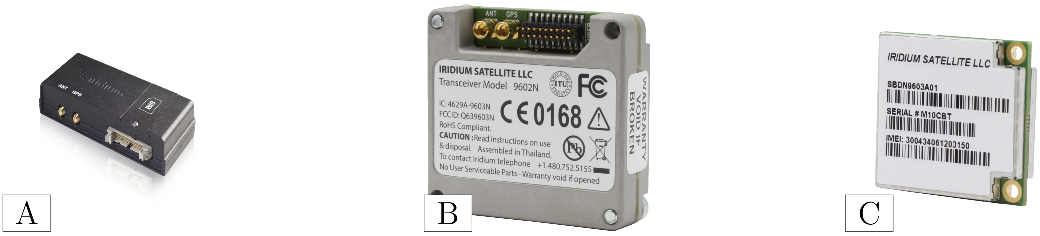

Figure 2.4: Examples of popular Iridium modems selected for remote communications. (A) The 9522B modem (image source: (Iridium Satellite Communications, 2020)), (B) the 9602 modem (image source: (Iridium Satellite Communications, 2020)) and (C) the 9603 modem (image source: (Iridium Satellite Communications, 2019))

Table D.2 shows the satellite network used by each device. All devices use the Iridium satellite constellation as the primary remote communication method. Other short range wireless systems such as Zigbee (Guimarães et al., 2018) are alluded to, however these systems are only used when the device is close by. Notably, The SIMB buoy details consideration for remote communication using the ARGOS satellite network however, the unreliability of the network resulted in irregular timestamped data (Planck et al., 2019). The network service, modem and transmission strategy of each device is shown in Table D.2.

Table 2.2: The following Iridium modems are compared in their key specifications. Devices in the table were suitable for IoT applications based on prevalence in literature and recommendations from the manufacturer. Key parameters include weight, power consumption and transmission latency. Information is taken from (Iridium Satellite Communications, 2020) with prices as of February 2021[1].

Device Name:	**9602**	**9603**	**9522B**[2]	**9523**	**Edge**
Weight [g]	30	11.4	420	32	330
Input Voltage [VDC]	5	5	4 to 32	3.2 to 6	9 to 32
Idle Current [mA]	35	34	250	70	300
Transmit Current [mA]	140	145	2500	500	300
Recieve Current [mA]	40	39	2.5×10^3	110	300
Packet Latency [s]	20	20	N/A	45	20
Price	R2,526[3]	2,526[4]	R23,317[5]	R13,123[6]	R5,638[7]

Unanimously, all devices use the Iridium satellite network for remote communication with the Iridium 9602/3 Short Burst Data (SBD) modem being used the most. This choice is justified for its small form factor, low power and easy interfacing as shown in Table 2.2. However, it suffers greatly from limited bandwidth having a maximum transmission size of 340 bytes. Systems that use these modems for transmission of wave data rely on complex data processing algorithms and therefore do not transmit the raw time series. The only notable exception to this is the wave buoy developed by Doble et al. (2017), which continuously transmitted data from an attitude and heading reference system (AHRS) as well as IMU time series data once every minute. For this purpose, they used the 9522B modem which allowed for continuous transmission using the router-based unrestricted digital internetworking connectivity solutions (RUDICS) data service. This modem, along with the SBD modem used for the SWIFT Buoy also has a much larger SBD data buffer (1.92 KB) However this device draws the most current during idle, transmit and receive states. Additionally this modem is expensive costing R23,317 compared to the 9523 (R13,123) and the 9602/3 (R2,526).

[1]GBP 1 = ZAR 20.41; USD 1 = ZAR 15.1
[2]source: https://www.rock7.com/shop-product-detail?productId=49
[3]source: https://www.rock7.com/shop-product-detail?productId=50
[4]source: https://satellitephonestore.com/catalog/sale/details/iridium-9522b-transceiver-496
[5]source: https://www.africasatellite.com/Iridium-9523-Core-Module-p/iridium-9523-core-module.htm
[6]source: https://www.rock7.com/shop-product-detail?productId=56

2.2.2 Power supply

A robust power supply is critical to support the functionality of a remotely deployed device. A successful power supply can extend the deployment range, duration, processing capabilities and functionality of sensors (Kennicutt et al., 2016). Device operation in the Southern Ocean MIZ presents a challenge where the constant freezing/refreezing of the ocean surface layer prevents long-term infrastructure from being implemented. Hence, a remote device for sea ice monitoring requires a portable power source. Figure 2.5 shows a diagram of a typical power module for a remote sensing device.

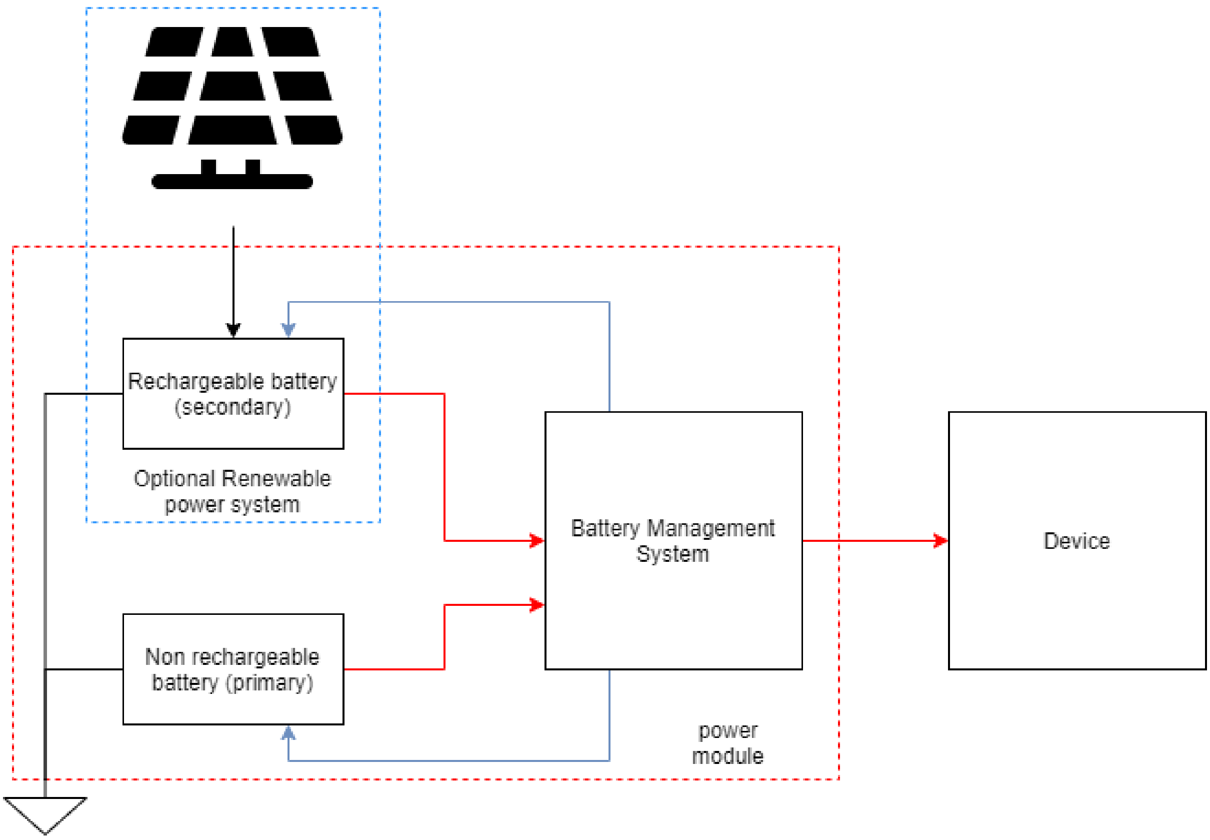

Figure 2.5: A block diagram of a typical power module for a remote sensing device based off the information from (Doble et al., 2017; Rabault et al., 2019; Vidal et al., 2019). Batteries are used as a primary source of energy which is connected to a battery management system to control and regulate the power supply to the device. Optionally, solar panels are implemented with a rechargeable battery as a secondary power supply. Shown in the figure: flow of power (red), control lines (blue) and ground (black).

Batteries such as lithium-ion are commonly used as sources of power for in situ devices in low temperatures. Batteries typically fall into one of two categories:

1. Primary: Cells that cannot be recharged once they are depleted. These batteries have a high energy density and can store charge for long periods(Besenhard, 2008).
2. Secondary: Cells that can be recharged. These cells are more cost effective with longer usage cycles (Besenhard, 2008).

Lithium-ion and alkaline batteries are examples of primary cells that have commonly been used as they provide a cost effective solution due to their high energy density and long-term consistent life cycles (Al-Zareer et al., 2018). Secondary cells such as lead-acid, nickel-metal hydride and lithium polymer are commonly used coupled with a secondary charging circuit such as a solar panel (Manimekalai et al., 2013) to provide a more constant source of power. While batteries are cost effective solutions, the climate of the Southern Ocean can affect the battery performance. Freezing air temperatures can reduce the capacity of a standard lithium cell by up to 50% for temperatures below -10° C (Doble et al., 2017; Zhang et al., 2003). Additionally, frozen batteries or ice formation on batteries can stop them from working (Doble et al., 2017; Manimekalai et al., 2013). A solution to compensate for this reduction in capacity is to use rechargeable batteries coupled with a renewable power sources such as solar (Doble et al., 2017; Rabault et al., 2019), wind and geothermal energy (Manimekalai et al., 2013). Solar photovotaic (PV) cells are the fastest growing renewable energy source with the highest energy density (Jordehi, 2016). PVs have numerous advantages such as low maintenance and operational costs, wide temperature operations and long life-cycles (Jordehi, 2016) which makes them ideal for long term operation in remote environments. However, the power output of PV cells are significantly affected by weather conditions (Sharma et al., 2015). Therefore, areas with poor sunlight coverage will not benefit from solar panels. Therefore this energy source is not suitable for winter Antarctic expeditions due to the lack of sunlight (Lever et al., 2006). Additionally, power generation from solar panels is inconsistent and requires an additional storage bank capable of frequent charging and discharging. Wind energy can provide a viable alternative to solar energy. Vichi et al. (2019) show that the Southern Ocean hosts strong, consistent winds. However, the design and implementations have not been discussed in any of the literature. Therefore this options is provided as an area for future research. Finally, a critical component of the power system is a battery management system. This allows the power supply to operate under safe conditions while meeting performance requirements (Vidal et al., 2019). This module includes power monitoring, power control and energy cycle optimisation. Table 2.3 below shows the power sources used by each device and the strategy used to manage it.

Table 2.3: A comparison of power supply strategies of the different devices showing the the power source, topology of the power supply module as well as the voltage supplied at the output of the module. Information that was unavailable at the time of research has been labeled as "Not Reported"

Device Name	Primary power source	Secondary power source	Battery management system	Output regulation strategy	Output voltage [V]
WIIB	Lithium Iron Phosphate ($LiFePO_4$) battery	None	ATMEL ATMega328P for Power control	Boost converter	5
WIIOS	Alkaline battery	None	Integrated into firmware	8-cell series configuration, no regulator	12
NDWB	Alkaline battery	Solar panel and lead-acid battery	Not Reported	Not Reported	12
SKIB	Lithium thionyl chloride ($LiSOCl_2$) battery	None	Not Reported	Not Reported	3.6
SWIFT	Alkaline or lithium battery	None	Not Reported	Not Reported	14
SIMB	Alkaline battery	None	Not Reported	Texas Instruments LMZ12003 Step down converter (5 V, 3.3 V) Microchip MIC29201-12W Low dropout regulator (12 V)	3.3 5 12
Polar ISVP	$LiSOCl_2$ battery	None	Not Reported	Not Reported	12
Trident	Lithium cell battery	None	integrated into firmware	Low dropout regulator	5

Table 2.3 shows the power supply strategies of each device. All systems use primary batteries as a source of power with the most common choice being alkaline or lithium-based batteries. However, Doble et al. (2017) are the only exception where a secondary power source was added consisting of a solar panel and lead-acid batteries. As a consequence of the added power system the NDWB had an increased weight which affected its portability and ease of handling. This is discussed further in Sub-section 2.2.4. Furthermore, systems deployed in the Arctic Marginal Ice Zone have been designed with a recharging system such as a solar panel in the case of WII Buoy and NDWB. However, most long-range deployment buoys have opted for non-rechargeable systems composed of lithium thionyl chloride ($LISOCL_2$) or alkaline batteries. In the case of the high-power buoys (SIMB, WIIOS, NDWB, Polar ISVP) an array of 3.3 V to 3.7 V cells are connected to provide a nominal voltage in series with a regulator to provide a stable output. The strategy for each system is to pack as many batteries in as possible to satisfy the long-term energy requirements (Doble et al., 2017; Rabault et al., 2019). Finally, few devices have reported their battery management strategies. Rabault et al. (2019) used an ATMEL ATMega328P microcontroller as a power controller for their device which monitored the status of the battery. Trident Sensors (2021) and Kohout et al. (2015) however integrated power control into their main firmware allowing for them to control and monitor their power source off a single processor.

2.2.3 Polar performance

This section outlines the deployment of the systems in the Arctic/Antarctic marginal ice zones and compares the survivability and performance of each system. The focus of this section is be predominantly on devices deployed in the marginal ice zone. Table 2.4 shows the significant deployment locations in the Arctic and Antarctic sea ice zones as well as the deployment objectives of each device.

Table 2.4: Comparison between the functionality and purpose of the buoy showing the critical measurements as well as the significant deployment locations either in the polar ice zones or in a location critical to the validation of the device.

Device name	Deployment objectives	Antarctic deployment locations	Arctic deployment locations
WIIB	Wave energy attenuation Significant wave height Data quality	Ross Sea landfast ice (Rabault et al., 2020)	Templefjord (Svalbard) landfast ice (Rabault et al., 2019) Northeast Barents Sea (Rabault et al., 2019)
WIIOS	Ice drift Waves in ice Ambient temperature Atmospheric pressure	Ross Sea Marginal Ice Zone (Kohout et al., 2020) Ross Sea packed ice zone (Kohout et al., 2015) Weddel Sea Marginal Ice Zone (Alberello et al., 2020; Vichi et al., 2019)	Not Reported
NDWB	Ice drift Wave induced breaking Ambient temperature Atmospheric pressure	Not reported	Beaufort Sea (Doble et al., 2017)
SKIB	Ice drift Surface waves	Not reported	North Atlantic Ocean (France) (Guimarães et al., 2018)
SWIFT	Ocean surface Ocean waves Turbulence profiles Ocean current profiles Conductivity Wind speed and direction	Ross Sea (Ackley et al., 2020) Weddel Sea (De Santi et al., 2018)	Chukchi Sea (Hošeková et al., 2020) Beaufort Sea (Lund et al., 2018)
SIMB	Surface and bottom ice position Snow depth Ambient temperature Atmospheric Pressure Vertical ice temperature profile GPS location	Weddel Sea (Hoppmann et al., 2015)	Beaufort Sea Marginal Ice Zone (Planck et al., 2019)
Polar ISVP	Sea ice drift Ambient temperature Atmospheric pressure	Weddel Sea Marginal Ice Zone (Grosfeld et al., 2016; Haas & Nicolaus, 2016)	Western Arctic Ocean (Lei et al., 2020)
Trident	Sea ice drift Ambient temperature Battery voltage	Weddel Sea (Alberello et al., 2019; Vichi et al., 2019)	Not Reported

Kohout et al. (2015) deployed five Wave in Ice Observational Systems (WIIOS) in the East Antarctic Marginal Ice Zone during the Sea Ice Physics and Ecosystem Experiment

(SIPEX) mission[1] with the goal of capturing wave in ice events with measurement goals shown in Table 2.4. Three devices were deployed from helicopters on ice floes while two devices were deployed from the ships crane. Kohout et al. (2015) note that deployment via crane was successful in spite of 7 m swell and 25 ms^{-1} winds. The device was fitted inside a Pelican box with a sealed membrane surrounded by a tyre for protection and flotation in case of melting (Kohout et al., 2015). Consequently, this places the buoy directly on the surface of the floe rendering it susceptible to snow build up and flooding as mentioned in the previous sections. After deployment, the crew received 600 samples of data over 39 days in total. However, the first device failed 20 hours after deployment coinciding with the first large wave event captured the buoys (Kohout et al., 2015). The second large wave event resulted in the failure of two more systems just 9 days after deployment (Kohout et al., 2015). The fourth buoy lasted for 17.5 days. The final buoy survived the longest at 39 days. As a result only one device lasted for the expected time with the majority of data captured during calm events.

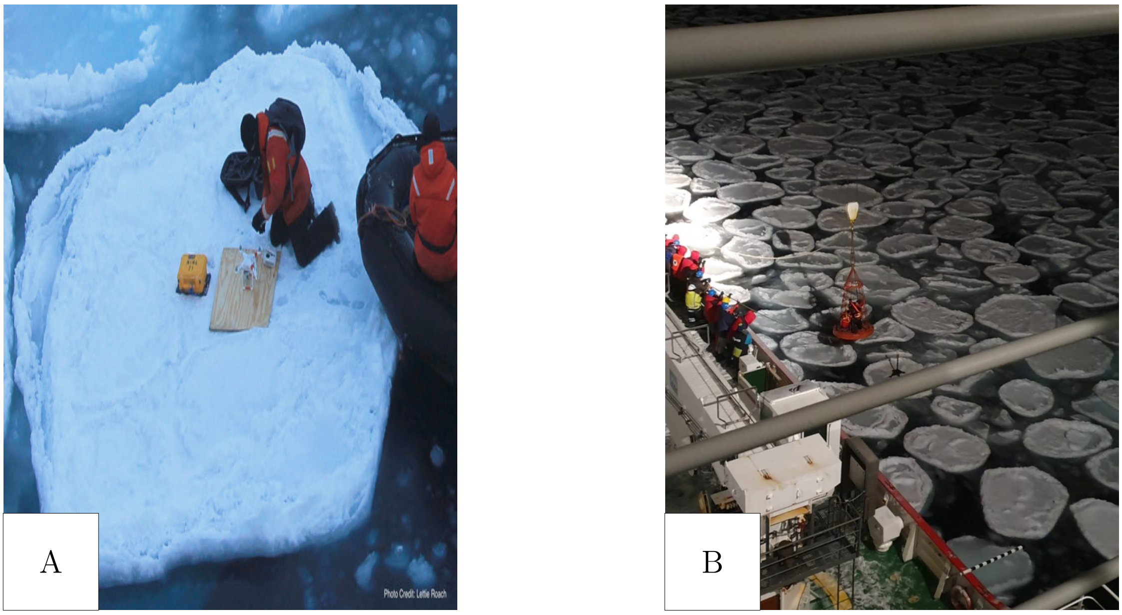

Figure 2.6: Examples of different deployment protocols for ice tethered devices.(A) In regions of consildated ice in favourable conditions, manned crews will step foot on the ice to deploy the device (image source: (Kohout et al., 2020)).(B) In unfavourable conditions, devices may deployed from a basket attached to a crane or a manned crew will lower the buoy onto a suitable ice floe from the safety of the basket (image source: N. Taylor).

Two additional WIIOS buoys were deployed by NYU Abu Dhabi (Alberello et al., 2019; Vichi et al., 2019) during the winter of 2017[2]. Here, the buoys lasted for periods similar to the devices from previous deployment. The first system survived for 8 days while the second system survived for 3 weeks in spite of measures taken to place the device in power saving mode (Alberello et al., 2019; Vichi et al., 2019). This was achieved by lowering the sample period from one sample every 15 minutes to one sample every 2 hours. Consequently, the lower temporal resolution resulted in a significantly reduced accuracy

[1]First deployment occured September 2012 (Kohout et al., 2015)
[2]First deployment occured in July 2017 (Alberello et al., 2019; Vichi et al., 2019)

of the ice deformation calculations (Alberello et al., 2019; Vichi et al., 2019). However, despite this low resolution, by operating at a temporal scale of 3 hours or less (Alberello et al., 2019; Vichi et al., 2019), one can effectively and accurately capture ice drift speed as well as the oscillations surrounding the movement. Additionally, Alberello et al. (2020) and Vichi et al. (2019) discuss the deployment of two Wave in Ice Observation Systems similar to the ones by (Kohout et al., 2015). Two devices were deployed on two separate ice floes 3 m in diameter and 100 km the ice edge (Alberello et al., 2020; Vichi et al., 2019). One system survived for 8 days and 18 hours while sampling every 15 minutes before transmission ended (Alberello et al., 2020; Vichi et al., 2019). The second buoy, however, survived for 6 days sampling every 15 minutes until it switched to power saving mode surviving for a total time frame of 3 weeks. Alberello et al. (2019) and Vichi et al. (2019) deployed a second pair of WIIOS buoys. However, the first buoy stopped responding after three days while the second buoy survived for 16 days (Vichi et al., 2019). While the buoys' survival is largely attributed to power optimisation, the lifespan could be influenced by the selection of the ice floe. Ice floe size and proximity to the ice edge affect the exposure of the floe to open-ocean processes and storms (Vichi et al., 2019). This could result in failure due to ice mechanics which is discussed in Section 2.2.3.

Rabault et al. (2019) deployed the Waves In Ice Buoy (WIIB) WIIB on landfast ice in the Ross Sea (Rabault et al., 2020) to test the device's performance in the Southern Ocean. In a similar fashion to the WIIOS buoy, the device was placed in a Pelican case and attached to a flotation device. However, expected survival time for this device was significantly lower compared to the WIIOS devices: a maximum of 8 days (Rabault et al., 2019) of continuous operation. The buoys by Kohout et al. (2015) were designed to be expendable whereas the buoys by Rabault et al. (2019) were designed to be retrievable. Additionally, the WIIB devices were deployed in the summer[3]. Two devices were deployed in close proximity to each other. However an ice break event resulted in the separation of the devices. The devices survived for 2.5 weeks (Rabault et al., 2019) which Rabault et al. (2019) attribute the failure to the devices having been crushed by ice and wave activity. Despite this, the devices were able to record significant wave events and maintain a fully charged battery throughout the deployment which Rabault et al. (2019) attributes to the solar panel.

Doble et al. (2017) alluded to a series of environmental considerations when designing the NDWB systems. One such consideration is the frosting over/rimming of the device due to freezing ocean spray. Additionally long periods of heavy cloud cover and no sunlight can affect the performance of the solar powered battery systems (Doble et al., 2017; Lever et al., 2006). Since the buoys were deployed by a manned crew, the design also had to account for ease of handling by the crew and not be too heavy (Doble et al., 2017). The mechanical enclosure consisted of a float and a keel with the electronics contained above the surface in a dome. Twenty buoys were deployed in the Arctic Marginal Ice Zone with each device anchored by drilling a hole in the ice and placing the keel inside. Nineteen buoys survived the deployment with one system failing to boot. The buoys survived for extremely long periods with twelve systems surviving for 200 days off a single alkaline battery pack (Doble et al., 2017). A significantly longer period than both the WIIOS and WIIB systems. Seven systems ran for 70 days on alkaline batteries before switching

[3]First deployment date: December 2019 (Rabault et al., 2019)

over to the solar powered lead-acid batteries. During this period, devices transmitted continuously over the Iridium network and were able to interpolate sea ice phases (see Section 1.1) from the tilt of the buoy (Doble et al., 2017). However, unlike the design phase for the NDWB was unconstrained by costs unlike the design phases of devices by Kohout et al. (2015), Planck et al. (2019), and Rabault et al. (2019).

Reasons for failure

Eventually, the systems by Doble et al. (2017) lost transmission 300 days after their deployment. This can be attributed to the depletion of the alkaline battery packs. The solar powered lead acid battery voltage eventually dropped below the alkaline battery voltage due to the lack of consistent solar coverage (Doble et al., 2017). Additionally, sub zero temperatures have a tendency to reduce battery capacities by up to 50% (Doble et al., 2017). However, Doble et al. (2017) found this estimate to be over conservative. Systems by Kohout et al. (2015) and Doble et al. (2017) encountered similar failures with devices eventually depleting the on-board batteries. Additionally, Vichi et al. (2019) and Alberello et al. (2019) attributed failure of the first WIIOS system to the battery being depleted.

Additional sources of failure experienced by Doble et al. (2017) include ice convergence. The systems were subject to ice-mechanics and as a result, ended up crushed by the floes due to rafting or buried under ice Doble et al. (2017). These failures were identified when more than one system suddenly went offline. Devices also experienced freeze-over or were buried under snow which resulted in the devices going offline for temporary periods (Doble et al., 2017). Additional evidence of rafting and ridging was captured by webcams on the buoy shortly before transmission ended (Doble et al., 2017). Buoys that survived the spring melt refroze during the gradual refreezing of the ice. During the second cycle, none of the buoys rebooted when the ice melted in the spring (Doble et al., 2017). Finally, the buoys developed by Kohout et al. (2015) and Rabault et al. (2017) sit in close proximity to the ice floes. As discussed previously, during the winter cycles, snow accumulates on the surface that can reach up to 1 m in height. This snow formation can result in flooding where the floe becomes submerged. Prolonged burying under snow may have resulted in the device freezing over thereby losing contact while prolonged contact with the seawater may have resulted in the buoys failing on several occasions ((Alberello et al., 2020; Kohout et al., 2015; Rabault et al., 2019; Vichi et al., 2019))

Figure 2.7: During the 2019 SCALE winter expedition, a SWIFT device was retrieved early due to lost communication with the host. This failure was attributed to a build up of ice along the rim from ocean spray. Photo taken by author.

Finally, Vichi et al. (2019) discuss the findings surrounding the failure of the first WIIOS system. Vichi et al. (2019) observed a major cyclonic event. The cyclone formed on 2 July 2017 and achieved lysis on 5 July 2017 which coincided with the buoy deployment. Following the event, four more cyclonic events were recorded with three explosive cyclones (Vichi et al., 2019) characterising a change of pressure over 24 hours. During this time, Vichi et al. (2019) observed winds speeds of up to 33 ms^{-1} while noting that the air temperatures had increased to values "close to melting" (Vichi et al., 2019). Additional observations found an increase in significant wave height in the activity. These conditions indicate deformation (Vichi et al., 2019) which may have subjected the buoys to forces experienced by (Doble et al., 2017) during their Arctic deployment which were verified against the temperature and pressure readings of the second WIIOS during the cyclonic event. The buoys were deployed close to the ice edge exposed to greater open ocean processes and cyclonic activities than other semi-consolidated and consolidated regions (Vichi et al., 2019). As a result, air advection, storms and large wave movement delay the consolidation of sea ice considerably (Vichi et al., 2019). Hence, the ice floes were more likely to experience rafting, ridging (Carsey, 1992), extended flooding, and freezing over which may have caused the failures of the WIIOS buoys.

2.2.4 Overall cost

A key factor of buoy development is the cost and weight of the overall device. Since these devices are still deployed manually, such deployment techniques involve the use of on-ship cranes (Alberello et al., 2019; Kohout et al., 2015), or by setting foot on the deployment site (Planck et al., 2019; Rabault et al., 2019). Additionally, Doble et al. (2017) deployed buoys by transporting them on a twin Otter aircraft and installing them on arrival. This shows that the weight and form factor of the device can impact the ease of deployment as well as where the device can be deployed. Table 2.5 provides insight into the quoted price[1] and development cost of each device to understand how expensive the current state of the art is.

Table 2.5: Comparison of price and weight of each device according to the published literature or commercial listing. Weight provides an indicator of the ease of handling whereas price provides an indicator of affordability. Prices have been converted to South African Rand (R) online (Oanda Corporation, 2021)where applicable while weight has been converted to Kg. "Not Reported" or "N/R" is given where a value could not be obtained.

Device Name	**Weight [Kg]**	**Price**
WIIB	4.5	R30,200[2]
WIIOS	N/R	N/R
NDWB	150	N/R
SKIB	N/R	R39,784
SWIFT	30	N/R
SIMB	34	R58,909
Polar ISVP	11.34	R52,119
UptempO	105	R863,686
Trident	0.42	R30,525[3]

Table 2.5 shows the current cost of in situ sensing devices. The cheapest wave sensing device is the WIIB at R30,200 showing that Rabault et al. (2019) succeeded in developing a feature-rich device for a relatively lower cost than the current state. Also included in the price comparison is a version of the Polar ISVP for deployment on ice floes called the UpTempo. This device is the lowest cost efficient device at R875,800 with only a GPS, pressure sensor and temperature sensor. This shows that to provide a cost effective solution, a new device will have to cost less than R30,200. However, this can be possible through the use of open-source and off-the-shelf solutions (Bonvoisin et al., 2017). As discussed in Section 1.1 the goal of remote sensing technology is to increase sensing in the region. To achieve this, more devices spread over a larger region are required. Finally, the cost efficiency of stand alone devices impacts the temporal and spatial scalability that can be achieved as it may not be possible to afford the required number and type of device to deploy during an expedition. This results in insufficient data to cover the Antarctic marginal ice zone over a seasonal period.

[1] Price as of February 2021.

[2] USD 1 = ZAR 15.1

[3] GBP 1 = ZAR 20.41

2.3 Subsystem overview

This section focuses on the subsystem analysis and component selection for each system. As stated previously, each buoy was created with a unique objective shown in Table 2.4. These objectives have been influencing the sensor selection, topology and layout of the overall subsystems. In addition, the device designs choices have influenced objectives for developing new in situ technologies by Kennicutt et al. (2016) as the device developers have factored in power consumption (Kohout et al., 2015), ease of use and deployment (Rabault et al., 2019), long-term operation (Doble et al., 2017), cost (Planck et al., 2019; Rabault et al., 2019) and availability of infrastructure (Doble et al., 2017) over and above functionality. For example WIIB was developed using open-source hardware (Rabault et al., 2019) to increase access to readily available technology while WIIOS was developed using off-the-shelf components (Kohout et al., 2015) to create a cost effective device. From Table 2.4 we saw that the principle measurements of each device share the following measurement objectives:

1. Ice drift
2. Wave data/Wave in Ice data
3. Ambient temperature
4. Atmospheric pressure

The following sections discuss how these objectives have influenced sensor selection for each of these measurements as well as the hardware, and software strategies implemented to achieve these objectives.

2.3.1 Processing capabilities

The processing capabilities of each device facilitate the functionality of each buoy. A processor allows for the implementation of in situ data processing and wave analysis algorithms (Kohout et al., 2015; Rabault et al., 2019). Additionally, due to the bandwidth constraints mentioned in Section 2.2.1, some devices require data compression algorithms to allow the data to fit in the transmission buffers. The functionality of these devices has been made possible through the use of microprocessors.

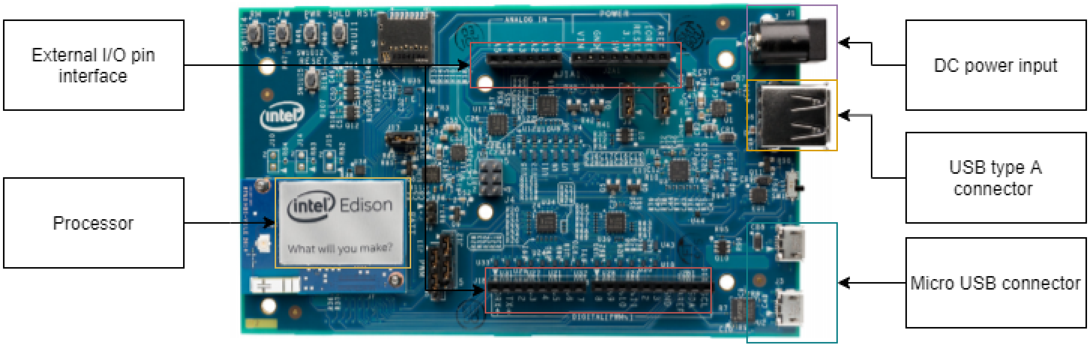

Figure 2.8: Diagram of a typical microprocessor (yellow) on a development board. This device is an Intel Edison which was used as the main processor by Kohout et al. (2015) for the WIIOS. The development board allows for fast prototyping and integration into projects. The processor interfaces with external peripherals through physical input/output pins (red) and contains standard serial communication ports such as USB (orange), micro USB (teal) and a connector for external voltage (purple). Image source: (Intel, 2015)

These are programmable integrated circuits that contain processing elements (Sarkar, 2018) and form the basis of microcontrollers and microcomputers (Crisp, 2003). These components are small and are increasingly becoming integrated into affordable, widely available components such as Raspberry Pis and Arduinos (Rabault et al., 2019). Table 2.6 shows a comparison of processors and topologies implemented in each design.

Table 2.6: Comparison of the processing strategy implemented by each device. Multiple processors have been used in a selection of devices, hence included in the comparison is the number of processors used, the type of processor and the function of each processor.

Device name	Number of processors	Processor name	Function
WIIB	3	ATMEL ATMega 328P	Low power unit
		Arduino Mega 2560	Data logger
		Raspberry Pi Zero	Wave processing
WIIOS	2	Intel Edison dual core	Wave processing
		ATMEL ATMega 328P	Low power unit
NDWB	1	ACME Systems Fox G20	Power control
SKIB	2	Silicon Labs EFM32-M3	Wave spectral processing
		Unspecified processor	Power control
SWIFT	1	Sutron Xpert	Data processing
SIMB	1	ATMEL ATSAMD21G18	Data processing control
Polar ISVP	1	Global Platform Transceiver Controller (GPTII)[1]	Data processing and control
Trident	2	Unnamed microprocessor	Data processing
		Unnamed low power unit	power control

From Table 2.6, we can see that each device has been developed either with a single, powerful processor or with multiple, low powered processors. NDWB for instance builds its system around the dominant sensor i.e. the AHRS IMU with a single processor controlling all the peripherals as well as allowing for data processing. Drift loggers such as Trident, and Polar ISVP feature sparser sets of electronics with smaller, lower-powered processors for power control and peripheral control, In contrast, WIIOS and WIIB compartmentalise subsystems with a cluster of processors handling different aspects from the buoy. This shows a focus on computation rather than sensing as multiple controllers are used to free the main processor for implementing advanced digital signal processing. SWIFT buoy appears as the outlier as the system is built around a dedicated data logger i.e. the Sutron Xpert with an integrated processor and satellite communication link abstracting data processing strategies on the buoy side. The SIMB buoy has the most advanced and largest number of sensors of all the buoys. A commonality among the buoys is the use of off-the-shelf components and processors. Another predominant feature, the GPS is an Adafruit MTK339 as well as ATMEL SAMD Chips, Raspberry Pis and Arduino boards whereas, for Trident and MetOcean, more expensive solutions are used. This shows that developers have opted for ready-made that components that are auxiliary to the main measurements. This should explain why some components on a system are more advanced than others. Finally, Trident and MetOcean are commercial systems and have therefore developed their own integrated solutions for sensors, processors and circuitry

[1]Developed by Metocean (2016)™

while researchers have opted for off-the-shelf components and development boards.

2.3.2 Measurement of wave data using inertial measurement systems

Typical wave state estimation is derived from calculating wave parameters such as significant wave height and dominant wave frequency (Williams et al., 2013). Additionally, wave data can be analysed in terms of its power spectral density. The two main methods for wave data analysis presented in this section are the Kuik Method and the Welch-Earle Method. Further explanations can be found in Appendix A.3.1. Both approaches rely on a discrete time series of inertial data from a device with 3 axes of acceleration of 3 axes of rotation (Earle, 1996; Kuik et al., 1988).

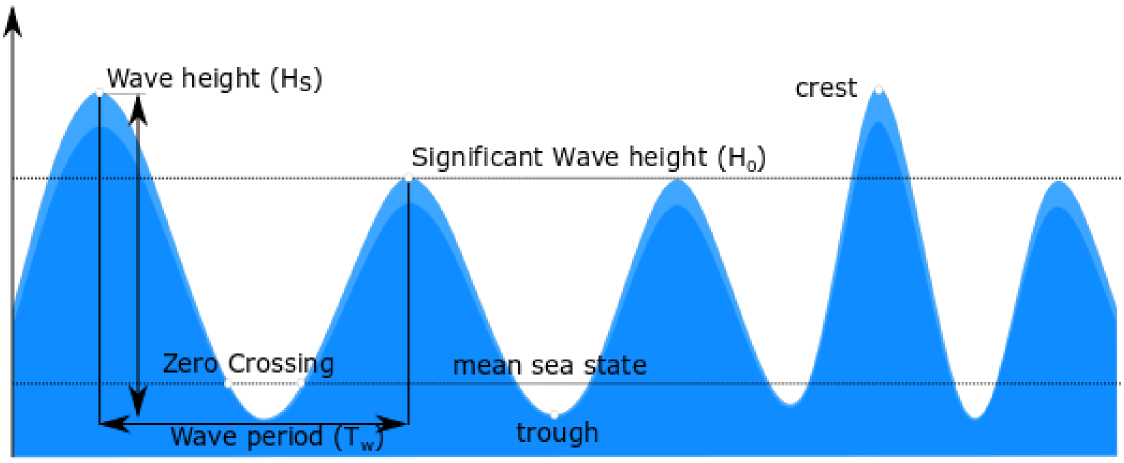

Figure 2.9: Diagram showing the characterization of sea state through statistical methods described by Kuik et al. (1988) and Earle (1996) and Welch (1967). A wave consists of a maximum vertical point (crest) and a minimal vertical point (trough) with the distance between the two points referred to as the wave height (H_0). The period between consecutive crests of a similar frequency is referred to as the wave length and the point where a wave crosses the mean sea state level is the zero crossing. From a statistical analysis, the significant wave height is the average of the top third of observed wave heights in a given time period. (Kuik et al., 1988).This diagram is based off the figure by (Mazarakis, 2019).

Devices that measure wave parameters such as significant wave height, wave spectra or ocean states, incorporate a sensor that measures the vertical acceleration and roll, pitch, and yaw in discretised space (Earle, 1996). These parameters can be measured using an accelerometer for axial acceleration and a gyroscope for rotational velocity (Fong et al., 2008). These devices are typically integrated circuits manufactured using micro electro-mechanical systems (MEMS) and are often combined to form an inertial measurement unit (IMU) allowing for 6 degrees of freedom from a single device (Fong et al., 2008). IMUs can also be expanded to include a magnetometer which measures magnetic bearing in 3 axis (Ahmad et al., 2013). IMU selection is dependent on the following factors[4]:

1. Package size
2. Accuracy
3. Response rate
4. Degrees of freedom

Figure 2.10: Diagram showing examples of the different types of inertial measurement systems (IMUs) available for commercial use such as (A) an Attitude Heading Reference System (AHRS) VN100 (VECTORNAV, 2019) used by (Rabault et al., 2019), (B) an analog capacitive accelerometer 8330B3 Servo-KBeam accelerometer used by (Kohout et al., 2015) (Kistler, 2011) and (C) a 9 degree of freedom MPU9520 (TDK InvenSense, 2016) used by (Kohout et al., 2015).

Ahmad et al. (2013) show that package size can limit the applications of the IMU. Additionally, IMUs require careful calibration and filtering to reduce the effects of bias offsets as well as low and high frequency drift (Fong et al., 2008). More advanced filtering methods have been developed to improve the accuracy of IMUs such as Kalman filters (Simon, 2001) for positional estimates or Real-Time Kinetic Fusion (RTK) for velocity (Meng et al., 2014). While important to the integrity of IMU data, these methods are usually implemented in software which is discussed in the upcoming sections. Finally, the degrees of freedom (DOF) influences the application of the IMU. The magnetometer is used to improve the accuracy of the gyroscope measurement and account for low frequency noise (drift) (Ahmad et al., 2013). However, the magnetometer is sensitive to magnetic distortion which can affect the measurements. Kohout et al. (2015) encountered magnetic distortion during the SIPEX II deployments in September 2012 which rendered the magnetometer readings useless. In this section, the IMU is integral to deriving a time-series representation of inertia to calculate wave data as described above. However, another

[4]Ahmad et al., 2013.

application relevant to the literature is using IMUs to improve navigation (Ahmad et al., 2013). An IMU can be coupled with a Global Positioning System (GPS) device to determine position in areas with poor signal which can assist greatly with determine ice drift (discussed in Section 2.3.3). Based on these considerations, Table 2.7 shows the IMU component selection for each device.

;

Table 2.7: Comparison of the inertial measurement systems selected for each device showing the sensors included as well as the degrees of freedom.

Device name	Inertial Measurment Unit	Sensors	Degrees of freedom
WIIB	VectorNav VN-100	Accelerometer Gyroscope Magnetometer	9
WIIOS	Kistler 8330B3 Servo-KBeam	Vertical acceleration	1
	TDK InvenSense MPU9250	Accelerometer Gyroscope Magnetometer	9
NDWB	SBG IG-500N	Accelerometer Gyroscope Magnetometer	9
SKIB	LIS3DH	Accelerometer	3
SIMB	Bosch Sensortec BNO055	Accelerometer Gyroscope Magnetometer	9
Polar ISVP	None	-	-
Trident	None	-	-

As mentioned previously, systems such as WIIOS and WIIB have built their purpose around wave measurements and therefore have specified high powered, high accuracy IMUs for wave measurements. However, WIIOS buoy separates itself from WIIB by having a cheaper complimentary 9 DOF IMU to complement the measurements (Kohout et al., 2015). SWIFT buoy and the NDWB buoy use an integrated system known as an Inertial Navigation System (INS) with the former containing an SBG Elipse AHRS (Thomson, 2012) and the latter containing a SBG IG-500-A1G2 (Doble et al., 2017). This device contains a GPS and an onboard processor for RTK fusion and Kalman filtering whereas other devices use an external processor for filtering. The SIMB Buoy is the only buoy on the list that has an IMU for non-wave related measurements. It uses a cheaper Bosch BNO055 which is used solely for measuring the orientation of the device.

Software processing

An IMU is a powerful device however extensive software processing is required to extract key parameters (Ahmad et al., 2013). Examples of software processing algorithms are shown in Kuik et al. (1988) and Earle (1996)[5] for wave processing algorithms. Additionally, as mentioned previously, advanced filtering techniques are required to reduce the effects of low and high frequency noise. In this subsection the software processing strategy for each device given for extracting the desired parameters shown in Table 2.4.

Table 2.8: Comparison of sampling strategies implemented in each device. This includes the desired measurands, sample rate and sample period of each IMU session.

Device name	Degree of freedom used	Sample rate [Hz]	Sample period [minutes]
WIIB	Vertical acceleration Pitch Roll	10	25
WIIOS	3-axis acceleration 3-axis gyroscope 3-axis magnetometer Vertical analog acceleration	2	11
NDWB	3-axis acceleration 3-axis magnetometer Heave Roll Pitch	1	Continuous
SKIB	3-axis acceleration	25	10
SWIFT	3-axis acceleration Tilt Horizontal rotation	5	9
SIMB	Tilt Orientation	-	-

Rabault et al. (2019) extract wave parameters by passing the raw time series data through an Extended Kalman Filter running at 800 Hz then through a low pass filter. Wave spectral data is calculated using the method by Earle (1996) where co-spectra were calculated using the method by Kuik et al. (1988). Significant wave height was calculated by double integration using a Fast Fourier Transform (FFT). Sampling is performed at 10 Hz to satisfy the Nyquist sampling criteria for open ocean waves as described in (Earle, 1996; Rabault et al., 2019).

Kohout et al. (2015), however, opted for a reduced sampling rate of 2 Hz over a shorter sample time. This was achieved by oversampling IMU data at 640 Hz then down-sampling the data through a multistage decimator (Kohout et al., 2015). Before each decimation, data were filtered using a Butterworth filter at 8 Hz with a cut-off frequency of 2 Hz, then once again at 40 Hz. Significant wave height is calculated by double integration using the Welch-Earle method (Earle, 1996; Welch, 1967) multiplying the transformed data set by

[5]See Appendix A.3.2.

a response weighted function to remove low frequency drift. Finally, the Longuet-Higgens parameters are calculated thereby characterising wave in ice activity.

Doble et al. (2017) did not apply any data processing algorithm to the raw time series as it is transmitted directly over Iridium. However, the raw time series is filtered using an Extended Kalman Filter running at 10 Hz.

The SKIB collects data from a sample window which is processed using a classical RC filter to attenuate frequencies below 0.04 Hz. Thereafter, Earle (1996) spectra and co-spectra calculation are then applied.

The SWIFT buoy is the only device that used multiple sensor types for sea state calculation. Additionally, data was collected more frequently in short intervals (9 minute sample periods every 12 minutes) which include Doppler profiles, camera images and IMU data. The inertial navigation system (INS) outputted a real-time kinematic (RTK) fusion data set where IMU data was passed through a Coning & Sculling Extended Kalman Filter running at 1 kHz (Thomson, 2012) while the Doppler profiler was sampled at 8 Hz. Turbulence profile was calculated through time-averaging and data fitting of the Doppler profile. Then, the ocean current state was calculated using the Stokes drift equation over a time-averaged velocity series. Finally, wave data were calculated through image processing from a still of the sea state taken from an onboard camera.

The SIMB uses the IMU in a non-critical manner. The device transmits tilt and orientation metadata describing the current status of the SIMB (Planck et al., 2019). While no method has been described by Planck et al. (2019) to calculate tilt, it can be achieved by measuring the orthogonal acceleration values over an angle of ration and taking the inverse tangent of the resulting value for each axis (Tuck, 2007).

Therefore IMUs are integral for performing sea state calculations and measuring wave spectra, a sufficient processor is required to filter and process the data. Therefore, significant consideration should be given to coupling a powerful processor with a sufficiently powerful inertial measurement unit.

2.3.3 Measurement of ice drift using GPS

This sections discusses the technology and techniques used for determining ice drift. The predominant approach towards understanding modeling ice drift is by using the techniques presented by Hibler (1979)[6] where kinematic data are used to study ice drift dynamics and calibrate the ice drift model. Additionally, Leppäranta et al. (2001) present two methods for collecting ice drift data. The first method utilises measurement beacons attached to the ice floes to track trajectories. The second method uses imaging devices such as radar, and satellites to determine ice displacement (Leppäranta et al., 2001).

[6]See Numerical Modeling in Appendix A.1

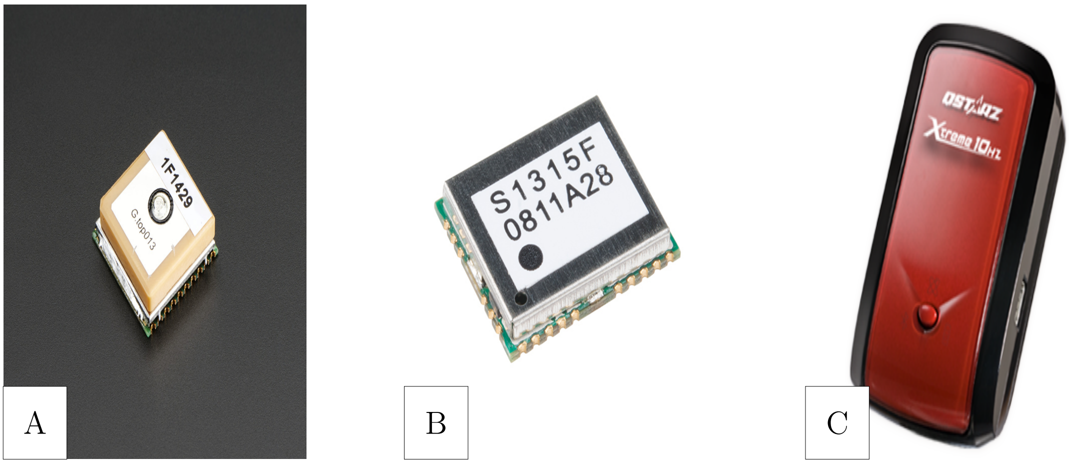

Figure 2.11: Diagram showing examples of the different types of global positioning devices available for commercial use such as (A) MTK3339 (image source: (Adafrut, 2014)) , (B) SkyTraq S1351R (image source: (SparkFun, 2017)) (C) Qstarz BT-Q1000eX (image source: (QStarz, 2013))

The discussion of modern technology for ice observations from Chapter 1.1 showed that observations from satellites such as OSI-SAF and METSAT are unsuitable for measurements (Galin et al., 2011; Leppäranta et al., 2001) due to their low spatial resolutions. Hence, a need arises for in situ drift measurement devices. Global positioning systems (GPS) have been the standard for ice drift measurements (Leppäranta et al., 2001) as they are capable of measuring data at relatively high temporal resolutions ranging from 15 minutes (Alberello et al., 2019) to 25 minutes (Rabault et al., 2019) as opposed to the limit of 3 hours (Alberello et al., 2019). This section provides an overview of GPS technology and how the devices have been used for measuring positional or drift data.

Overview of GPS

The principles that govern GPS have remained unchanged since its inception in 1973 (Spilker Jr et al., 1996). The system consists of a satellite constellation that constantly broadcast their estimated position. A GPS device determines its position by matching a user-generated signal to that of four received satellites and comparing the phase difference to an on-board crystal oscillator (Spilker Jr et al., 1996). This technique is called ranging and four satellites spread in a uniform geometry will allow for a device to calculate latitude, longitude, altitude and time to a relative degree of accuracy. The number of unknown signals correlates to the number of satellites required. Generally, a GPS device will have a lesser degree of accuracy than the satellites. Hence, an incoming signal can be used to correct the device's clock [7].To accurately predict the satellite's trajectory, satellite ranging is performed by a network of global monitoring stations which calculate the future position and send it back to the satellite. GPS signals are transmitted on two frequencies: 1575.42 MHz and 1227.46 MHz (Spilker Jr et al., 1996). These are synchronously generated signals and allow a device to correct for ionospheric distortion. These bands carry modulated signals which are as follows: (Spilker Jr et al., 1996)

[7] provided altitude or time are already known (Spilker Jr et al., 1996)

1. Clear Acquisition (CA) Code: This is a short code transmitted at 1.023 MHz and is used to request the Standard Positioning Service or SPS.

2. Precise (P) Code: This is a much longer acquisition code. This signal is transmitted at 10.23 MHz which is 10 times the rate of a CA code. This results in a much more accurate signal with less noise. This signal allows for the acquisition of Precise Positioning Service. However, this service is not available to unauthorised users and cannot be spoofed. As a result, this signal requires additional decryption.

Spilker Jr et al. (1996) also mention that military operators can degrade GPS signals which result in decreased accuracy from 20 m up to 100 m. The reduction of these accuracies requires differential GPS techniques. However, due to the scope of this projects, this section will not be explored any further. Finally, once the acquisition signal is transmitted, the GPS device begins modulating at 50 bits/s allowing the satellite to transmit its position as well as clock correction information to the device.

The GPS constellation consists of 24 GPS satellites. These are configured into three rings of eight satellites orbiting at different latitudes. These orbital altitudes were selected as 10.98 Nautical Miles (Spilker Jr et al., 1996). This altitude was chosen to optimise user visibility with the number of crossings over United Sates ground stations, and cost of launching the satellites (Spilker Jr et al., 1996). These satellites carry onboard atomic clocks for stability at 1×10^{-13} resolution. This allows for extremely accurate signaling as well as allowing for much more predictable time and position signals (Spilker Jr et al., 1996). To achieve this, these atomic clocks are made out of either Cesium or Rubidium. Also, a frequency correction at 4.5×10^{-10} Hz is provided to correct for relative shifts.

GPS error modeling

As mentioned in the previous section, GPS signal accuracy is greatly affected by Earth effects and satellite distribution. The main source of distortion is attributed to the Earth's ionosphere (Spilker Jr et al., 1996). The ionospheric free electronics cause a delay in the modulated signal which is proportional to the sum of electrons along the signal's trajectory and inversely proportional to the signal's frequency squared. This delay is modeled as the product of a theoretical 90° delay (Zenith delay) and a function of the elevation angle (obliquity factor). This results in a ratio of between 1.0 to 3.0 at small elevation angles (Spilker Jr et al., 1996). This results in delays of 3 m (often at night) to 20 m (after midday). These delays result in errors in positional accuracy as shown in figure 2.12 which can increase the measurement confidence interval resulting in an unreliable positional reading (Spilker Jr et al., 1996). Fortunately,These delays are usually resolved by satellite correlated positions.

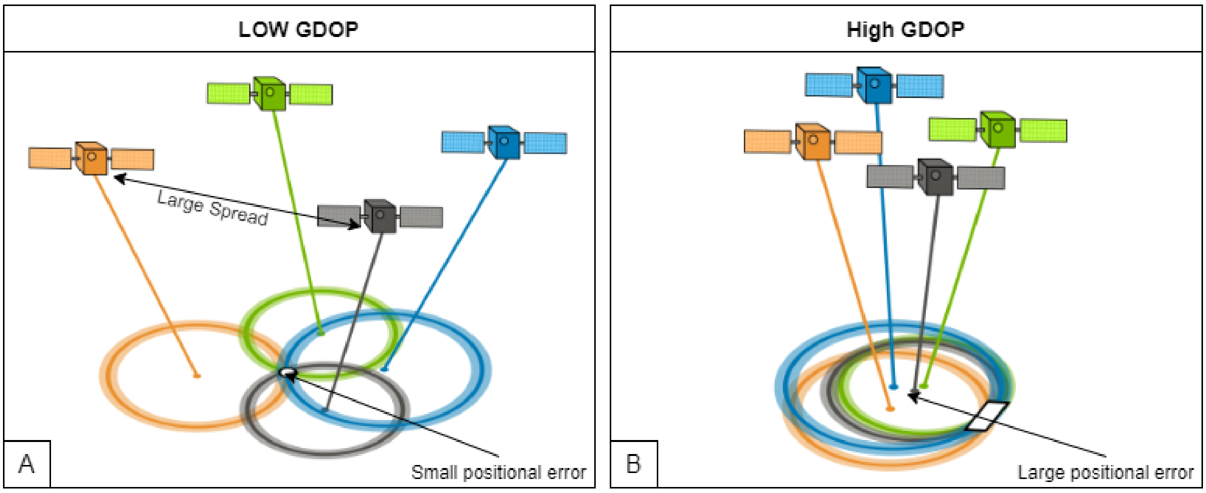

Figure 2.12: Diagram showing how satellite distribution affects the positional estimation. Global navigation satellite system (GNSS) satellites have an associated inaccuracy which is represented by the circles. Locking on to more than one satellite reduces these inaccuracies by interpolating the position from the phase differences between satellites. This value is greatly affected by the spread of satellites as a larger spread results in a more accurate positional estimate (A) while a shorter satellite spread results in a less accurate positional estimate. A measure of this inaccuracy is called the dilation of procession (DOP). Figure was adapted from images by (GIS Geography, 2020) for A and B.

Correction can be performed in one of two ways:

1. Transmission of Ionospheric model parameters as part of the message to the device and calculating the offset using that
2. Using the two previously mentioned transmission frequencies directly measuring the delays in each broadcast frequency and estimating the position (Spilker Jr et al., 1996).

Navigation errors are characteristic of GPS performances. These errors are affected significantly by satellite spread and ranging errors. Assuming the incoming signal is uncorrelated with a mean of zero, the RMS positional error is calculated as:

$$RMS_{error} = (\text{Geometric Dilution})(\text{RMS Ranging errors}) \tag{2.1}$$

The geometric dilution of precision (GDOP) is the error in the precisional spatial and temporal measurements, which is inversely proportional to the volume of the shape formed by four satellite (Jwo, 2001). Jwo (2001) outlines the procedure for the calculation of this value which is shown in Appendix A.2. A GPS position is calculated from the incoming signal of three or more satellites. This is because at least three satellites are required for a valid three-dimensional positional fix and four satellites for an accurate time fix (Jwo, 2001; Spilker Jr et al., 1996). However, if the internal satellite clocks are not synchronized, a clock offset appears resulting in a dilution in the temporal accuracy of the GPS signal.

This value is called the time dilution of precision (TDOP). Signal noise can also contribute to spatial inaccuracies in estimating the one-dimensional vertical position (VDOP), the two-dimensional horizontal position (HDOP) or the three-dimensional position (PDOP). DOP values represent the ratio of measurement errors to pseudo-range measurement error[8] where the higher the DOP number, the larger the measurement error and hence, the more inaccurate the positional fix will be (Tahsin et al., 2015). A description of DOP accuracies is provided in Table A.2.

Table 2.9: Table showing the ratings for a dilation of precision (DOP) measurement with a numerical range corresponding to a rating as shown by Tahsin et al. (2015). These ranges provide context for positional accuracies associated with GPS measurements with a DOP of 1 being an ideal reliable measurement with an associated small margin of uncertainty whereas a DOP of 20 is completely unreliable with a large uncertainty.

DOP Value	Rating
1	Ideal
2to 4	Excellent
4 to 6	Good
6 to 8	Moderate
8 to 20	Fair
20 to 50	Poor

Finally ranging errors are shown to come from 6 sources (Spilker Jr et al., 1996):

1. Satelite ephemeris
2. Satelite clock
3. Ionospheric group delay
4. Trophospheric group delay
5. Multipath scattering
6. Hardware/software errors

Theses errors become much more prominent in the polar region due to higher Ionosopheric total electron current (TEC) than mid-latitude regions (Bishop & Klobuchar, 1990). Furthermore, Bishop and Klobuchar (1990) show that these errors can be corrected by coupling statistical models with satellite readings to reduce these errors. However, no adequate models exist for the polar region. Furthermore, the discusion in section 2.2.3 shows that freezing temperatures and ice dynamics can be significant sources of failure for GPS signal acquisition (Doble et al., 2017). These sources of error need to be accounted for when incorporating a GPS device into an in situ remote sensing device for the Southern Ocean.

[8] See Section A.2

GPS component selection

The component selection for each device is shown in Table 2.10 below.

Table 2.10: Comparison between different GPS devices, sampled data and periods between samples implemented by each device.

Device Name	GNSS device	Data sampled	Period between samples [minutes]
WIIB	Adafruit MTK3339	Geographical position	25
WIIOS	Adafruit MTK3339	Latitude (decimal degrees) Longitude (decimal degrees)	180
NDWB	SkyTraq S1351R	Geographical position	60
SKIB	Adafruit MTK3339	Geographical postion	10
SWIFT	Qstarz BT-Q1000eX	Geographical position Horizontal velocity	0.003
SIMB	Adafruit MTK3339	Geographical position	60
Polar ISVP	Jupiter F2 Module	Geographical position	180
Trident	Unspecified GPS	Geographical position	0 to 5 5 to 60 60 to 1440

Table 2.10 above shows the GPS receivers implemented in each system as well as measurements of interest. The most common GPS receiver is the Adafruit MTK3339 Adafrut (2014). Additionally, all devices have fixed transmission periods between samples except the Trident buoy which has user configurable periods that can be set from a couple of minutes to hours. Most devices use the GPS for positional location however, SWIFT buoy measures horizontal velocity in addition to vertical position (Thomson, 2012). Thomson (2012) justify this by stating that the accuracy of horizontal velocity measured by a GPS is accurate enough (± 0.5 ms^{-1})to be used for determining the orbital motions of waves. Kohout et al. (2015) and Rabault et al. (2019) provide the measurements recorded by the GPS. However, very little discussion is given regarding the performance and accuracy of the device. Doble et al. (2017) showed that during their year long deployment, 14 buoys maintained a near perfect satellite signal acquisition however, software issues with the GNSS receiver resulted in a failure to obtain measurements in five systems. However, Doble et al. (2017) had implemented two-way Iridium communication and were able to partially overcome this set back by transmitting commands that performed a software reset on the GPS receiver. Additionally, two devices lost signal for 6 days while another two devices lost signal for 62 days and 41 days respectively (Doble & Bidlot, 2013). This shows that acquisition failures can cause temporal gaps in data and therefore, need to be reduced to provide robust data sets.

Each ice floe follows a unique trajectory (Leppäranta et al., 2001) and individual trajectories combine to form a continuum. It has previously been believed that sea ice drift has been linked strongly to significant wave events (Alberello et al., 2019). An experiment was conducted by Alberello et al. (2019) to measure the drift of sea ice during a cyclone event. Here it was found that wind velocity is the dominant driver of sea ice drift (Alberello et al., 2019) causing ice drifts of up to 0.75 ms^{-1} (Alberello et al., 2019). Sea ice drift speed is extremely sensitive to sampling rates. (Alberello et al., 2019) where sampling rates of 6 hours can underestimate the ice velocity by 5% (Alberello et al., 2019) and up to 20% for 12-hour sample rates. The consequence is reduced, near unusable, estimates of sea ice velocity components as well as drag coefficient and wind factor estimates. High temporal resolutions are capable of capturing important, inter-daily activities such as ice oscillations. Alberello et al. (2019) state that to accurately capture sea ice dynamics, a temporal resolution of at least 3 hours is required (Alberello et al., 2019). Table 2.10 shows that all devices sample GPS at a rate of 3 hours or less thereby fulfilling this criteria. This not only allows for the capture of accurate drift speeds but provides an accurate characterisation of instantaneous velocities and Coriolis forces (Alberello et al., 2019).

2.3.4 Temperature sensing and measurement

As discussed in Chapter 1.1, Antarctic sea ice follows a unique formation cycle with different phases marked by changes in season. Sea ice formation additionally is affected by environmental factors which can arise from one of two sources: Long-period seasonal cycles (Barber, 2005) which affect snow growth and sea ice formation, and short term extreme weather events (Alberello et al., 2020; Vichi et al., 2019) which affect the thermodynamics of the formed ice and results in ice drift and collisions (Arrigo & Thomas, 2004). One key measurement for correlating environmental effects to sea ice formation is air temperature. Barber (2005) show that the melting and freezing phases in the sea ice life cycle is preceded by increases in air temperature above freezing and decreases in temperature below freezing respectively. In addition, Vichi et al. (2019) show that warmer air temperatures were observed during polar events. This shows that temperature is critical measurement for understanding sea ice lifecycles and the effects of ocean processes. Additionally Doble et al. (2017) and Kohout et al. (2015) have discussed the significance of sea ice melting. This was considered a significant phase of sea ice and was classified as a phase in the development of their buoy. Hence, we turn to temperature sensing as a solution to understanding the effects of temperature on Antarctic sea ice.

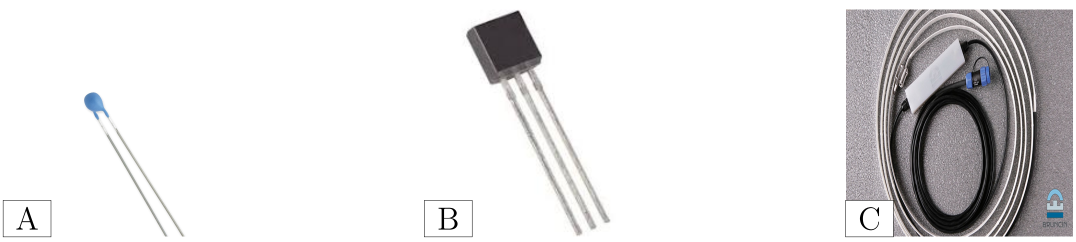

Figure 2.13: Examples of temperature sensors employed by remote sensing devices. These types of devices include (A) thermistors such as the PR303J2 (image source: (Littelfuse, 2021)), (B) digital temperature sensors such as the DS18B20 (image source: (Digikey, 2021)) and (C) digital temperature chains (DTC) such as the Bruncin DTC (image source: (Bruncin, 2021))

Temperature sensing technology is commonly used for thermal compensation as measurements such as pressure and humidity are dependent on environmental temperature (Mansoor et al., 2015). Thermal sensing technology exists in a variety of forms. However, choice of sensor is heavily dependent on the application i.e. the object to be measured, the material state and the type of contact with the sensor (Childs et al., 2000; Mansoor et al., 2015). There are three main categories of measurement techniques (Childs et al., 2000):

1. Invasive measurements: Direct contact with an object of interest. This method is suitable for the measurement of objects in liquid or gas states. This category encompasses thermoelectric devices, liquid in glass thermometers, electronically resistive devices as well as semiconductor devices (Mansoor et al., 2015).
2. Semi-invasive: Using the thermal measurement medium on an object and observing the effects of temperature such as thermal paints. Note: measurements are not directly taken from the object but rather the properties of the medium.
3. Non-Invasive: Object is measured from a distance using a device such as an infrared camera or acoustic thermography.

In addition, sensor selection is based on the range, accuracy, resolution and precision of the device to ensure correct use An overview of different electric sensors is given below (Childs et al., 2000) A full discussion of the types of sensors is provided in Appendix 2.11 where the types of technology, advantages and disadvantages are provided. Additionally, the technology discussed has been selected for its implementation in the remote sensing devices shown in table 2.11 below.

Table 2.11: Comparison of the different components used by each device for temperature measurement as well as the sensor type and the measurement objectives of the device. Each device measures temperature of a different process. For example: the WIIB measure air temperature whereas a device like the SIMB measures temperature profiles of ice floes in addition to air temperature.

Device name	**Temperature sensor**	**Sensor type**	**Measurement objective**
WIIB	VectorNav VN-100	Digital temperature sensor	Air temperature
WIIOS	Maxim Integrated DS18B20	Digital temperature sensor	Air temperature
NDWB	SBG IG-500	Digital temperature sensor	Internal ambient temperature
SKIB	None	none	None
SWIFT	Aquadop profiler	Thermistor	Water temperature
SIMB	DS18B20	Digital temperature sensor	Air temperature
	Bruncin DTC	Digital temperature chain	Ice temperature profile
Polar ISVP	Littelfuse PR303J2	thermistor	Sea surface temperature
Trident	unspecified	Not reported	Air temperature

As shown in Table 2.11, digital temperatures sensors are the most common with thermistors being the second most prevalent. Thermistors are semi-conductor based temperature sensors whose resistance changes as a function of temperature which can be described with a negative temperature coefficient. These devices have a typical accuracy of 0.05° C to 0.01° C with a temperature range of $-100° - 300°$ C (Childs et al., 2000). These devices have a fast response and are cheaper than their counterpart: the resistance temperature device (RTD) (Childs et al., 2000). However, they aren't strong enough to reach the desired operating ranges as standalone devices and require additional circuits (Tong, 2001). Additionally, these devices have a larger measurement uncertainty as they are more susceptible to noise (Childs et al., 2000).

Another common technology basis for temperature sensing is using a semi conductor temperature device (STD). These consist of diode and transistor based circuits whose voltage changes with temperature. These devices have measurement range from -55 $°C$ to 150 $°C$ with an accuracy of $0/08°c$. Additionally, these devices are suitable for MEMS-based circuits and high powered electronics (Willander et al., 2006). These devices are readily available with a reliable accuracy however, the performance of the device is heavily dependent on the material used. For example, silicon has a low temperature stability but a lower voltage output (Childs et al., 2000).

Table 2.11 shows that most devices use digital temperature sensors for ambient air temperature measurement with thermistors begin the second temperature sensors type as used by Thomson (2012). Most device use temperature sensors integrated into high powered IMU/AHRS systems, as is the case with WIIB and NDWB. While the SWIFT buoy and the Polar ISVP both utilise the same sensing technology however the Polar ISVP used a standalone Littelfuse PR303J2 whereas the SWIFT used the temperature sensor onboard the Nortek Aquadopp Profiler which is, primarily, a current profiler. This shows that temperature sensing was not a primary focus for this device design as there is a lack of discussion regarding the performance of the temperature sensor in the literature.

2.3.5 Atmospheric pressure sensing and sensors

There has been an increased demand for in-situ environmental monitoring as mentioned by (Alberello et al., 2019; Kennicutt et al., 2019; Kennicutt et al., 2014; Kennicutt et al., 2016; Vichi et al., 2019). It can provide insight into wind currents and storm events as well as predict trajectories of these storms. In addition, atmospheric pressure is crucial for characterising atmospheric-ocean process such as tropical storms which create areas of low pressure during their trajectory (Vichi et al., 2019). Current devices have employed pressure sensing techniques which have been critical for determining accurate AHRS measurements (VECTORNAV, 2019) in addition to environmental monitoring. Examples of pressure sensing devices are shown in Table 2.12 below.

Table 2.12: Comparison of the different pressure sensing components used by each device as well as the measurement objective guiding the selection of the component. "Not Reported" is given where a device includes a pressure sensor but provides no information to its use. "-" is given where a column does not apply to the device. "None" is given where a device does not contain a pressure sensor.

Device Name	Pressure sensor	Sensor type	Measurement objective
WIIB	VectorNav VN-100	Digital barometric pressure sensor	Atmospheric pressure
WIIOS	None	-	-
NDWB	NXP MXP-5100-AP	Piezoresistive silicon pressure sensor	Atmospheric pressure
SKIB	None	-	-
SWIFT	SBG Eclipse-N	Not Reported	Not Reported
SIMB	Bosch Sensortec BME280	Digital barometric pressure sensor	Atmospheric pressure Humidity
Polar ISVP	Vaisala PTB100	Silicon capacitive barometric sensor	Atmospheric pressure
Trident	None	-	-

Table 2.12 above shows the common pressure sensing types used in remote sensing. While different devices are reported, Eaton and Smith (1997) shows that the basis of modern sensors are built around MEMs with diaphragm-based sensors being the most common system. These devices consist of a miniature diaphragm mounted in a specific way. Pressure is determined by measuring the deflection of the diaphragm against a reference pressure and converting the result into an electrical signal. While these devices are common for sensing pressure (Eaton & Smith, 1997), the diaphragm is susceptible to plastic deformation which can affect the long term reliability of the device (Eaton & Smith, 1997). Furthermore, mechanically stronger diaphragms have a non-linear relationship with current which can result in inaccuracies from calculation errors.

Another pressure sensor type is a piezoresistive sensor which is a semiconductor based device. These devices are diaphragm-based MEMs sensors whose resistance changes with a change in stress (Eaton & Smith, 1997). A major advantage of these devices is the linear relationship between resistance and pressure. They are robust with reduced hysteresis and measurement drift effects and exhibit elastic properties at low temperatures and are stronger than strain gauges (Eaton & Smith, 1997). However, device accuracy is significantly affected by thermal expansion which causes thermal drift. These devices are also susceptible to resistor noise therefore requiring resistors with identical temperature characteristics. Furthermore these devices require extensive compensation techniques which can increase the complexity of the device.

While pressure is important for understanding atmospheric processes, Table 2.12 shows that it is the least critical component for in situ remote sensing. The WIIOS, SKIB and Trident sensors do not include a pressure sensor at all. The consequence is that these devices are not suitable for characterising the effects of climate on sea ice as well as capturing the/predicting severe weather events such as the cyclones discussed in Vichi et al. (2019). The SWIFT buoy includes the capability of pressure sensing. However, do not sample the sensor for standalone pressure measurements. The devices that include pressure measurements focus on measuring atmospheric pressure through digital barometric pressure sensors (Planck et al., 2019; Rabault et al., 2019), piezoresistive silicon sensors (Doble et al., 2017) or silicon capacitive sensors (Metocean, 2016). Examples of these sensors are shown in figure 2.14

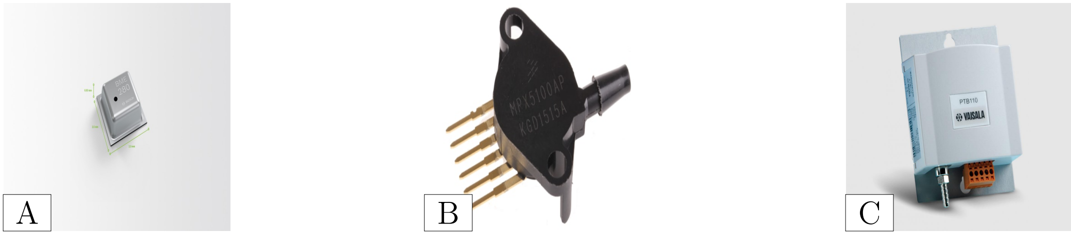

Figure 2.14: Examples of pressure sensing technologies using a diaphragm based MEMS with different methods of measuring the strain. These are piezoresitive sensors: (A) the BME280 (image source: (Bosch Sensortec, 2021)), (B) the MPX-5100-AP (image source: (RS Components, 2021)) or capacitive sensors: (C) the PTB100 (image source: (Vaisala, 2018))

This shows that silicon-based pressure sensors are the most commonly used for remote sensing. Eaton and Smith (1997) discuss the importance of micro-machined pressure sensors and provide an overview of various sensors that have been used in remote sensing devices as shown in Table 2.12.

2.4 Conclusion

From the system analysis, we can see that all devices were successful in communicating remotely with a user through the Iridium satellite network due to its high area coverage and reliability. However, due to network and bandwidth constraints, most devices compensated for this by implementing computationally intensive algorithms to compress data into the required bandwidth, the popular choice for network modems is the 9603 which is ideal for its low power consumption, small form factor and relatively low cost however it only allows for short burst data transmissions. For continuous transmissions, the 9523 modem is ideal.

Systems were able to operate remotely for long periods of time using batteries as a power source. Lithium batteries and alkaline batteries were the most prevalent as primary power sources allowing devices such as the WIIOS to survive for a maximum of 39 days. Doble et al. (2017) showed that in the Arctic marginal ice zone by coupling a solar power to a secondary lead acid battery, the device could survive for up to a year without human intervention. However, Rabault et al. (2020) achieved lower surviviabilty even with an onboard solar panel. Additional energy harvesting techniques are required for secondary power source to be viable.

In spite of advances in power optimisation, the Marginal Ice Zone is a dangerous region. A significant number of devices were reported by Doble et al. (2017) to have failed when devices froze over and failed to recover during sea ice melt. Additionally, polar storms and large swells caused the WIIOS buoys to be offline during their deployments (Alberello et al., 2019; Kohout et al., 2015). Additional sources of failure have been attributed to freezing over Rabault (2018) however, this was due to the device being placed in the ground allowing it to be covered by snow growth and flooding (Barber, 2005). Additionally, Rabault et al. (2019) reported failures due to rafting and ridging of ice floes which critically damaged devices.

From the system analysis, we can determine that the most important measurement objectives are:

- Ice drift
- Wave in ice measurements
- Ambient temperature
- Atmospheric pressure

Wave analysis is the most computationally expensive measurement objective as Table 2.8 show that raw IMU time series measured by each wave sensing device was sampled above 2Hz (Kohout et al., 2015). Advanced filtering techniques were required to compensate for the effects of low drift and biases. Some devices achieved this by using components with integrated filters such as the VN-100 AHRS sensor, However, these components are expensive and resulted in a higher overall cost for the device (Guimarães et al., 2018). Additionally, devices such as WIIOS and SWIFT required more expensive and powerful processors to compensate for higher data rates and advanced processing algorithms.

Additionally, all remote sensing devices in this review used a GPS to measure sea ice drift showing that these devices are reliable enough to perform these measurements (Doble et al., 2017). A sample time of at least 3 hours between GPS measurements is required to accurately capture sea ice dynamics such as oscillations and collisions. Thomson (2012) show that GPS velocity measurements are suitable for wave measurements in addition to telemetry and used these measurements to determine the orbital motion of waves. However, the positional accuracy of GPS is not suitable for measuring significant wave height as the uncertainty in positional measurements is too high ($\pm$ 5 m). GPS readings are affected by ionospheric interference which causes a phase delay resulting in a dilation of precision (DOP), this can also be caused by the spread of satellites, azimuth and number of satellites used to take measurements. Hence, these measurements form a critical part for statistical analysis of GPS signals as this section was under-reported in the current literature.

Environmental sensing is critical to determining the conditions around sea ice formation. Temperature and pressure changes are key indicators of short term weather events such as polar cyclones and as such, all remote sensing devices in this review employ some form of temperature measurement either actively through components such as thermistors, and silicon temperature devices or passively embedded in higher powered sensors such as an AHRS. Additionally, the effects of temperature sensing on atmospheric temperature measurements were significantly under-reported in the literature as was the effect of pressure sensing. Pressure sensing was also the least critical objective for the devices as this device was excluded from three out of eight devices while the SWIFT buoy had pressure sensing capabilities, this feature was not used. Hence, more research is required to fill in this knowledge gap to understand the effects of environmental sampling and their impact on climate measurements.

In conclusion, while the literature shows breakthroughs in low cost in situ remote sensing in the marginal ice zone, some of the effects remain unknown. Devices are still extremely specialised. However, open-source, off the shelf devices can pave the way for more accessible, more affordable devices thereby increasing access to science and increasing our understanding of the marginal ice zone.

Chapter 3

Design methodology

3.1 Design overview

In Chapter 2, the critical areas, challenges and techniques used by remote sensing devices to meet the objectives outlined in 1.1 were discussed. Remote sensing devices aim to increase the temporal and spatial resolution of Southern Ocean data sets by increasing survivability and concentration of remote sensing platforms. The challenges identified in Chapter 2 were the sea ice dynamics which can damage the device. Furthermore, strong wave activity and low temperatures which can freeze the device and degrade the battery life. A key difference between each device was the measurement objectives as shown in Table 2.4 which dictated the sensors, processing strategy and functionality of each system.

This section outlines the steps taken to identify the user requirements and translate them into hardware subsystems. The design phase began with a user requirements analysis. These requirements resulted in well-defined measurement objectives for the device and the selection of subsystems critical to the device functions. Then, a high-level system diagram was created to show the interaction of the subsystems within the system. This allowed for the selection of hardware components to satisfy the requirements for each subsystem. Finally, to ensure that the subsystems met the user requirements, a set of acceptance tests were derived.

3.2 User Requirements

The user requirements analysis began with an identification of the project stakeholders shown in Appendix B.1. Through constant engagement with the primary stakeholders, a set of user requirements was generated which identified the objectives the device would need to meet. The formatting, presentation and selection of these user requirements was done in accordance with IEEE Standards[1]

[1] C/S2ESC - Software and Systems Engineering Standards Committee, 1996.

Table 3.1: User requirements obtained by meeting with the principal stakeholders. These will be used to determine the desired functionality of the buoy

User Requirement ID	Description
UR001	System must be able to withstand the Southern Ocean climate.
UR002	System must be able to transmit data remotely without additional infrastructure or user input.
UR003	System shall provide higher temporal and spatial resolution data.
UR004	System must be capable of measuring ice floe dynamics and environmental conditions surrounding sea ice formation.
UR005	System must be user-friendly and easy to deploy.
UR006	System Must be cost effective.
UR007	System must be able to store and process data in an organised manner.

3.2.1 Analysis of UR001

System must be able to withstand the Southern Ocean climate.

Kohout et al. (2015) encountered 7 m swell and 25 ms^{-1} winds during their deployment in the marginal ice zone which lead to the immediate failure of one of their systems (Kohout et al., 2015). Strong wind and waves were also observed by Alberello et al. (2019) and Vichi et al. (2019) during their deployment which has been attributed to multiple cyclonic events coinciding with the deployment of the WIIOS buoys. The effects of wind and waves result in the delay of consolidation of sea ice at the edge of the marginal ice zone which created survivability challenges for the devices. Additionally, Alberello et al. (2020) showed that wind speed resulted in ice floe drifting at 0.35 ms^{-1}. Placing the buoy close to the surface of the ice subjects it to collisions, breaking and rafting which resulted in the failures of (Doble et al., 2017; Rabault et al., 2019). Snow and ice formation on the surface of the floe can bury the device (Doble et al., 2017) and constant wave energy on unconsolidated ice cause flooding which can further damage the devices. A device that is elevated above the surface while tethered to the floe can reduce exposure to these events however the buoy elevation must be at least 1 m to compensate for snow growth (Barber, 2005).

Furthermore, for a device to survive in the Southern Ocean, the software must contain a robust set of error checking for each module. The software should ensure that critical subsystems are functional and responsive while constantly providing feedback on statuses. Should a module be damaged or go offline, the software should flag this issue, identify the failure and attempt to rectify it. Alternatively, if the failure is critical, the device should flag the module as malfunctioning and continue to operate without it.

3.2.2 Analysis of UR002

System must be able to transmit data remotely without additional infrastructure or user input.

Kennicutt et al. (2016) shows a fundamental lack of infrastructure on the Antarctic continent including data networks. Operations taking place on sea ice are isolated from any resources that exist via Antarctic bases. Sea ice in the marginal ice zone is subject to conditions inhospitable to humans (Kennicutt et al., 2016). Therefore access to the buoys is limited once the device is deployed often making it difficult to retrieve. The life cycle of sea ice presents an additional access challenge through the consolidation of sea ice during the freezing periods and melting of the ice floes during the warming periods (Womack, 2020). Additionally, manned expeditions are typically inflexible (Kennicutt et al., 2016) resulting in additional challenges in retrieving the buoy and hence the data. Therefore, most devices deployed in the region are designed to be expendable ((Kohout et al., 2015; Rabault et al., 2019; Trident Sensors, 2021)). These device circumvent this by using satellite networks with global coverage such as Iridium[2] which allows the users to receive data and status updates from the buoy without needing to retrieve the devices.

The lack of user input implies that device routines and sub routines must be performed automatically. The device should control and sample sensors in a fixed, predictable manner ensuring that the correct data is sampled during the correct periods. Furthermore, the device needs to transmit data over the Iridium network. Therefore the software is required to control the interactions with the mode ensuring that it is functional. The software should condense data to fit the bandwidth of the device and ensure it is successfully uploaded to the transmission buffer. Finally, the software should be able to check for sufficient network availability and initiate a transmission. Should an error occur, the software needs to respond and handle it efficiently.

3.2.3 Analysis of UR003

System shall provide higher temporal and spatial resolution data.

Phases of the sea ice life cycle are defined by periods of freezing followed by periods of melting (Barber, 2005) with maximum extents occurring in winter (freezing) and summer (melting) respectively (Barber, 2005). The formation and consolidation of sea ice floes are influenced by atmospheric and oceanic processes resulting in the delay of sea ice consolidation (Alberello et al., 2020; Vichi et al., 2019). Each period coincides with a seasonal cycle typical lasting a few months (Alberello et al., 2019; Barber & Ursell, 1948; Vichi et al., 2019) which is the length of time a buoy needs to survive to provide sufficient data on a temporal scale.

Increasing remote sensing in the region is also required to provide spatial coverage (Alberello et al., 2020). Certain observational methods such as satellite observation are performed on a 10 m scale (Galin et al., 2011) where sea ice variability can scale down to the cm (Vichi et al., 2019). Doble et al. (2017) achieved large spatial coverage by deploy-

[2]See Chapter 2.1

ing the devices in clusters of five every 5 km. Additional deployments from (Vichi et al., 2019), (Kohout et al., 2015) and (Alberello et al., 2020) also achieved this by deploying multiple systems spaced 3 to 4 m apart (Vichi et al., 2019). Therefore increasing the spatial resolution can be achieved by increasing the concentration of devices in an area spaced apart.

For a remote sensing device to survive the required period, a built-in power source is required to maintain functionality without constant maintenance. This power supply primarily needs to come from a replenishable source. Doble et al. (2017) and Rabault et al. (2019) coupled battery arrays to a rechargeable power system which showed promise however, insufficient cloud cover (Doble et al., 2017) resulted in the solar panel being underutilised. As discussed in Chapter **??**, commercial batteries are readily available and well-specified to supply power for long periods (Rabault et al., 2017). However, the system must conserve energy. Otherwise, this could result in low survival rates (Kohout et al., 2015). Additionally, batteries in sub-zero temperatures have a significantly reduced capacity of up to 50% (Doble et al., 2017).

Therefore, the software needs to contain power monitoring capabilities. A sensor should monitor the current and power usage of the device and provide feedback to the system. The device software should be optimized to conserve power which means turning off sensors that are not in use and entering low power mode during periods of inactivity. Finally, the software needs to handle power events that could disrupt the functionality of the buoy such as brownouts and power resets. The software should be able to recognize when the power is too low to operate and respond accordingly.

3.2.4 Analysis of UR004

System must be capable of measuring ice floe dynamics and environmental conditions surrounding sea ice formation.

As discussed in Chapter 2.1, in situ, remote sensing devices have been deployed in the Southern Ocean with specific measurement objectives. Table 2.4 shows that the following measurements were common to one or more devices:

- Ice drift
- Collisions between ice floes
- Waves in ice
- Ambient temperature
- Atmospheric pressure

Meteorological sensing requirements

Temporal resolutions and measurement standards need to be taken in accordance with the World Meteorological Organisation to ensure effective communication and standardisation of the data sets (World Meteorological Organisation, 2010). For environmental data and wave spectra, the data are provided in Table 3.2 below:

Table 3.2: Comparison of standard measurements for meteorological data including temporal resolution, measurement unit and accuracy from: (World Meteorological Organisation, 2010)

Variable Name	**Resolution**	**Accuracy**
Temperature	1 hour	± 0.5 K
Pressure	1 hour	$\pm$ 0.5 HPa
Wind Speed	1 hour	± 2 ms^{-1}

Meteorological data should be sampled from a height of 1 to 40 m (World Meteorological Organisation, 2010). Therefore, all meteorological sensors should be mounted 1 m above the ground to meet these standards. Additionally, the software should be capable of retrieving data from a temperature and pressure sensor. The software should also contain error checking to ensure robust sampling and reliable data from the sensors.

Ice drift sensing requirements

Kohout et al. (2015), Metocean (2016), and Trident Sensors (2021) and Alberello et al. (2020) show that ice drift measurements can be taken using a GNSS tracker can be used to monitor by recording the global coordinates against an accurate time reference. Alberello et al. (2019) show that temporal resolutions affect the behaviour of drift data. Devices that went into low power mode during deployment ((Alberello et al., 2019; Vichi et al., 2019)) had decreased sampling rates which failed to capture ice drift oscillations. Alberello et al. (2020) further show that a temporal resolution of 3 hours is required to capture ice drift oscillations. Additionally, the GPS reading can be affected by the number of satellites picked up by the receiver (dependent on the receiver antenna gain) (Spilker Jr et al., 1996), the spread of satellites and the angle of elevation above the horizon. A characteristic of this error is called the dilution of precision (DOP). This value details the positional or temporal measurement inaccuracy. Moreover, the software needs to accommodate a GPS module and interface with it through a suitable communication port. The software needs to sample the GPS at a frequency of once every 3 hours or less. Finally, the software should configure the GPS module to transmit diagnostic information, positional error and temporal error information in addition to time and date information.

Waves in ice sensing requirements

Wave in ice measurements play a critical role in understanding the formation of sea ice in the marginal ice zone (Alberello et al., 2019). Low frequency, high energy waves propagate through the area and displace the ice floes (Womack, 2020). Current devices such as those developed by (Kohout et al., 2015; Rabault et al., 2017; Thomson, 2012) utilise either a statistical (Kuik et al., 1988) or spectral (Earle, 1996; Welch, 1967) approach which allows for measurements of waves independent of the dynamics of the ice floe. These methods require roll, heave, pitch and vertical acceleration measurements for 1000 s at sample rates above 0.5 Hz, which corresponds to the upper band of ocean waves (Earle, 1996). The software should be capable of interfacing with an IMU and should ensure that data is sampled at a fixed sample rate for the required period. The software should also store the data in an area with sufficient space. Finally, the software should contain error checking algorithms to ensure robust communication with this device.

3.2.5 Analysis of UR005

System must be user-friendly and easy to deploy

Table 2.5 shows the weight of each system. Notably, the lightest device being the Trident buoy at 0.42 kg and the heaviest being the buoys by Doble et al. (2017). The weight of the device significantly affects the deployment protocol. Heavy devices will require a large team to deploy the device and specialised courier methods to transport it such as those described in Doble et al. (2017). Devices that weighed 4.5 kg to 30 kg were light enough to be carried by one person and deployed much faster.

The deployment is also affected by the set up of the device. The SIMB Buoy, while being relative light, requires a team to assemble the components on the ice and drill a hole to place it in (Planck et al., 2019). Kennicutt et al. (2016) shows that certain polar regions are too dangerous for manned missions, which can limit the deployment location and time frame the crew can spend setting up the buoy. However, systems that are relatively easy to deploy (Trident, WIIOS, SWIFT) allow for sensing near dangerous environments such as the ice edge of the marginal ice zone. These devices are preassembled and set up leading to a "drop and go" style deployment from ship cranes (Alberello et al., 2019; Vichi et al., 2019) or boats (Kohout et al., 2015; Rabault et al., 2019). The software should be configured to begin execution as soon as the device is operational. Software settings and parameters should be loaded into permanent storage and the sensors should be calibrated before being sent on the expeditions.

3.2.6 Analysis of UR006

System must be cost effective

Guimarães et al. (2018), Planck et al. (2019), and Rabault et al. (2019) consider cost to be a significant constraint in designing a system. Additionally, some devices such as SIMB buoy, gradually factored in price after two iterations (Planck et al., 2019). This shows that optimising device performance for cost is critical for increasing the affordability and availability of devices. An affordable system Table 2.5 showed a comparison of reported costs and wughts for each system where applicable.

from Table 2.5 we can see from the cost breakdown that Rabault et al. (2019) succeeded in creating a low cost buoy through the use of open source hardware and off-the-shelf components resulting in this device having the lowest reported price out of all the system. The next cheapest device is the Trident buoy which is only R300.00 more expensive than the WIIB. However, this device contains fewer sensors and is only capable sea ice drift and temperature measurements. On average, commercial systems (UptempO, Polar ISVP, Trident) proved to be significantly more expensive than research devices with similar attributes. However, due to the absence of prices for SWIFT, WIIOS and Trident it is difficult to draw conclusions from this comparison. Furthermore, commercial systems had design capabilities to design and print custom circuit boards and chip sets while research systems (SWIFT, WIIB, WIIOS) did not have such capabilities. Therefore, the developers optimised for procurement time by using off the shelf components (Kohout et al., 2015; Rabault et al., 2019). A novel sensing device that is cost optimized should result in an overall cost cheaper than the devices in table 2.5 with comparable performance, this will also allow for quicker and cheaper device procurement allowing for more devices to be produced for deployment thereby allowing for a larger spatial area in the marginal ice zone to be covered.

3.2.7 Analysis of UR007

System must be able to store and process data in an organised manner

The proposed system will require multiple subsystems to satisfy the user requirement UR004. These subsystems will generate large volumes of data that needs to be stored and organised efficiently. As shown in the discussions for user requirements UR001 to UR005, the system will require multiple sensors and modules. Each module has different operational and communication requirements. Therefore, a suitable processor needs to be selected to provide sufficient ports to interface with each sensor. This processor should accommodate sufficiently high volumes of data with a wide enough byte size to accept sensor data without calculation errors. The software will need to meet the requirements of each sensor and sequence these functions into a routine. This can be achieved by developing sensor libraries for each device. Included in these libraries will be initialisation routines, peripheral communication drivers and sensor sampling routines to meet the requirements for each sensor. Furthermore, as shown in the discussion above, each sensing activity is time-critical. This places a strict timing requirement on the device to ensure the integrity of the data set on a temporal scale. Therefore, an accurate timing reference is required in the form of a real-time clock (RTC).

Additionally, Each sensor has a different data rate requirement. Some sensors will need to stream large volumes of data of an unknown length. To deal with this, efficient data acquisition techniques need to be implemented by the software to accommodate these volumes. Such techniques include setting up direct memory access (DMA) channel in a circular buffer to stream data to a memory location with an input capture timer on slave reset mode to close the channel when the data stream is completed.

Finally, long periods of inactivity between measurements can result in wasted power. The discussion of user requirement UR003 showed that the software should turn the device off or into low power mode during these periods. If the data is in the processor memory when the device is off, it could get lost. Therefore, a permanent storage device is required to store data during these periods of inactivity. The software should include functions to read from the storage space and write to it efficiently. Additional error checks should be written to ensure the storage device is online, operational and the data has not been corrupted.

Finally, the aforementioned hardware and software modules need to be verified with a suite of acceptance tests to ensure that all the user requirements have been met.

3.3 Functional requirements

Analysis of the aforementioned user requirements resulted in the procurement of a set of functional requirements that dictate how the buoy will function.

3.3.1 Operational requirements

Table 3.3: Requirements addressing the mechanical needs for the system during operation.

Requirement ID	Description	User requirements addressed
FR001	The System shall have a protective enclosure against precipitation and frost.	UR001 UR005
FR002	The enclosure shall be constructed from strong, corrosion resistant materials with strong thermal characteristics.	UR001 UR005
FR003	The device will protect electronics from internal humidity.	UR001
FR004	The electronics will be elevated above the ground by 1 m.	UR001 UR005
FR005	All subsystems shall be rated for extreme temperatures.	UR001 UR003

3.3.2 Electronic requirements

Table 3.4: Requirements addressing the electronic needs for the system including the modules, components and sensors that satisfy the user requirements.

Requirement ID	Description	User requirements addressed
FR006	System will transmit data via Iridium satellite network.	UR002
FR007	Device shall be battery powered.	UR001 UR003
FR008	System shall measure ice drift using a global positioning system (GPS).	UR004
FR009	Device shall measure ambient temperature.	UR004
FR010	Device shall measure atmospheric pressure	UR004
FR011	Device shall contain an inertial measurement unit (IMU) to record acceleration (3-axes) and rotation (3-axes) of an ice floe.	UR004

3.3.3 Software requirements

Table 3.5: Software functional requirements for the system addressing the system function, performance, operation and control during the lifetime of the device.

Requirement ID	Description	User requirements addressed
FR012	Device to contain sufficient memory for data storage.	UR006 UR007
FR013	Device to contain a processing unit to control sensors and process data.	UR006 UR007
FR014	Device to be optimised for low-power consumption and power event handling.	UR003 UR006 UR007

3.3.4 Other requirements

Table 3.6: Other system requirements being addressed.

Requirement ID	Description	User requirements addressed
FR015	Device shall be calibrated prior to shipping and delivered in a state where it can be deployed at a moment's notice	UR005
FR016	The Device will cost less than currently available systems.	UR006

3.4 System overview

To meet the functional requirements, the overall system was designed using a top down approach. The requirements highlighted in Tables 3.3 to 3.4 will be used to identify key subsystems to achieve the required functionality.

Table 3.7: Table showing the subsystems that are critical to the functionality of the buoy and the level of importance indicated by rank

Name	Rank
Firmware	1
Power system	2
Communication module	3
Processor	4
Sensors	5
Permanent storage	6
Mechanical features	7

The firmware is the most critical subsystem in the device and ranks the highest in terms of priority. The firmware is crucial for the operation of the device and to control all the modules. The next most critical component is the power system. Any failures in the power system will cause the device to stop functioning. All device components need to be rated for subzero operation to ensure robust operation. A voltage regulator will be included to ensure a constant voltage. Finally, a power sensor will be included to monitor the batteries and warn the system when the batteries are almost depleted.

After the power system is the communication subsystem as Iridium will be used to transmit the data obtained by the system. Should this device fail, the device will be unable to transmit data unless it is retrieved. Satellite communication for Iridium is performed using a satellite mode while GPS communication is performed using a GPS receiver. They require, clear, unobstructed views of the satellites which can be achieved with high-gain antennas. These devices need to mounted as close to the sky as possible.

The sensors are the primary interface between the system and the environment. The electronics need to be as close to the exterior of the system as possible to measure ambient temperature and pressure. The IMU can be mounted anywhere inside the buoy however, the device needs to be calibrated for its position on the buoy as well as its orientation inside.

The sensors will interface with a central processing system which will control the sensors and sample data from them. Data coming from the sensor will be processed and stored in packets in a permanent memory storage system. Finally, a metal stand will be created to anchor the device to an ice floe and suspend the electronics well above the sea ice surface to prevent it from being covered in snow. The electronics will be placed in a thermal-resistant and waterproof enclosure to protect the system with desiccant placed inside to prevent moisture from interfering with the device. A block diagram of the proposed system is shown in the figure below.

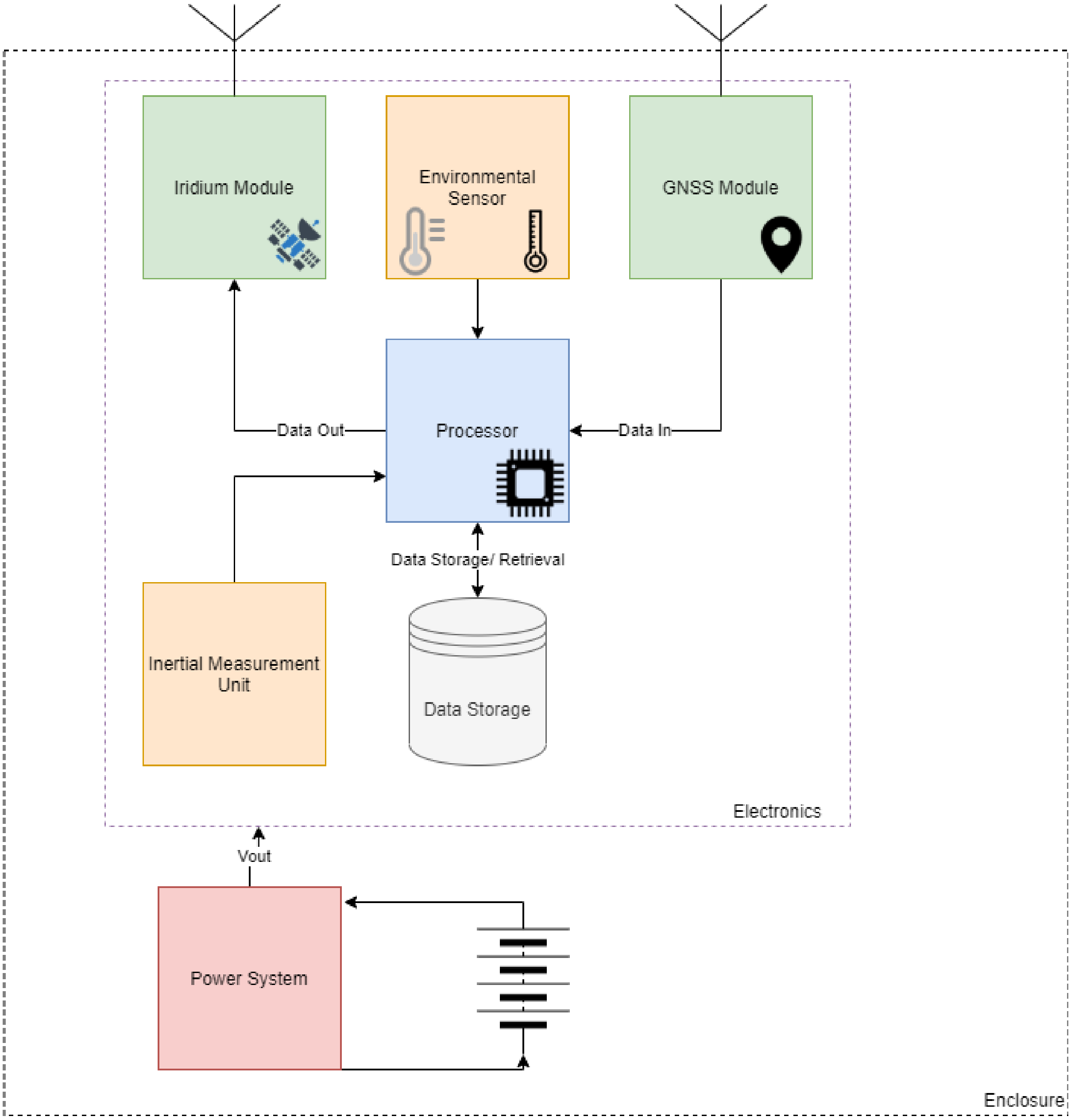

Figure 3.1: Block diagram of the proposed autonomous system showing subsystem arrangement, data flow and interfaces with the environment.

These subsystems can be further broken down into components requirements as shown in the figure below

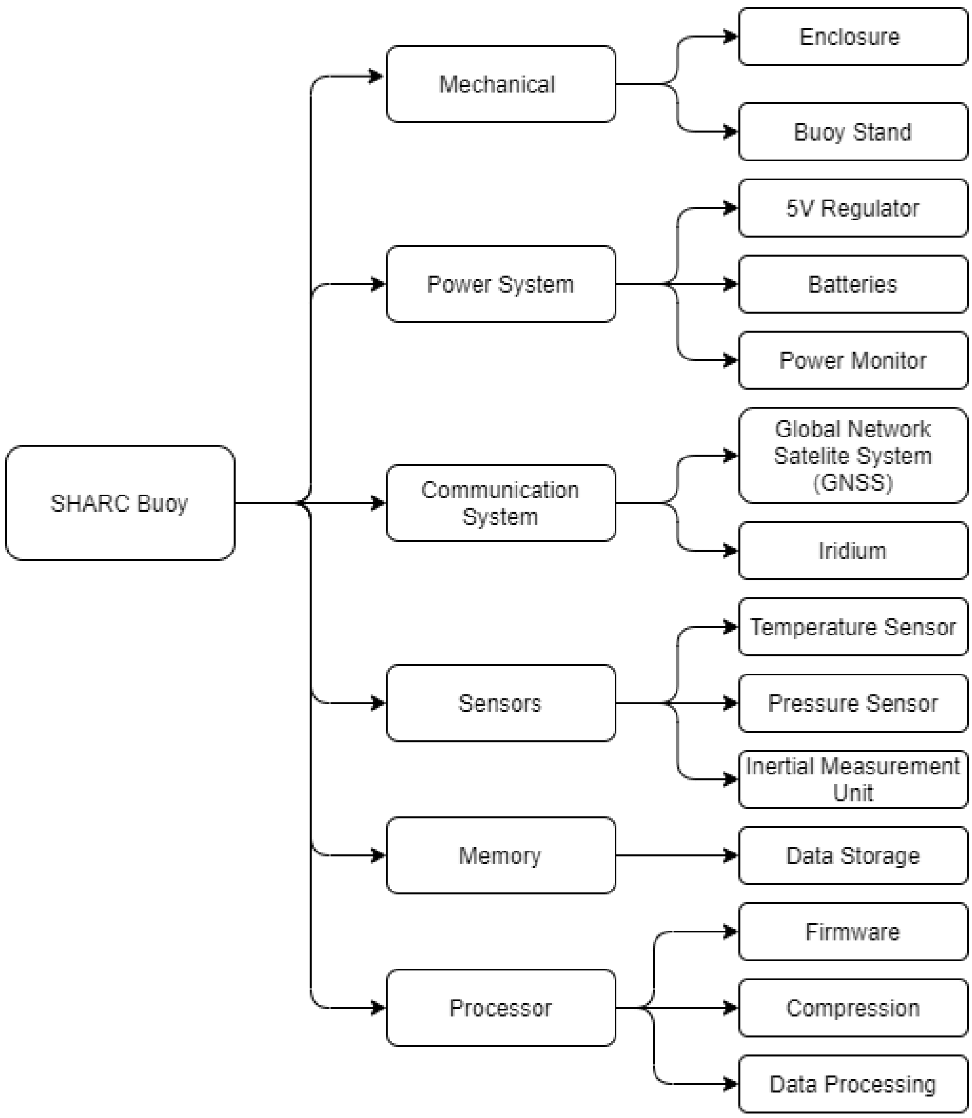

Figure 3.2: Breakdown of subsystems from table 3.7 into usable components.

3.4.1 Technical specifications

These technical specifications will be used to determine what hardware is required to construct the subsystems as showing in Figure 3.1 above.

Table 3.8: Technical specifications for the overall system

Specification ID	**Description**	**Functional requirement addressed**
SP001	Enclosure built using thermal resistant plastic.	FR001 FR002
SP002	Electronics to be mounted on a 1.5 m stand constructed from non-corrosive metal.	FR002 FR003 FR004
SP003	System to include desiccant packets inside the enclosure.	FR003
SP004	Device to have a temperature operating range of $-40°$ C to $20°$ C with $1°$ C uncertainty.	FR009
SP005	Subsystems to be rated for 3.3 **V to** 5 V power.	FR008
SP006	Device shall survive for 1 month on a single set of cells	FR007
SP007	The device should cost less than R10,000	FR016
SP008	System will contain flash chips for permanent storage.	FR012
SP009	System will use the STMicroelectronics STM32 series of microcontroller.	FR013
SP010	The system shall be supplied by a regulated 5 V supply.	FR014
SP011	The low power threshold occurs for voltages < 5 V	FR014
SP012	Maximum current operations: 500 mA maximum start-up current. 100 mA maximum active current. 10 mA sleep current.	FR0014
SP013	Device to be powered off or placed in sleep mode when inactive.	FR014

3.4.2 Acceptance test protocols

In this section, the acceptance testing protocols for hardware and software modules is provided. These tests are designed to ensure that the devices meet the functional requirements outlined in table 3.3 to 3.6. A full description of the acceptance test protocols can be found in Appendix B.2. The goal of the acceptance criteria of each test as well as the the targeted module is given in table x below.

Table 3.9: A summary of acceptance test protocols from Appendix B.2 showing the target and purpose of the test.

Acceptance test	Target	Purpose
AT001	Sensor modules.	Ensure module is online and functional
AT002	All hardware modules.	Test for faults and errors.
AT003	Device components.	Ensure selected components are rated for this application.
AT004	Sensor peripheral libraries.	Verify software correctly interfaces with subsystem modules.
AT005	Full system.	Ensuring an accelerated functional cycle meets the timing and sensing requirements.
AT006	Sensor modules.	Calibrate the sensors against a known reference.
AT007	Power subsystem.	Verify the power system meets the user requirements.
AT008	Full system.	Ensure the device can operate in low temperatures.
AT009	Full system.	Ensure device functions in a remote environment.

3.5 Conclusion

To summarise, this chapter outlines the design procedure for identifying critical subsystems and technical specifications to meet the user requirements. This will provide the basis for component and module selection which will be discussed in the next chapter.

Chapter 4

Platform design

In this chapter, the hardware design processes are outlined based on the user requirements and technical specifications given in Chapter 3. This chapter begins with a description of the mechanical features showing how the design accommodates the electronic subsystems while meeting the functional requirements outlined in Table 3.3. This chapter then shows the electronic components selected for each subsystem and how they affect the overall system. Finally, this chapter will conclude with the final design considerations for the buoy.

Son and Vorajee in 2018 performed initial concept work for the buoy, which strongly influenced the current design choices for this device. Furthermore, MacHutchon designed the original buoy with modifications by Verrinder to accommodate the buoy. Verrinder designed the physical enclosure and electronic hardware subsystems for the first (V1) and second (V2) versions of the buoy with further design contributions from Jacobson (V1, V2), Cloete (V1) and Pead (V2).

4.1 Mechanical features

The mechanical design for the system falls outside the scope of this project. However, it forms an integral part in protecting the electronics against sea ice dynamics, strong wave activity and freezing. This subsystem consists of two parts:

1. Buoy stand
2. Enclosure

4.1.1 Buoy Stand

The principle goal of the stand is to anchor the device to the ice floe and protect it from the harsh environment. A buoy stand was designed by K MacHutchon with modification from R. Verrinder and was constructed by the University of Cape Town's Mechanical

Engineering Workshop to satisfy this requirement. The stand is shown in Figure 4.1 and is 1.2 m tall with a width of 0.71 m. The stand has a cylindrical cradle at the top where the device will be placed. A screw hole in the side of the cradle allows the buoy to be fastened to the stand to prevent it from falling out during deployment. The base of the stand is pyramid shaped with metal spikes to anchor the system to an ice floe. Due to the height of the stand, the system may be susceptible to tipping. This has been overcome by constructing the base to be heavier than the top thereby lowering the centre of gravity. The stand was originally designed for the Trident buoys. However, this design has been modified by increasing the radius of the housing.

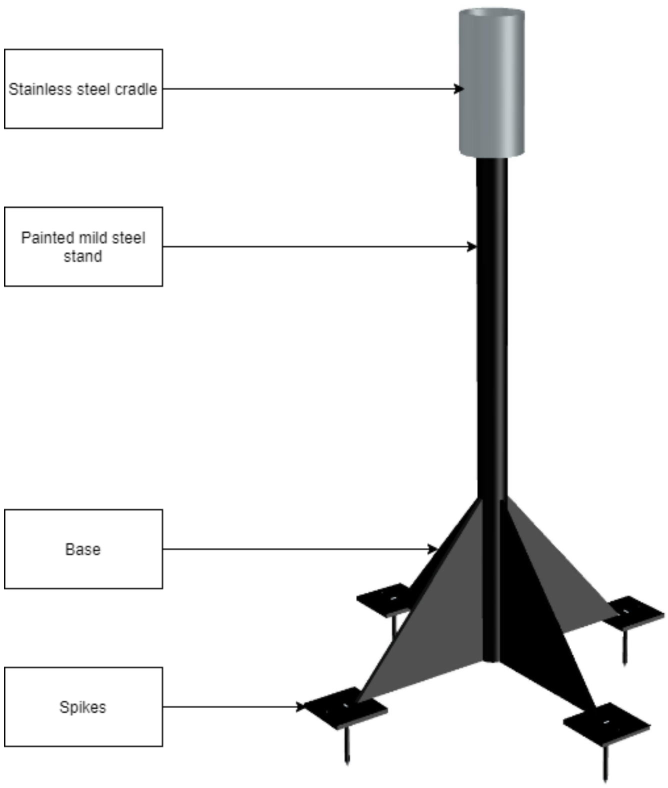

Figure 4.1: Diagram of the buoy stand for the SHARC buoy. The stand consists of stainless steel and painted mild steel to withstand the climate of the Southern Ocean and stop the stand from rusting. A cradle at the top of the stand houses the buoy and secures it to the stand via a screw. The buoy stand elevates the electronics 1m above the ice to overcome the effects of snow growth and flooding. Finally, spikes at the bottom of the base will secure the stand to the ice floe. Drawn by R. Verrinder.

4.1.2 Enclosure

The second part of the mechanical subsystem is the physical buoy enclosure, which was designed by R. Verrinder. The greatest challenge for designing this system was selecting a material that was both lightweight and low-temperature resistant. A decision was made to use High-Density Polyethylene (HDPE) which can survive temperatures up to $-120°$ C before becoming too brittle (Studenovská et al., 2003). The enclosure was designed to fit the housing on the buoy stand while providing ample room for the antennas of the various communication modules. It was split into 3 parts: A top enclosure, a bottom enclosure and a connector block. A schematic of the enclosure is shown in figure 4.2

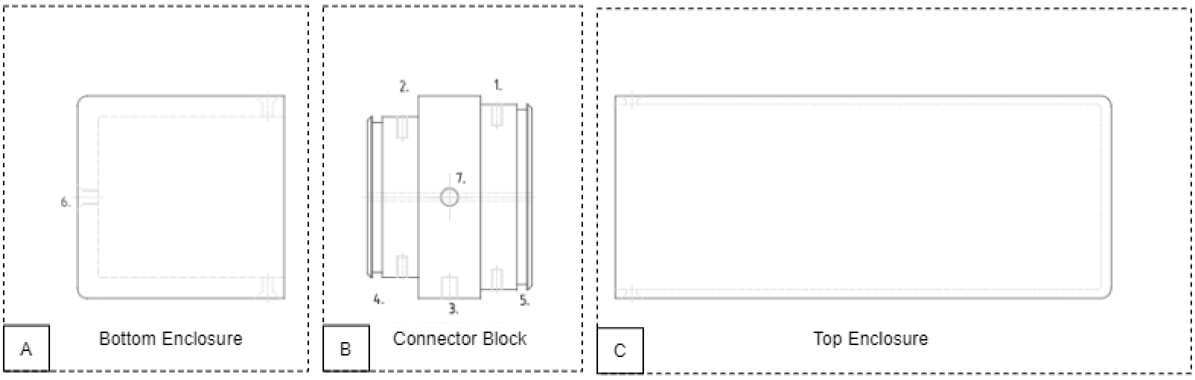

Figure 4.2: 2-D exploded view of the buoy enclosure showing (A) the bottom enclosure for the power module, (B) the connector block which also acts as a base for the electronics and (C) the top enclosure which covers the electronics. Drawn by R. Verrinder.

Table 4.1: Primary measurements of the buoy enclosure taken from the schematic in Appendex B.3

Component	Dimension	Size [mm]
Top Enclosure	Height	240
	Outer diameter	98
	Wall thickness	4
	Base thickness	5
Bottom enclosure	Height	100
	Outer diameter	98
	Wall and base thickness	10
Connector Block	Height	80
	Outer diameter	98
	Top inner diameter	89.94
	Bottom inner diameter	77.85
	O-ring thickness	2.6

This design allows for easy access to the electronics as well as separation between the various subsystems. The connector block acts as a connection point for the electronics in version 1 of the buoy. This point of contact was a three-dimensional printed connector for a vertically mounted printed circuit board (PCB). In version 2 of the buoy, this was replaced by a row of screw holes around the connector block to connect a horizontal stack of customised PCBs. This was found to greatly improve the robustness of the system and prevented components from breaking during transport and deployment. The communication modules, microcontroller and sensors were mounted in the top enclosure while the batteries and power system were placed in the bottom enclosure. The power system was connected to the top enclosure through a drill hole in the connector block. The system was waterproofed by placing two o-rings on either side of the connector block. The top and bottom enclosure are fastened to the connector block using a a flat head counter-sunk hex screw. Finally a drill hole in the connector block allowed the system to be secured to the buoy stand preventing it from falling out during deployment.

4.2 Electronics

The electronics for the system refer to the communication subsystems, power electronics, sensors and processors. Due to project time constraints, the approach to developing the platform was to select off-the-shelf components that satisfied the subsystem specifications shown in Table 3.8. Further consideration was given to components that were low power (SP011, SP012) and cost effective (SP013). Additionally, devices with intelligent operations were selected as this would allow us to effectively control the current consumption and operations of the device. These consisted of components with programmable settings such as digital sensors and modems. The following section gives an overview of the selection consideration for each subsystem.

4.2.1 GPS

A u-blox NEO-7M[1] GNSS reciever was initially selected during the 2018 design concept phase as it was easy to procure and has a small form factor. The positioning module was designed around a Waveshare[2] development board which significantly decreases the development time. The board comes with an active patch antenna which has a gain of about 30 dB (Waveshare, 2016). In addition, the component is low power with a relatively fast acquisition time and accuracy. The device also can be configured to output diagnostic information such as dilation of procession with the associated measurement which can provide a greater understanding of satelite connectivity in the region. However, this product has been depreciated by the time the latest buoy was developed. To overcome this, we opted for the u-blox NEO-M9N[3] module which had improved performance at a higher cost. Table 4.2 below shows a comparison of the two modules and their key performance parameters.

[1] *NEO-7 U-Blox 7 GNSS modules data sheet.* 2014.
[2] Waveshare, 2016.
[3] *u-blox M9N standard precision module Datasheet*, 2020.

Table 4.2: Comparison of key parameters between the initial u-blox NEO-7M GNSS module and the updated u-blox NEO-N9M module.

Specification	Neo-7M	Neo-M9N
Positional accuracy [m]	2.5	2.0
Communication type	UART I2C SPI	UART I2C SPI
Cold-start time [s]	30	26
Supply voltage [V]	1.65 to 3.6	2.7 to 3.6
Active current draw [mA]	32	42
Price	R269 [4]	R1,195[5]

Table 4.2 shows the u-blox NEO-M9N offers improved performance over the u-blox NEO-7M at a higher cost and higher power consumption. This module comes on a Sparkfun GPS Breakout - NEO-M9N U.FL (Qwiic) board which optionally comes with an integrated chip antenna. The chip antenna however has a very small gain making it unsuitable to be used for this application. Therefore, an additional antenna was bought.

4.2.2 Iridium

The Iridium modem is critical for ensuring data can be transmitted from remote locations. When selecting a modem, key considerations were given to the physical size, Bandwidth as well as coverage. In addition, we require a module that is low powered and cost effective. For this reason, we have selected the Rock block 9603 modem which has the following key specifications. This is a module that contains an Iridium 9603 modem on a specially -designed power board. The device communicates via UART with the option for flow control. The module contains a 10-pin picoblade. The module contains 4 communications pins, 1 digital input pin and 2 digital output pins for interfacing with. Power is supplied either through a 5V pin or 3.3V pin in addition to the ground pin. A brief description of the pin out is given in the table below:

[1]from Digikey https://www.digikey.co.za/ ordered on 09/2020
[5]from Microrobotics https://www.robotics.org.za/ ordered on 19/12/2018

Table 4.3: Pinout for the Rockblock 9603 Iridium Modem

Pin Number:	Label	Pin Description
1	RXD	UART Output Pin
2	CTS	Flow Control Clear To Send
3	RTS	Flow Control Request To Send
4	NetAv	Network Available
5	RI	Ring Inidcator
6	TXD	UART Input Pin
7	OnOff	Sleep Control
8	5V	5V max supply pin
9	Li-Ion	3.7V max supply pin
10	GND	Ground

The device communicates via UART through the RXD and TXD pins. The CTS and RTS pins are optional if flow control is required. The OnOff pin can be used to put the device to sleep which significantly improves power performances. Finally, The NetAv and Ring Indicator are notification pins that can be used to indicate whether there is sufficient signal to transmit as well as to notify when a message is waiting to be downloaded respectively.

Finally, the key characteristics for the device are shown in the table below:

Table 4.4: Table showing key parameters and performance characteristics taken from the datasheet

Mechanical Features:

Antenna:	Patch or External SMA
Temperature Rating:	-40ºC to +85ºC
Dimensions	45.0 × 45.0 × 15.0 mm
Cost:	R2,850.56

Power Characteristics:

Supply Voltage	5v or 3.7v Li-Ion
Start-Up Current	450mA
Active Current	100mA
Sleep Current	200uA

Communication:

Baudrate	19200 b/s
Data bits	8
Stop bits	1
Parity	none
Max Upload size	340 bytes
Max Download Size	270 bytes

4.2.3 Sensors

2 versions of the buoy were developed from 2019 - 2020 with different sensing capabilities. The first version consisted of a DS18B20 Temperature sensor. This was a low cost, small form factor device that interfaced over One-wire. In version two, this was dropped in favour of the Bosh Sensortech BMP280 sensor. The BMP featured improved sensing capabilities, temperature compensation as well as a programmable interface. In addition, the sensor contains both an ambient temperature sensor as well as a pressure sensor. A comparison of each device is given in the table below

Table 4.5: Comparison of performance between the BMP280 and DS18B20 environmental sensors.

	BMP280	**DS18B20**
Temperature Range	$-40°C$ to $85°C$	$-55°C$ to $125°C$
Accuracy	$1°C$ for $T < 0°C$	$1°C$ for $T < 0°C$
Pressure Range	N/A	300 to 1100 HPa
Pressure Accuracy	N/A	1.7 HPa for $T < 0°$
Price	R87,84	R85.17

The BMP 280 is a chip that can be ordered standalone or comes on a I2c/SPI ready breakout board. The device on a breakout board is cheaper than than DS18B20 and can measure both temperature and Pressure whereas the DS18B20 can only measure temperature. The Power characteristics of each device are given in the table below

Table 4.6: Comparison between supply voltage and current draw of the BMP280 and DS18B20

	BMP280	**DS18B20**
Supply Voltage	3.0V - 5.5V	1.71V - 3.6V
Sleep Current	$0.75\mu A$	$0.3\mu A$
Active Current	$1500\mu A$	$4.2\mu A$

The BMP280 was chosen for its comparable performance and accuracy. In addition, the BMP280 features more sensing capabilities and is more power efficient and cost effective than the DS18B20 making it suitable for this application.

Finally, a digital sensor for power monitoring was selected to provide constant feedback on the status of the power system. This will be used to monitor the battery voltage as well as the current draw to make sure that the system does not deplete the energy reserves to quickly. To achieve this a INA219A IC was selected and mounted on a custom PCB with a shunt resistor of known resistance. The device has a high reported accuracy of 1% over a full temperature range and is fully programmable. The device communicates via I2C with 16-bit registers storing ADC values for Current (mA),Voltage (V) as well as power (mW). The device is extremely low power with a high voltage measurement range and on-board calibration features. Some key performance parameters are shown in the table below:

Table 4.7: Performance specifications for the INA219 current monitor chip.

Operating Temperature:	$-40°C$ to $125°C$
V_{shunt} **range:**	$40mV$ to $320mV$
V_{bus} **rage:**	$0V - 16V$ or $0V - 32V$
ADC Resolution:	12-bits
Measurement Error:	$\pm 1\%$
Price:	R17.77[6]
Power Characteristics	
Supply Voltage:	$3.3V$ to $5V$
Quiescent Current:	$0.7mA$ to $1mA$
Standby Current:	$6\mu A$ to $15\mu A$

4.2.4 Inertial Measurement Unit

The MPU6050 is a 6-axis IMU that measures the acceleration and rotational velocity of 3 axes respectively.This component has a small form factor, low power and is fully programmable allowing the device to operate in different modes thereby optimising the data flow to and from the device. While the device does not contain a magnetometer, this is not an issue since the region suffers greatly from magnetic distortion (Kohout et al., 2015) thereby rendering all readings to be unreliable. In addition, The acceleration of waves can be defined by the stoke supper limit (Kohout et al., 2015) as 0.5g for a non breaking wave. The device has a programmable full scale range for both the accelerometer and gyroscope. IT contains an IIR filter and on-board self testing for added robustness and data integrity thereby making it the ideal device for this application. The key parameters for the device are shown in the table below:

[6] source: https://www.digikey.co.za/

Table 4.8: Performance Characteristics of the MPU6050 6-axis IMU

Accelerometer:	
Full Scale Resolution:	$\pm 2g$ to $\pm 8g$
Sensitivity:	$61.17\mu g/LSB^{-1}$ to $488.281\mu g/LSB^{-1}$
Sample Rate:	4Hz - 1000Hz
Noise Performance:	$400\mu g/\sqrt{Hz}$
Gyroscope:	
Full Scale Resolution:	$\pm 250°/s$ to $\pm 2000°/s$
Sensitivity:	$7.63(\mu°/s)/LSB^{-1}$ to $60.98(\mu°/s)/LSB^{-1}$
Sample Rate:	4Hz - 8000Hz
Noise Performance:	$0.005(\mu°/s)/\sqrt{Hz}$
Device Characteristics:	
Temperature Range:	$40°C$ to $85°C$
Low Pass Filter Range:	5Hz to 256Hz
Supply Voltage:	2.375V to 3.46V
Active Current:	3.9mA (Max)
Low Power Current:	$< 20\mu A$ for $ODR < 5Hz$
Cost:	R40.00 [7]

The device has a high range for both gyroscope and imu with ideal low power performances making it the ideal device. In addition, the device comes prototype ready on the GY-521 development board. The device can be interfaced either using SPI or I2C. For this application, the device was interfaced with using I2C.

4.2.5 Memory

Physical memory is an important feature in the device as it allows for permanent storage of data during the life cycle of buoy. Having the device in various sleep modes may result in lost data if the data is stored in RAM.

Flash Chips were selected as a permanent Solution. An array of 4 AT45DB641E SPI Serial Flash Chips were selected and mounted on a PCB directly interfacing with the system. Each chip can hold up to 64Mbit of data. Data can be read/ written at speeds of up to 85MHz of 15MHz in low power mode. The device is low power with high data retention requiring a supply voltage of 1.7V – 3.6V and draws a maximum of 11mA in Active Read mode thereby making it one of the lowest power consumption components in the system. In addition, the device comes with 2 x 256byte buffers that can store data while a read/ write operation is taking place. Memory is Organized into sectors (2 – 256 Kbs long), blocks (2kB long) and pages (256 bytes) with write, read and erase options at each level. The following table shows key performance characteristics

[7] Source: https://www.communica.co.za/

Table 4.9: Key performance characteristics for the AT45DB641E flash chips.

Operating Temperature:	$-40°$ to $85°$
Storage Capacity:	64 Mbit
Supply Voltage	1.7V -3.6V
Standby Current:	$45\mu A$
Active Current:	$22mA$
Unit Cost:	R 65.307 [8]

4.2.6 Processor

For the processor, a single processing unit was selected to reduce complexity of the system. However, in order to satisfy the requirements for the buoy, a processor must be selected with sufficient peripheral ports to handle communication from all sensors, communication modules and memory banks. In addition, there should be sufficient digital input and output pins to control the sensors and provide feedback The communication peripheral requirements are condensed into the following table:

Table 4.10: Type and number of communication ports in order to facilitate communication with all the external modules.

Peripheral Name:	Qty
UART	2
I2C	2
SPI	2
Digital Pins	11

Additionally, the processor needs to have a high resolution and large memory bank to handle incoming data. For this reason, a 32-bit micro-controller was identified as the ideal component for the processing system. 3 processors were selected from the STM32 range of microcontrollers and prototyped at various phases during the development cycle. The first version of the buoy contained the STM32F407 which is available on a 100-pin development board thereby decreasing the development time and increasing the technology readyness level of the system. This device was found to have more peripherals than required and had a large power requirement. Therefore the device was replaced by the STM32F446-RE which had significantly reduced peripherals and more optimal performance. The final processor selected was the STM32l476RG. Which matched the STM32F446 in pinout and peripheral however it was significantly more optimised for low power operation. The device had significantly more wake up pins with an extremely low power consumption therefore being the optimal choice. In addition, the development board for the STM32l476 has an on-board debugger which can be removed to reduce the physical size of the device. The STM32L4 can also be configured to passively detect a brownout event as well as a low

[8]Source: https://za.rs-online.com/

power event which provides critical feedback regarding the device's performance. Some key performance parameters of the STM32l476 are shown in the table below:

Table 4.11: Performance parameters for the STM32L4 microcontroller.

Electrical Characteristics:

Input Voltage:	$1.71V$ to $3.6V$
Active Current Draw:	$100\mu A/Hz$
Shutdown Mode Current Draw:	$30nA$
Standby Mode Current Draw:	$420nA$
$V_{brownout}$ **Threshold:**	$1.66V$ to $2.90V$

Computational Characteristics:

Processor:	ARM Cortex-M4
MCU Size:	32-bit
Float representation:	Hardware FPU
Flash size:	1MB
RAM Size:	128 KB
Clock Source:	LSE, HSE, LSI, MSI, HSI
System Clock Frequency:	4MHz to 80MHz
Dhrystone Benchmark:	1.25 DMIPS/Hz

Communication Ports:

Total Communication ports:	20
UART Ports	5
I2C Ports	3
SPI Ports	3

The STM32l4 also features seven general purpose timers as well as two advanced timers and two low power timers. In addition, the device has five wake up pins which allow the device to be woken up from deep sleep (shutdown) via an external source. The device is capable of DSP processing using external libraries provided by the manufacturer and a real-time clock thereby making it the ideal component to be a processor for the buoy.

4.2.7 Power Electronics

Based on the aforementioned Hardware selection, the following power requirements are outlined in the table below:

Table 4.12: Current consumption of various components as well as the estimated maximum possible current draw

Device Name	QTY	Supply Voltage	Maximum current Draw
Ublox NEO-M9N	1	3.3V	42mA
Rockblock 9603	1	5V	450mA
BMP280	1	3.3V	0.0042mA
INA219A	1	V_{Bat}	1mA
MPU6050	1	3.3V	3.9mA
AT45DB641E	4	3.3V	88mA
STM32L476RG	1	5V	2.6mA
		total:	587.50mA

From table 4.12 we can expect a maximum current draw of 587.50. The largest consumer of power is the Rock-block 9603 which can draw up to 450mA when charging. Therefore, the power supply needs to be able to supply at-least 500mA during start up. Current can be conserved by placing the devices into sleep mode which further reduces the current consumption from the batteries. Finally, By only turning the components on when required, even less power can be conserved.

Therefore, a regulator is required that is capable of supplying the required current while being able to stand the drastic changes in current consumption. A decision was made to use a 5V low Dropout regulator to supply the 5V components directly i.e. the iridium modem and the micro-controller. The 3.3V components are powered through the on-board 3.3V regulator for the STM32L4 nucleo development board. The Low Dropout regulator is a LP3876 7V LDO capable of supplying up to 3A. The device has a quick response to step changes and an adjustable output voltage thereby making it the ideal device to supply power. The output voltage level can be controlled by selecting capacitors. For this application a $10\mu C$ tantalum capacitor was used as tantalum capacitors have excellent robustness and transient responses especially at low temperatures. Some key characteristics for the device are given in the table below

Table 4.13: Key Performance Characteristics for the LP3876 Low Dropout Regulator

Input Voltage	$2.5V$ to $7.0V$
Voltage Regulation (over current)	0.14%
Dropout Voltage at 3A	0.8V to 1.2V
Quiescent Current at 3A	14mA
Temperature Range	$-40°C$ to $125°C$
Unit Cost	R95.19 [9]

The LDO was placed on a customised PCB with the INA 219 Current sensor as well as an indicator LED to show that the batteries have sufficient charge. The power board was supplied by 3.6V C-cell LiSOCl2 batteries. These batteries have ideal low temperature characteristics as well as a high capacity. 2 cells were placed in series to create a 7.2V

[9]source: https://www.digikey.co.za/

power source which was placed in parallel with another 7.2V array to increase the capacity. The batteries, battery holders and power board are connected to form a single subsystem which was placed in the bottom enclosure and connected to the micro-controller via a 7-pin cable.

4.3 Final Assembly

The final electronics choice and configurations are shown in the figure below:

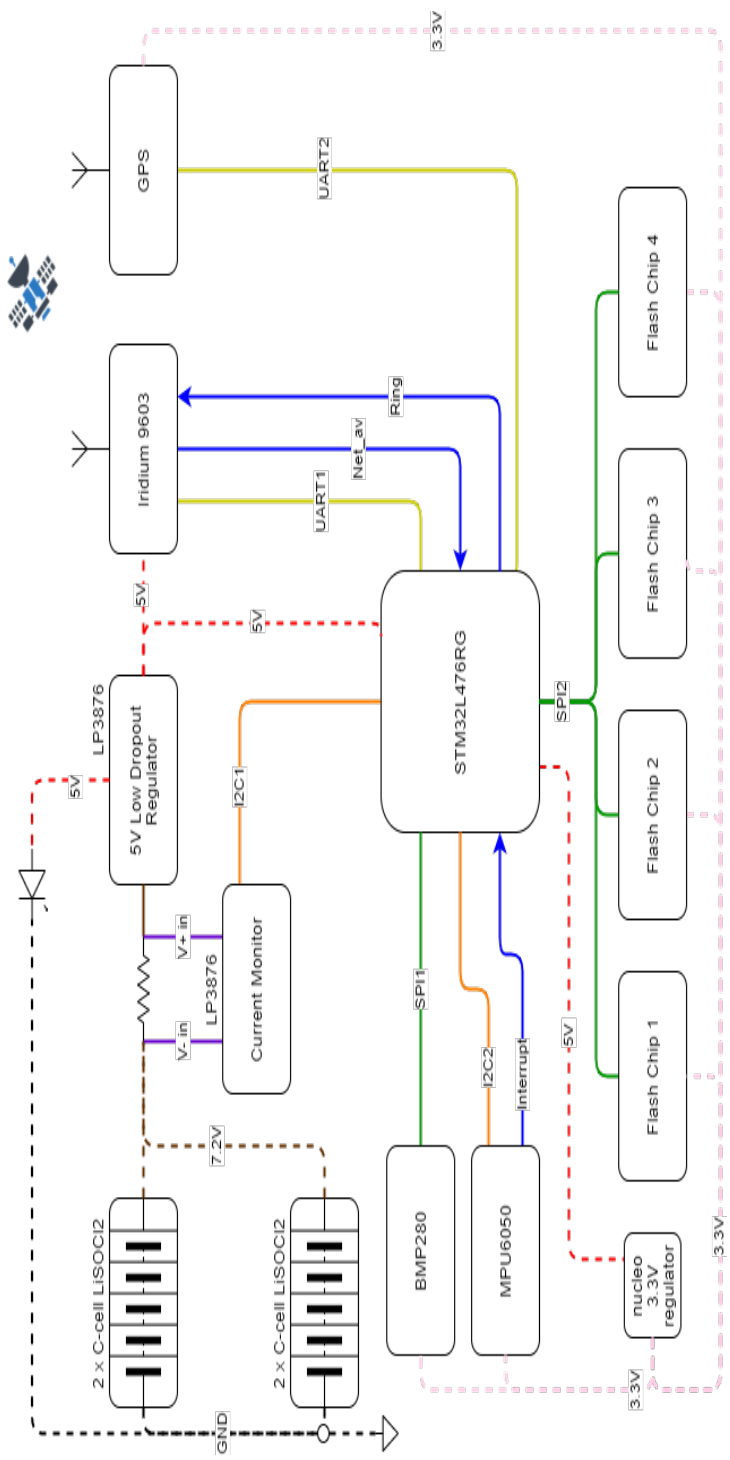

Figure 4.3: Simplified schematic of the final version of SHARC buoy showing power supply (dash), communication (solid) and digital connections (arrows) and configurations

A final costing of the system is provided in the table below:

Table 4.14: Approximate procurement cost for a single SHARC buoy node.

Component Name:	QTY:	Unit Cost	Total:
Buoy Enclosure and Stand	1	R1,206.84	R1,206.84
Ublox Neo-M9N	1	R1,195.45	R1,195.45
Rockblock 9603	1	R3,278.144	R3,278.144
M1621HCT Helical Antenna	1	R1,411.15	R1,411.15
BMP280	1	R46.00	R46.00
INA219A	1	R17.77	R17.77
MPU6050	1	R40.00	R40.00
AT45DB641E	4	R65.307	R261.229
Nucleo-l476RG	1	R215.98	R215.98
Fanso C-cell 9000mAh Battery	4	R101.81	R407.24
BHC-2ND Battery Holder	4	R61.87	R247,48
LP3876 5V regulator	1	R95.19	R95.19
Wiring and Connectors	-	R136.46	R136.46
		Grand Total:	R8,421.13

Customised PCBs were designed to connect the various subsystems together. The device was kept modular by separating PCBs and grouping devices by functionality. A circuit board was created for the Dropout regulator and INA219 current sensor which was affixed to 4 x C-cell battery holders.The battery holders have leads which were were arranged in a 2-series, 2- parallel configuration.

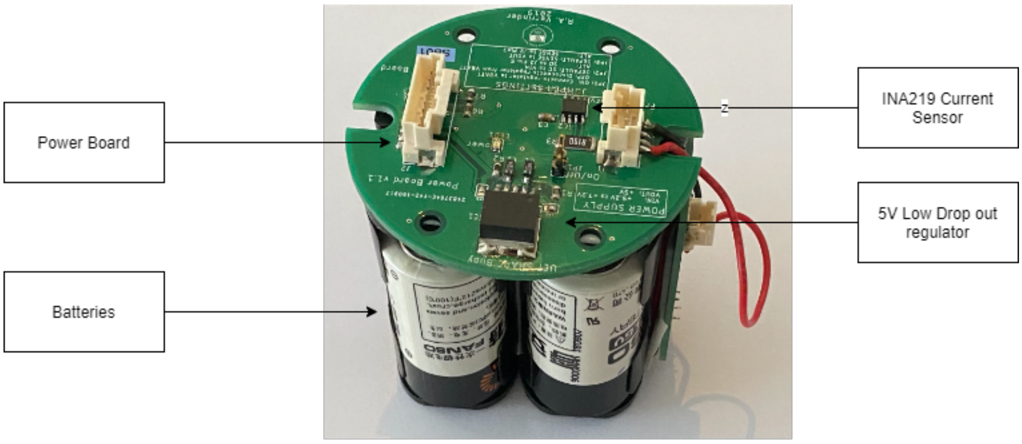

Figure 4.4: Power Module for the SHARC BUOY. A custom PCB with Dropout Regulator and current sensor connected to a battery pack

This module was placed in the bottom enclosure and fastened to the connector block using a hex screw. A customised 7-pin duraclick cable connects the module to the modules in the top enclosure. A main connector board was developed with duraclick connections for each of the aforementioned devices. The board contains 2 2x16 female header rows to fit the morpho connectors of the nucleo-l4 development board. 2 more disc-shaped PCBs were developed. First a communication boards which contains a 4-pin female header to connect the ublox GPS module and 2 brackets to mount the iridium module vertically. A helical antenna connects to an SMA antenna on the Iridium module. Then a sensor board for the IMU and environmental sensor. The boards were connected in a stack configuration and fastened to the connector block using M6 metal Hex Spaces with the communication board being placed at the top for direct line of sight with satellites. The environmental board was secured to the base of the connector block with the BMP280 placed face-down over a hole drilled through the connector block allowing it to interface with the environment.

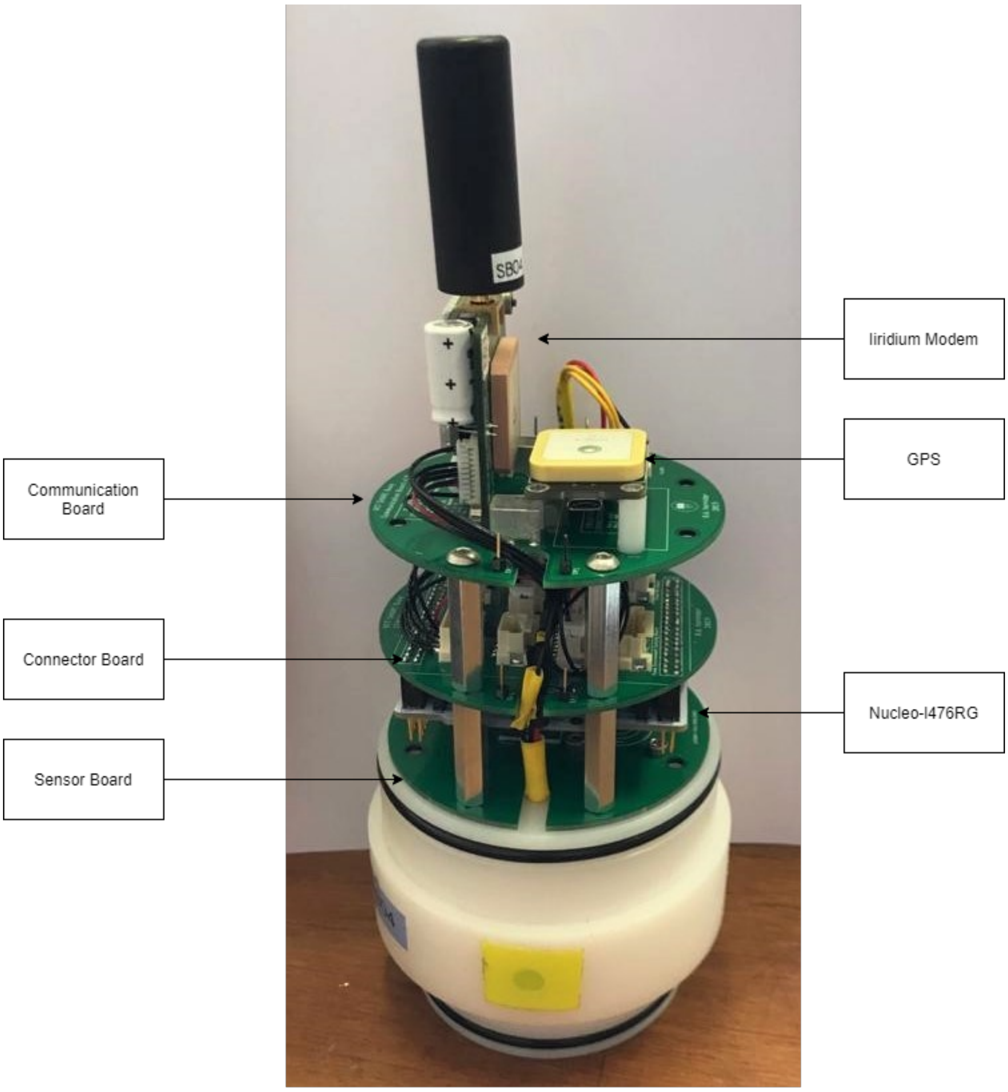

Figure 4.5: Electronic Stack for the top module consisting of connector board, micro-controller board and sensor board attached to the connector block

This configuration greatly increases the robustness of the electronics and can overcome breaking caused by poor handling or improper deployment. The top enclosure is placed over the electronics and fastened to the connector block using Hex screws. Finally, the system is placed in the stand housing and secured using another hex screw.

Figure 4.6: SHARC BUOY fully assembled and in deployment state. Electronics placed in enclosure and fastened to the buoy stand. LEDs on the various components indicate that the device is in working order

Chapter 5

Software Design

This section outlines the design methodology for the SHARC Buoy Software. The software cycle was designed with consideration towards the IEEE software standard 12207.1.

The software structure was kept as compartmentalised as possible to improve the modulator of the firmware. This would allow for fewer changes to be made during the design process allowing for a quick response to hardware changes. The design process was iterative as changes were made over the design cycle to the micro-controller platform as well as the sensors. In addition, some of the required libraries had depreciated and needed to be replaced. This section will focus solely on the firmware design for the overall system as well as the subsystem.

This section begins with an overview of the development environment which discusses the tools, platform and any libraries that were used. Then an overview of the main firmware is given. Each aspect of the system is described in terms of function, configuration parameters as well as location in the overall scope.

5.1 Software Architecture

The STM32 series does not come loaded with any Operating System. Therefore, firmware development had to occur on bare metal. In addition, the firmware had to be tailored to the specific micro-controllers architecture. The Atollic Truestudio IDE allowed for development to take place in C. The program comes packaged with an ARM development tool chain and a C compiler allowing for code to be compiled and flashed onto the board via a USB cable. The manufacturer also provides a set of driver files and initialisation tools. The project was written in C which allowed for higher-level code to implemented while still optimising for size and speed on the device. In addition, C allows for the program to include drivers and resources from the manufacturer.

The Firmware was designed using a top down approach. The overall system was decomposed into 3 distinct layers as shown in the figure below

[0]Software life cycle processes—Life cycle data(C/S2ESC - Software and Systems Engineering Standards Committee, 1998)

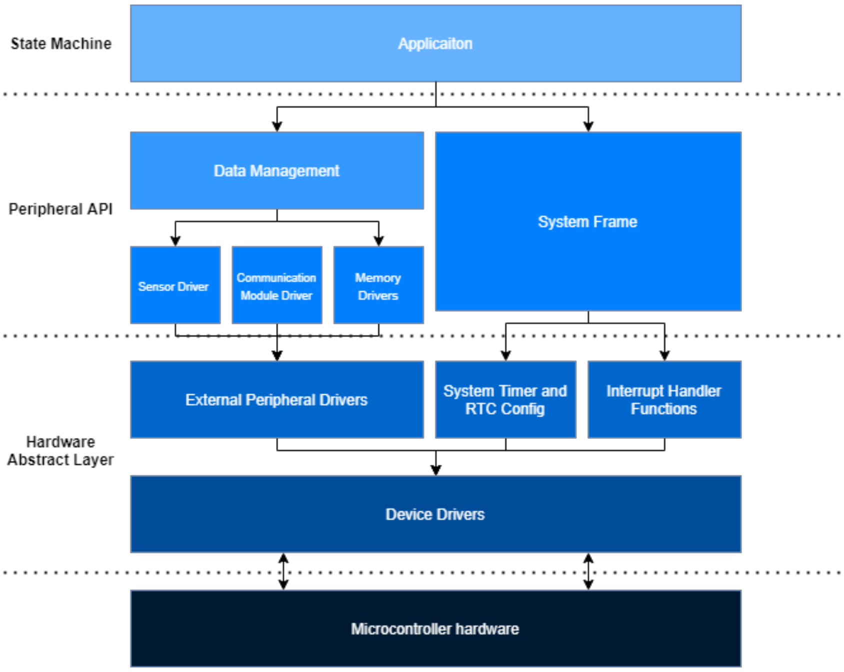

Figure 5.1: Diagram showing the decomposition of the overall firmware into distinct layers and the relationship between each part.

The Hardware Abstract layer consists of the driver files used to initialise and control the hardware of the micro-controller.This layer is platform specific therefore needs to be tailored to the architecture of the micro-controller. The manufacturer provides hardware driver files which were used to form the Hardware abstract Layer.The Standard Peripheral Library (SPL) was used in the first version of the firmware however, the library had depreciated and was replaced with the Hardware Abstract Layer (HAL) libraries. HAL libraries were used to form the foundation of the code as it allows for the code functionality to run independently from the hardware architecture. Should a new micro-controller be required, the HAL library simply needs to replaced. Therefore allowing the firmware to maintain modularity and increase portability. In addition, the HAL Library offers robust error checking and flagging. If a peripheral fails at any point during run time, the libraries provide handlers and flag signalling to handler the error.

Once The HAL Layer was finished, customised driver files were written for each module. These files were written to interface with the sensor through the HAL layer thereby reducing dependencies on the hardware, in addition, these driver files were created to abstract the initialisation and configuration process of each peripheral as well as the hardware routines that occur. In addition, some external modules required the use of more than one peripheral such as timer channels for input capture or GPIO pins for External interrupt detection. Finally, these drivers are critical for managing the flow of data too and from the module. The files contain functions that interpret incoming data bytes and convert them to the relevant data type.

Finally, driver files, configuration files and other libraries are synthesised and sequenced into one main program. This program calls the functions defined in the Driver files. This program provides a frame for the various modules to interact with system. This will be discussed in greater detail in the section below

5.2 Project Structure

The project was set up using CUBEMX for creating peripheral initialization and handling functions. Final code for the project can be found in the folder BUOY_Frame_L4. All the tools, definitions and functions developed for the Buoy frame have been organised into the library files Sharc_Frame.h and Sharc_Frame.c. This allows for the frame to ported over multiple projects allowing for a new firmware version to be developed from scratch instantly. The project code files are organised into the following folders:

1. Drivers
2. src
3. Start Up

The project code files are organised into the following folders: 1. Drivers 2. SRC 3. Start Up The Drivers folder contains the HAL and CMSIS libraries for the device. The SRC Folder contains the main.c file which acts as the entry point for the program to run. The start up file contains assembly code that specifies the vector table, Hard fault/ Reset Handler Entry Points as well as the entry point for the main code. When the file startup_stm32l476xx.s is run, the program enters into the main() function and begins running from there. The SRC folder contains the .h/.c pair Sharc_Frame files which are implemented in the main.c The main() code consists of a set up phase and a loop phase. During the set-up, the functions HAL_Init(); and SystemClock_Config(); are used to reset the peripherals and the systick timer and set the System clock to the correct source and speed. These two functions run in the set-up phase of the code and are called whenever the program re-enters the main function. The next step in the set up phase is to configure the unused GPIO pins to analog floating mode. This greatly reduces the current consumption by the micro controller. The peripherals required for debugging the code are placed here. Before deployment, the code will be removed. This phase is referred to in the program as the System Init and Clock Configuration. It is the first phase to be run. The next phase in the Set-up is the Power and Reset State Check. If any power event occurs, a software reset is generated, and the program will restart from the main() function. When this happens, a flag is set in the RCC_CSR. This can occur in the form of a brown out, Pin reset or Low Power event. This phase will check for the occurrence of any event and handle them before the program enters the main loop. Finally, if successful the program will enter the main loop and the firmware will begin.

5.2.1 Power Mode Selection

The focus on development optimizing for power consumption as well as accuracy. The system requirements are extremely flexible since the required sampling rate is very slow for example, the largest consideration of the system is Accelerometer sensing which has a maximum expected sample rate of 100Hz. For this reason, high speed computing techniques are not required and do not require much optimization. Since the system will most likely be in a wait state for the majority of its operation, It is important to place the device in as low power mode as possible to minimize consumption. This will be elaborated on in the following sections The biggest Consideration with system operation is clock speed and source. The STM32l4 has 5 possible options: 3 internal oscillators (MSI,LSI,HSI) and 2 external crystal oscillators (HSE and LSE) these clock sources will provide power to the peripherals as well as the RTC. According the reference manual, the real time clock must be clocked from the LSE 32.768KHz crystal in order to provide an accurate calendar function therefore, the RTC must be clocked from the LSE no exceptions. The external crystal oscillators provide high precision clock speed with extremely low drift however, the power consumption of these oscillators are much higher than the internal RC. The clock configuration of the STM32L4 allows for a combination of these oscillators in a Phase Locked Loop (PLL) which allows for a greater degree of accuracy at desired speeds.

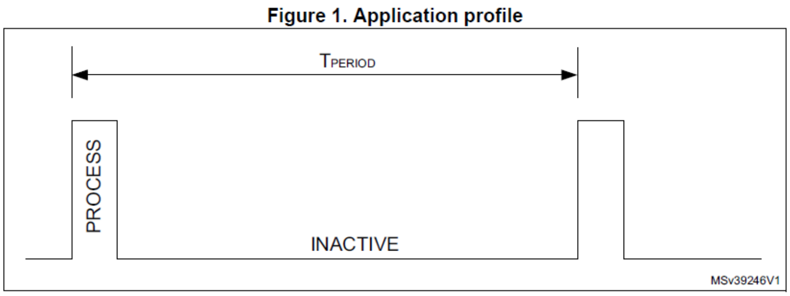

Figure 5.2: Diagram showing a general low power operation profile for the micro controller with two distinct phases: Process and Inactive occuring over a period T

Figure 5.2

above details a typical low power operation Which can be expected from the buoy For a typical application, we consider two main phase:

1. Process phase: System is in run mode with peripherals are active at regular intervals.
2. Inactive phase: System is asleep until RTC/GPIO event.

Once the buoy has finished an active routine, the system becomes inactive between samples. The buoy is designed to operate in routines occurring once every half an hour. Once the routine is complete, it still has to wait an extremely long time before it is required again. This is the inactive between sample mode and consider this our period of inactivity where we can place the device in the lowest possible state with very little concern for wake-up time or peripheral settings.

Therefore, the following power modes were selected for each phase of the system's operation

Table 5.1: Table showing the power mode selection for each phase of the Buoy's operational cycle

Phase	Power Mode	Current Draw
Process	Run Mode	1.16mA
Inactive	Standby Mode	710nA

Table 5.1 above shows the estimated current consumption taken from the STM32L4 datasheet. The Current Value for Run Mode was bench-marked using a Dhrystone Test with an system clock of 24MHz and code loaded from Flash. The Inactive current draw was estimated with a Low Speed External Oscillator supplying the Real Time Clock.

5.2.2 Clock Selection

The biggest Consideration with system operation is clock speed and source. The STM32l4 has 5 possible options: 3 internal oscillators (MSI,LSI,HSI) and 2 external crystal oscillators (HSE and LSE). Since the buoy will be inactive for long periods of time, an accurate 1Hz reference signal is required to keep calendar date and time. In addition, The STM32 microcontroller features a variety of wake up options to transition from low power mode to run mode

1. Internal configurable Alarm
2. Periodic Wake Up Alarm
3. External Wake Up Pin

These options are made available through an internal Real Time Clock on the STM32L4 microcontroller. The peripheral can receive input from multiple clock sources such as an external Low Speed Oscillator (LSE), an internal Low Speed Oscillator (LSI) or an internal High-speed Oscillator (HSI). The peripheral also allows for fast and simple data storage during extreme power down modes. When the device enters shutdown mode, RAM is turned off, therefore all data will be lost. The RTC has 32 back up registers capable of retaining 1Kb of data when the device is powered down.

these clock sources will provide power to the peripherals as well as According the reference manual, the real time clock must be clocked from the LSE 32.768KHz crystal in order to provide an accurate calendar function therefore, the RTC must be clocked from the LSE no exceptions. The external crystal oscillators provide high precision clock speed with extremely low drift however, the power consumption of these oscillators are much higher than the internal RC. The clock configuration of the STM32L4 allows for a combination of these oscillators in a phase locked loop (PLL) which allows for a greater degree of accuracy at desired speeds. The final clock configuration parameters are shown in the table below:

Table 5.2: configuration parameters for the system clock and Real Time Clock including sources and frequencies

Run Mode System Clock Source:	MSI and LSE in a PLL Configuration
Clock Frequency:	24 MHz
Shut Down Mode Clock Source:	LSE
RTC Clock Frequency	1 Hz
LSE Clock Frequency	32.768 KHz

5.3 Firmware Overview

In a multi-sensing system, it is important to manage the interactions and data flow between the various aspects of the system to ensure the device operates in a predictable, manage manor. To achieve this, a state machine can be implemented to provide a high-level form of control over the system. This can be achieved by decomposing the overall function of the buoy into a series of finite states. These states are connected through a series of transitions which can be described using Boolean techniques. Through this, the buoy retains a modular structure both in firmware and in hardware which can allow for additionally sensors and functions to be implemented seamlessly.

5.3.1 Execution

The goal of the buoy is to sample environmental, GPS and power data at a fixed rate. This rate T_{sample} will be used to describe the period between sampling the devices. Each Sample will be condensed into a byte packet and stored in flash memory at a sector. After every 4 samples, the device will load the packets from memory into a buffer and transmit the data. When the device exits this state, it will reset the sample count and repeat until the buoy is turned off or loses power. The buoy can therefore be broken down into a set of finite states which are shown below:

1. **Initialisation State:** The device initializes the counter and verifies the sensors.
2. **Reset State:** Counter and memory Variables are Reset
3. **Sample State:** During this state, the device actively receives data from the sensors and stores them into a packet which is then saved to Memory
4. **Sleep State:** The device enters this state between samples and active states. Here, the device will remain in this state for a time T_{sample}. After which, the buoy will wake up
5. **Transmit State:** The device will load the data from memory and transfer to the Iridium Modem Buffer. Upon successful transmission, it will enter the Reset state

Each state will control which routines are performed during the function and provide the system with information on the current status of the device. Should the device encounter a hardware reset, the system can recover and predict the action it needs to take based on the last state the system was in. A typical system run is shown in the figure below:

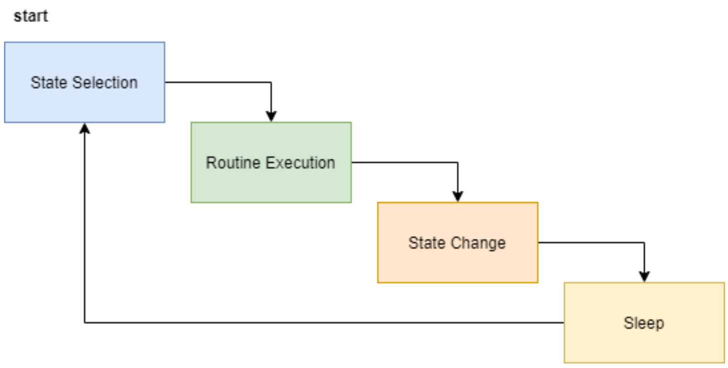

Figure 5.3: Diagram showing the steps executed from wake up when

The inputs to the state machine are:

1. C: a 2-bit integer signifying the number of samples performed ($0 \leq N < 4$)
2. T: Variable that matters when the system is asleep. Signifies whether the system has been in sleep mode for a time defined by the constant value T_{wake}

The system has no explicit outputs however, the state machine is used to control which routines will be executed during the execution phase of the program. Therefore, the outputs can be considered as the Routine Rx as shown below:

1. R_{sample}: Sensor sample routine, this can involve all the sensors or just a select number. For simplicity's sake, this period implies all sensors will be sampled from
2. R_{sleep} : Device is in a sleep state and will wake up when the periodic wake up unit counts to a time T_{wake}
3. $R_{Transmit}$: Satellite Transmission Routine

Given the following information, the Algorythmic State Machine (ASM) chart is derived and shown in the figure below

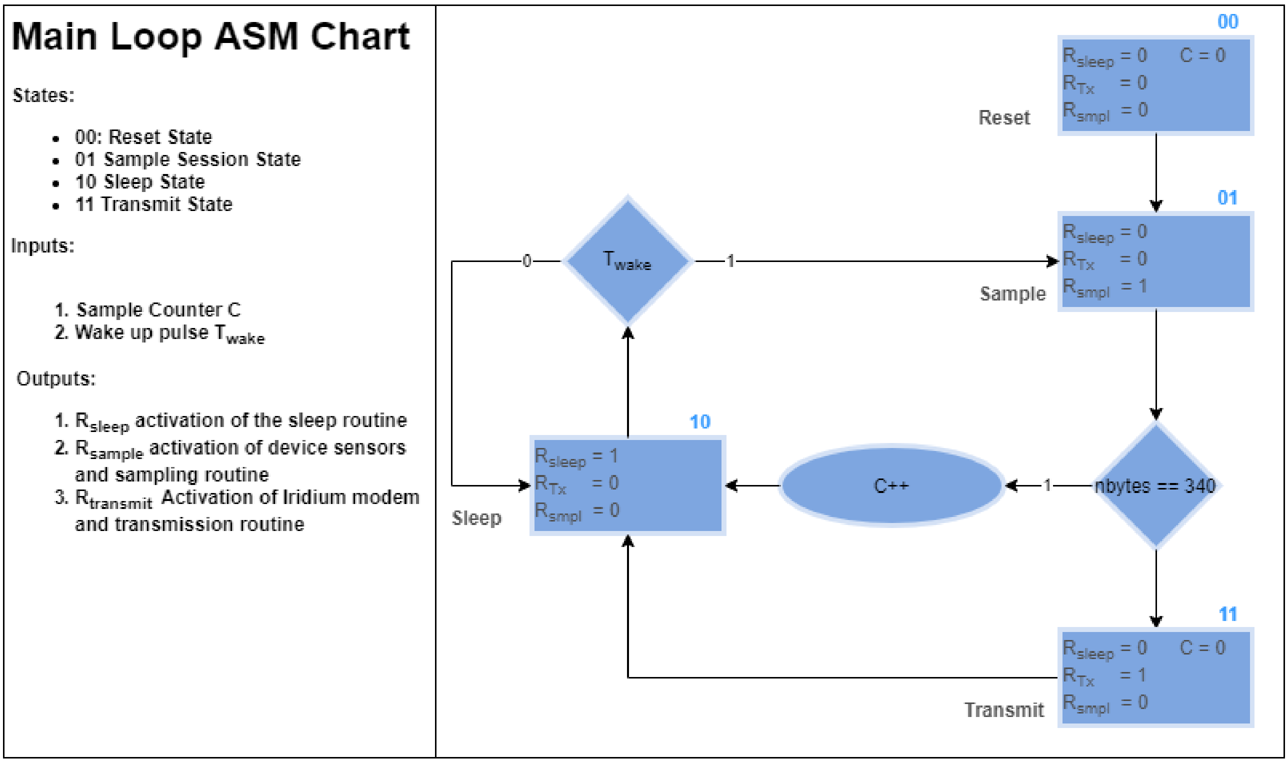

Figure 5.4: ASM chart for the proposed program to run on the processor showing entry/exit conditions and functions to be run during states.

Figure 5.4 above shows an abstract representation of the logical flow of the program. A typical run from the system will have the buoy initialised and calibrated before entering the main loop where it will alternate between active sampling and inactive sleep mode until enough data has been collected to transmit. This allows the Iridium modem to only be turned on when needed thereby significantly conserving energy while allowing for the system to sample as much as possible. The variable T_{wake} is user defined and sets the sample rate of the system For this application it has been set to 30 minutes. The device will sample 4 times with 30 minute intervals in-between and transmit the data on the 4th cycle i.e. every 2 hours.

The RTC periodic wake up unit is used as a counter in deep sleep mode. This is a 16-bit down-counting Auto Reload Register that generates an interrupt on an internal wake up line when the system has Slept for a length of time T as defined by the user. In addition, the sample counter gets reset after every transmission state and when the buoy enters a reset state. The number of samples before transmission is chosen to be 4 to optimize packet size for the transmission buffer. Since the Iridium Buffer is 340 Bytes long and the Transmission rate is per 50 bytes, the goal is to transmit as much data that would fit into the buffer as possible. Too frequent transmissions incur a high data cost but result in data integrity. Too few transmissions can result in lost sample points if a transmission is not received.

5.3.2 Asynchronous Behaviours

Asynchronous behavior describes all functionality that occurs outside of the main loop. This can come from Interrupts/ External events which causes the system to exit the main loop regardless of state and execute the code. This can occur from the following sources:

1. Interrupts
   (a) Iridium Message Received (Ring Alert)
   (b) IMU Event Detection (Collision / Free-fall detection)
2. Events
   (a) Low power detection.
   (b) Brown out detection.
   (c) Software resets.
   (d) Watch Dog resets.

These events take precedence over the main loop function. The table below shows the entry/exit conditions. Functionality as well as return state after exit. A full description of events, interrupts, and the protocols for handling them are shown in tables C.1 to C.5 in Appendix C.1. The figure below shows how the event handling procedure is sequenced in the main program:

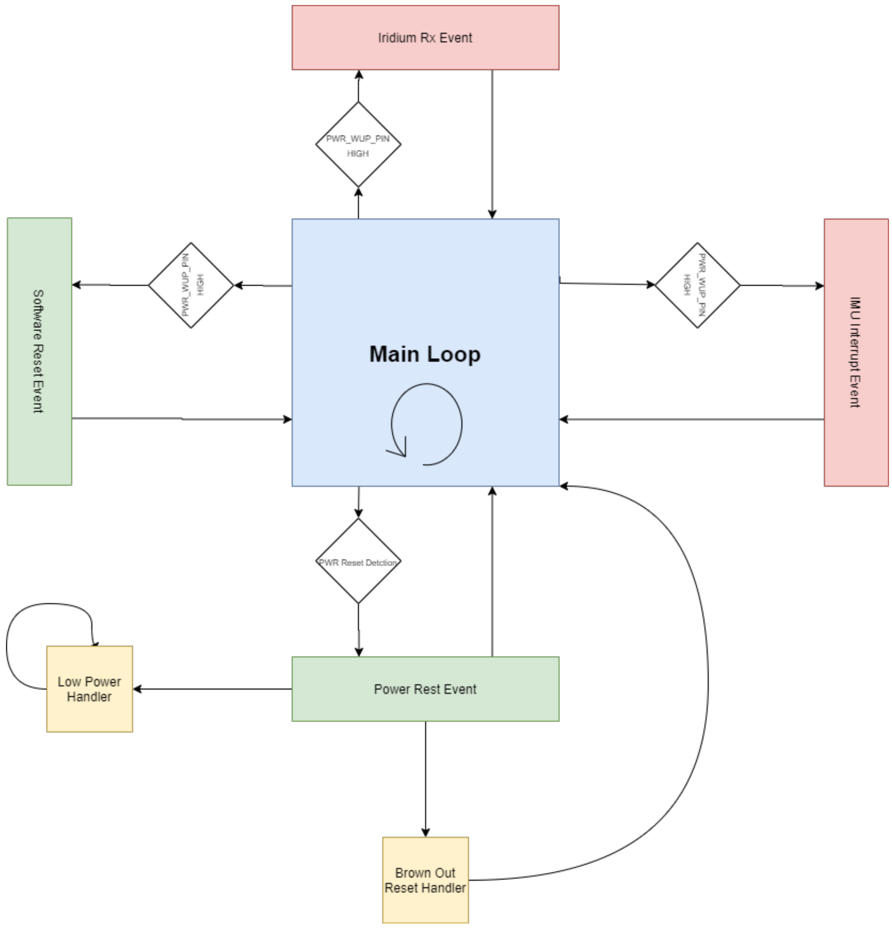

Figure 5.5: Application Diagram with Event and Interrupt sequencing

States are represented by integers on the system and are stored in the back up registers of the RTC. These registers keep data even when the device is in low power mode or a software reset has occurred therefore making them the perfect storage location. The State Variable holds the value of the current state of the buoy. This variable is stored in two locations: When the system is in run mode, the value is stored in the global variable *Current_State*. When the device is in a deep sleep state, The variable is stored in the RTC Back up registers at byte 0 of Back-Up Register 0. Upon wake up, the value is loaded from the register and placed in the global variable.

The main loop follows a sequential state transition as described in Figure 5.5. To achieve this, at the start of each loop, the program reads the value stored in the state variable. This determines what the previous state was. Based on this value, the new state is determined and stored in the state variable. This process is shown in the figure below.

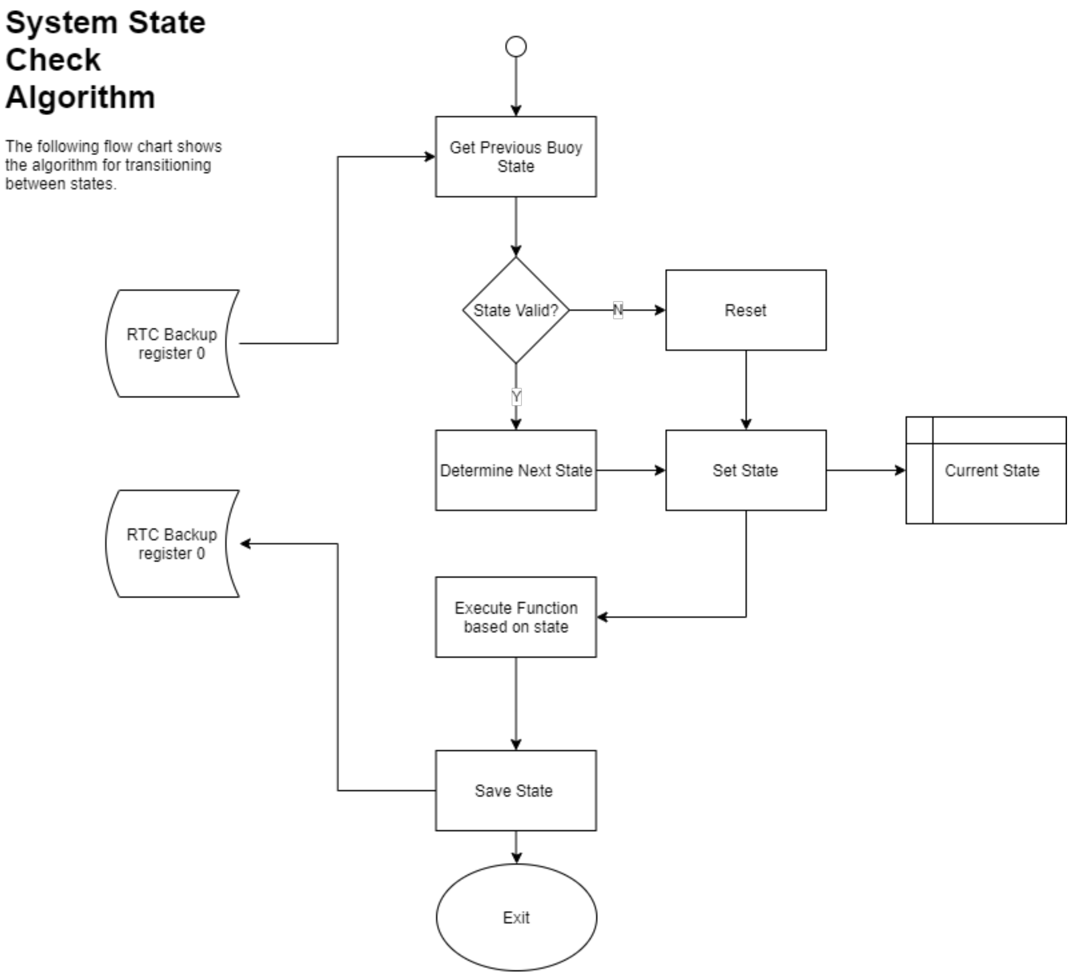

Figure 5.6: Flow chart for the state-check algorithm

Figure 5.6 above shows the algorithm for selecting and transitioning between states. This algorithm allows for states to be linked in any order and, most importantly, Separates the state selection from the state function. By separating these two concepts, a more modular framework is created. This allows for the addition of more states and transitions without modifying the routines that are currently in place. This allows for device functions to be turned on and off as desired without drastic changes to the firmware.

Finally, Asynchronous States take a higher precedence over the main loop states and therefore are checked before the state check shown above. The order of precedence is shown in the table below:

Table 5.3: Table showing the types of states that the system checks for ordered by priority with 1 being the highest priority and 3 being the lowest

Name	Priority
Power Event	1
Asynchronous Interrupt	2
Sequential State	3

Power Events generate a system reset and raise a flag in the PWR Status Register. When the flag is set, the program enters the handler and, if the event is non-fatal, returns to the main loop. The following flow chart shows an example of such a case for a Brown Out Event

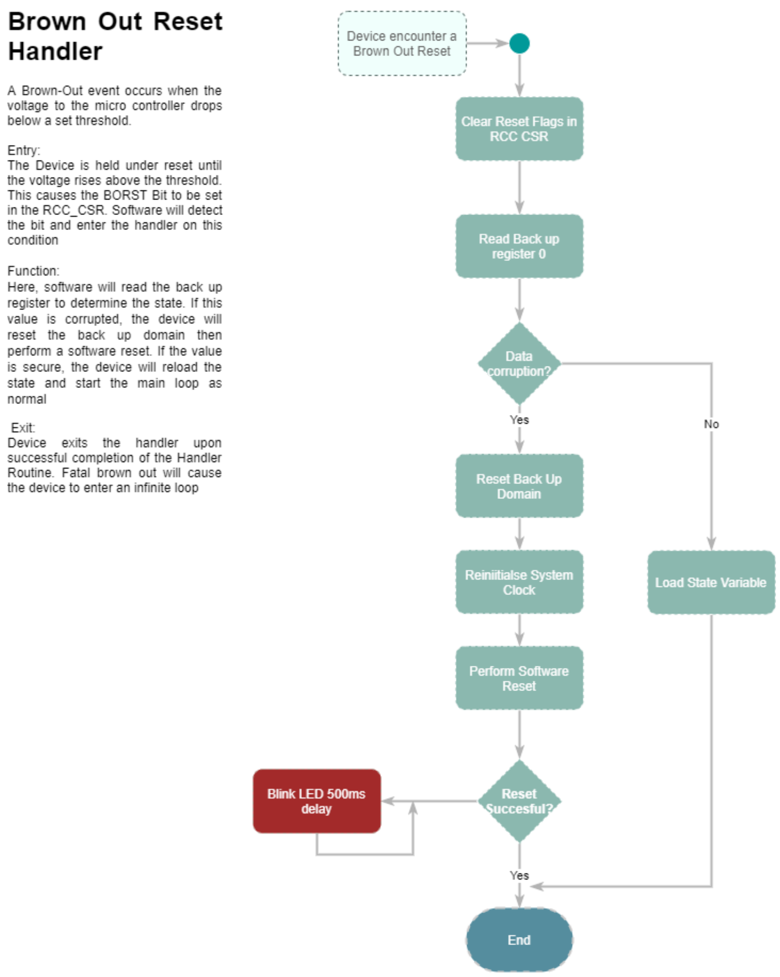

Figure 5.7: Diagram showing the algorithm for Brown Out Event Recovery and Handling

Some sensors have interrupt pins and can be configured to trigger upon detection of a specific event. When this happens, the sensor will send a digital high on the interrupt pin. On the processor side, a hardware interrupt is generated and the software handles the interrupt. An example of such a prceedure is shown in the figure below

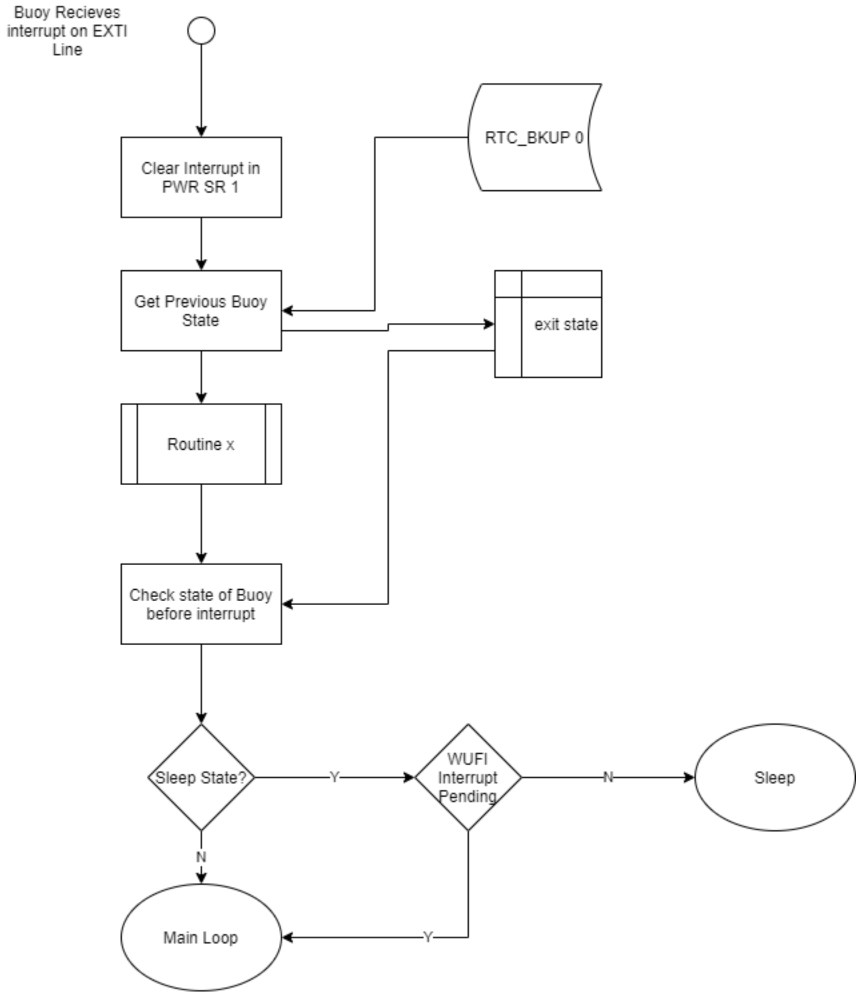

Figure 5.8: Diagram showing the algorithm for handling an external interrupt from a Wake Up pin connected to one of the modules

By connecting these pins to external wake up pins, the buoy is capable of event detection in deep sleep mode. If an event is detected while in deep sleep, the interrupt causes the buoy to wake up and resume from the beginning. No interrupt handler is entered at this point. A flag is set the PWR_SR at the position of the wake-up pin it detected. The buoy will enter the asynchronous state depending on which flag is set and will execute the routine associated with it. When the buoy wakes up from an internal wake up timer, the pins are reconfigured into GPIO EXTI mode which allows the buoy to receive interrupts when active. Note: by keeping the buoys configured as wake up pins, the system will reset when an interrupt is detected.

5.3.3 Subsystem Execution

When a module is is being used at any point in the program. The micro-controller will execute an initialise routine. This will enable any required peripherals for communication with the subsystem. This function will be called before every sample period in case the system encounters a power surge or an unexpected reset. Additionally, placing the micro controller in deep sleep mode results in the registers being reset upon wake up. The initialisation routine is specific to each micro-controller and includes the following:

1. High Level Communication Peripheral Configuration
2. Low Level Pin configuration
3. Sensor Verification function
4. Sensor Configuration function
5. Return Status

The outcome of the initialisation routine is evaluated based on a return status from the function. Items 1 - 3 are included to configure the subsystem to adhere to the functional requirements in table 3.8. Sensor Verification functions are included to satisfy acceptance Tests AT001 and provide evaluations for acceptance tests AT002 and AT004. The initialisation function is designed handle fail modes by evaluating the system's failure return type and responding in accordance with the protocols outlines in acceptance Test 2. Initialisation routines for each subsystem is provided in Appendix C.1 to C.6

If the initialisation was successful, the program will continue using the module in the firmware. Should a failure occur, the system will attempt to reconnect with the device a predefined number of times. In case of a critical failure, the system will acknowledge that it can no longer use the device and will continue the main firmware without it. The resulting behaviour is shown in the table below:

Table 5.4: Table Showing the device behaviour in case of a critical failure in one or more of the subsystems. Critical failures are defined in AT006 (table B.7) testing protocol.

Device Failure Case:	**Impact:**	**Result:**
Iridium	Critical	No data will be transmitted from the buoy
Flash Chips	Critical	Data will be lost when power is reset
GPS	High	GPS data will not be captured
MPU6050	High	Unable to measure Waves in Ice
Environment Sensor	Medium	Environmental data will not be captured
Power Monitor	Low	Current and voltage measurements will not be captured

5.4 Data Management

A critical consideration for the system is the flow of data and memory Management. The flash chips provide a solution for permanent storage however, it is critical that data integrity be maintained.Some form of data organization must be implemented for intelligent retrieval/ storage of data in a meaningful way. In addition, the system requires some form of back up should the device be unable to connect to the flash chips.

The flash Chips being used are AT45DB641E SPI Serial Flash Chips. Each chip can hold up to 64Mbit of data. Data can be read/ written at speeds of up to 85MHz of

15MHz in low power mode. The device is low power with high data retention requiring a supply voltage of 1.7V – 3.6V and draws a maximum of 11mA in Active Read mode thereby making it one of the lowest power consumption components in the system. In addition, the device comes with 2 x 256byte buffers that can store data while a read/ write operation is taking place. Memory is Organized into sectors (2 – 256 Kbs long), blocks (2kB long) and pages (256 bytes) with write, read and erase options at each level.

In this section, the data requirements from each sensor is listed. The optimal storage strategy is to convert the measurements into binary data and store as an array of bytes at known locations in an array. The data requirements for each component is listed below

5.4.1 Drift Data Acquisition

This section describes how data is aquired from the sensors to form an Ice Drift measurement. Readings are taken from the GPS and environmental sensor with the power monitor being sampled to provide an update on the buoys performance.

The GPS is sampled 4 times over a given interval. The interval between samples can range from 15 minutes to 30 minutes. At each sample point, the following data is recorded

1. Time and Date Information
2. Geographical Coordinates
3. Dilation of Precision
4. Diagnostic Information

By Default, the Ublox Neo GPS series uses the National Marine Electronic Standards (NMEA) [1] format to send messages. This message structure can vary depending on the type of message being sent/ received however, these message follow the same format:

Table 5.5: Breakdown of a typical NMEA message string with fields indicating start/stop sequences and character information.

$	Address		Data Field	checksum	End Sequence
	TT	SSS			

- $ - Character denoting the start of the sequence
- Address - This is a 5 character sequence that is used to provide information on the Talker ID (TT) and the the type of information in the Payload (SSS)
- Data Field - Data in this field is formatted as a character sequence separated by commas. This field holds the payload specified by the payload information characters in the address field

[1] Information about NMEA messaging on the UBlox Neo GPS is taken from the Interface description here: https://www.u-blox.com/sites/default/files/NEO-M9N_Interfacedescription_%28UBX-19035940%29.pdf

- checksum - Sequence of characters denoted by a "*" and followed by two bytes in ASCII hexadecimal format. These values are calculated by performing an XOR operation on all the bytes between the "$" and "*" characters
- End Sequence - 0x0D, 0x0A denotes the end of the NMEA message

Each NMEA message holds different information and can vary in the message size. To ensure a standardised data flow, The following table shows the NMEA messages that were selected and the data as well as the format of each of the fields:

Table 5.6: Description of ZDA Message string showing variables, description and how the example datum 5th September 2002 08:27:10 am is stored

ZDA - Time and Date		
Description:	Datum information in UTC representaion	
Variable Name	**Format**	**Example**
UTC Time	hhmmss.ss	082710.00 - 08:27:10 am
UTC Day	dd	05 - 5th
UTC Month	mm	09 - September
UTC Year	yyyy	2002
Time Zone Hours	hh	00 (+00)
Time Zone Minutes	mm	00 (+00)

Table 5.7: Description of GSA Message string showing variables, description of parameters and how the variables are stored

GSA - Fix Diagnostic		
Description:	DOP, number of satelites and fix type	
Variable Name	**Format**	**Example**
Opperation Mode	A/M	A - Automatic
Navigation Mode	Number (1-3)	1 - No Fix
Satelite ID	Number	29 - Satelite number
Direction	C	E - East
PDOP	Float	1.91
HDOP	Float	1.18
VDOP	Float	1.14

Table 5.8: Description of GLL Message string showing variables, description and how a set of coordinates e.g. (47°17.11364'N, 8° 33.91565') is stored

GLL - Geographic Coordinates and Fix		
Description:	latitude and longitude with postional fix information	
Variable Name	**Format**	**Example**
Latitude	ddmm.mmmmm	4717.11364 - 47°17.11364'
Direction	C	N - North
Longitude	dddmm.mmmmm	00833.91565 - 8° 33.91565'
Direction	C	E - East
Fix Status	A	A - Valid

The UBlox Neo Module continuously outputs data at a fixed rate of 1Hz (U-Blox, 2020) through Universal Synchronous/Asynchronous Transmission. The device comes preset with certain messages activated. The required messages need to be enabled by writing to the *CFG-MSGOUT* register. Then, Message parsers were written to extract the information for the aforementioned message strings and convert them into binary representation. These message parsers contain a check for validity. This algorithm first checks that the data follows the correct NMEA formatting as shown in Table 5.5. Then it analyses the Address to ensure that the Talker ID and and Message ID are valid. Finally it calculates the two byte checksum by performing an exclusive or on all the bytes in the data field and compares them to the checksum bytes that were sent with the packets. Message parsers were written for GLL, GSA and ZDA messages and were called based on the return status of the validty check. The following table shows the memory allocation for each variable.

Table 5.9: Data collected from the GPS in a single sample session.

Variable Name	Variable Type	Size (bytes)
Epoch Time	Unsigned 32-bit Int	4
Latitude	signed 32-bit Float	4
longitude	signed 32-bit Float	4
HDOP	Unsigned 8-bit Int[2]	2
VDOP	Unsigned 8-bit Int[2]	2
PDOP	Unsigned 8-bit Int[2]	2
Diagnostic Info	Unsigned 8-bit Int	1
	Total:	19

Time and date information were combined and converted into Unix Epoch Time. This represents the number of seconds that have elapsed since a defined epoch (1 January 1970) which allows for a single, 4-byte variable to represent both time and date. Geographic coordinates have been converted into singed 32-bit floats with the sign representing the direction of the coordinate. The coordinates were then split into an array of 4 unsigned 8-bit integers and recombined using IEEE-754 as a standard. The dilation of precision represents a value between 0 and 99.99 therefore, the optimal storage solution is to allocate a byte for the digit and a byte for the precision. Finally, diagnostic information includes the Fix type and the number of satellites. A maximum of 15 satellites can be used to determine a position This data can be stored in the lower 4 bits of a single 8-bit integer. The fix type is a number from 1-3 therefore only taking up 2 bits.

The BMP contains 2 onboard Analog To Digital Converters (ADCs) which are used to convert the pressure and temperature measurements into unsigned byte strings.Each measurement is stored as 3 unsigned 8-bit integers in 3 registers and must be read sequentially in order to get the full measurement. Once retrieved, the data must be combined into a 24-bit word which results in the raw, uncompensated ADC value. The BMP also contains a configurable Infinite Impulse Response (IIR) filter as well as configurable oversampling parameters for the pressure and temperature measurement. Data is read through an SPI communication interface into the micro-controller by performing a bust read of 6 bytes. To compensate for the mechanical effects of each sensing element, the device comes preloaded with a set of compensation parameters for the temperature and pressure reading (Bosch Sensortech, 2018). The compensation algoriintthms are shown in Appendix C.8 and C.7. The output of the compensation algorythm are shown in the table below

Table 5.10: Description of output values from BMP280 post processing.

Name	Type	Format	Example	Total Bytes
Temperature	signed 32-bit Integer	CCcc°C	2508 - 25.08°C	4
Pressure	signed 32-bit integer	PPPppp KPa	100653 - 100.653 Kpa	4
			total:	8

The INA219 samples Current across a shunt resistor of a known value. In thiss application, the shun resistor provided is 0.1Ω. The device also samples the Voltage accross the shunt resistor which passes through a programmable gain amplifier before being sampled by and ADC. The sensor stores data as 16 bit integers. Negative values are stored in two's compliment formed. Data is transferred via I2C to the microcontroller after the conversions have taken place. The sensor measure both shunt and bus voltage which, when combined, provide an estimate of the Load Voltage. The resolution of the values can be programmed as either 9-bit, 10 bit or 12 bit. When the device is initialised, it needs to be calibrated. Calibrating the device begins by specifying the User's power requirements and maximum current range. THe Bus range voltage is chosen as either 16V or 32V. The output of the calibration procedure is a 16-bit word that is written to the Calibration register. The algorithm used to calibrate the sensor for the SHARC Buoy application is outlined in Appendix C.9 with the following parameters:

Table 5.11: Description of parameters used to calibrate the INA219 current sensor

Maximum Bus Voltage	16V
Maximum Expected Current	1.2A
Shunt Resistor	0.1 Ω
Shunt Voltage Range	± 160mV

The Sensor calculates the power consumption as a signed 16 bit number by multiplying the Bus Voltage with the Current and placing it in the Power Register. The microcontroller performs a burst read of the Bus Voltage, Shunt Voltage, Current Voltage and power register and stores the values as signed 16 bit integers. The bus voltage register reserves the first 3 bits of the register for signal flags. Therefore, the bus voltage reading is shifted by 3 bits to the right to remove them. Finally, the Power reading is multiplied by the LSB size calculated in the calibration function which results in a signed 16 bit integer representation of the power in milliwatts. The data requirements are shown in the table below:

Table 5.12: Description of output values from INA219 current sensor.

Name	Type	Format	Example	Total Bytes
Shunt Voltage	Signed 16-bit Integer	vvvmm	18049 - 180.49mV	2
Bus Voltage	Signed 16-bit Integer	VVvvv	08025 - 8.025V	2
Current	Signed 16-bit Integer	IIIii	51234 - 519.23 mA	2
Power	Signed 16-bit Integer	PPPPpp	28130 - 2813.00mW	2
			total:	8

5.4.2 Wave Measurement Data

This section describes how data is acquired for Waves in ice measurements. The Inertial Measurement Unit (IMU) provides 3 axes of acceleration and 3 axes of angular velocity which are the components used to estimate the significant wave height, dominant wave frequency as well as the spectra and co-spectra over the sample period. Wave Data sampling occurs after the 4th drift measurement is taken and the IMU is sampled. The sample frequency was chosen to be 5Hz to be above the Nyquist frequency of the dominant wave frequency.

The MPU6050 IMU is a micro electrical-mechanical (MEM) based system. The device measures the inertial axis reading which is then digitised using a 16-bit ADC for each axis of the accelerometer and gyroscope. Communication is performed using I2C where the pin AD0 is used to set the I2C address. In addition, the device is fully configurable allowing for programmable ADC full scale resolutions and sample rates. The device also contains an on-board digital low pass filter, the bandwidth of which can be programmed through the *CONFIG* register.

The MPU6050 is an 8-bit device. Measurements from the ADC are split into 8-bit bytes and stored across 2 registers (one for the most significant byte, and one for the least significant byte). A burst read operation is performed to retrieve the data in the register. The two bytes are combined and stored as a signed 16-bit integer. This value is then multiplied by a sensitivity factor which results in a float representing either the acceleration in ms^{-2} or the angular velocity in $^{\circ}s^{-1}$. The sensitivity factor is determined based on the selected Full Scale Range of the accelerometer and gyroscope. Therefore, the following table gives a breakdown of a single sample of IMU data:

Table 5.13: Description of output values from the MPU6050 IMU showing variable name, size and significance

Name	Type	Total Bytes
x-axis Acceleration	Signed 16-bit Integer	2
y-axis Acceleration	Signed 16-bit Integer	2
z-axis Acceleration	Signed 16-bit Integer	2
x-axis Angular Velocity	Signed 16-bit Integer	2
y-axis Angular Velocity	Signed 16-bit Integer	2
z-axis Angular Velocity	Signed 16-bit Integer	2
	total:	12

From our user requirements the sample period for collecting wave data is a minimum of 15 mins. Average ocean wave sample periods are recorded at 20 mins sometimes even as high as 30 mins for significant wave height. Using Nyquist sample theory, the dominant wave frequency occurs at about 1 Hz. Sampling at 2 Hz (Kohout et al., 2015) is a bare minimum however, 5Hz is recommended.

Sample Period:	20 minutes
Sample Frequency:	5Hz
Accelerometer Full Scale Range:	$\pm 2g$
Gyroscope Full Scale Range:	$\pm 500^{\circ} s^{-1}$
Digital Low Pass Filter Bandwidth:	$92Hz$

Table 5.14: Paramaters of the IMU and their configured value for this application

Finally, the total data accumulated over the required sample period is shown in the table below

Table 5.15: Breakdown of data accumulated from the IMU with the sample parameters mentioned in table 5.14

Sample Frequency	5Hz
Sample Period	1200s
Number of Samples	6000
Bytes Per Sample	12
total:	72000 bytes

Therefore, a total of 72kB is collected from each session. With the current memory configuration. a single sample can occupy 0.9% of a single Flash chip. However, due to the low bandwidth of the Iridium modem, IMU data would need to be split into packets of 340 bytes. This would require 212 transmissions to deliver a single set of data. This is not advisable due to the high current consumption of the modem as well as the long transmission times. To send all data, advanced compression techniques or a robust wave data processing algorithm needs to be implemented which falls outside the scope of this project.For testing purposes, as a proof of concept, the IMU sample period was reduced to 5.6s which resulted in 28 samples or 336 bytes of data.

5.5 Data Flow

Table 5.16: Total drift data collected during a single sample point

Device Name	Total Data (bytes)
GPS	19
Environmental Sensor	8
Power Monitor	8
Total	35

Drift data is collected every half an hour with a transmission occurring after 4 samples. The total data collected before sampling is 140 bytes. The Iridium modem has a maximum transmission buffer of 340 bytes. Therefore, all data can be transmitted at once without any advanced transmission routines required. A custom struct was defined to hold all data in a central location.

```
/*
* @brief: Structure to store data from GPS in an organised
   format. Note: custom data types from HAL_GPS.h
*/
typedef struct
{
  uint32_t Etime;    //UTC Epoch representation of time
  Coord_t coordinates; //GPS coordinates
  Diagnostic_t diag;  //Diagnostic information
  uint32_t env_Temp;  //Environmental temperature
  int32_t atm_Press;  //Atmospheric pressure
  int16_t shunt_v;  //Shunt voltage (mv)
  int16_t bus_v;    //Bus voltage (mV)
  int16_t current;  //Load current (mA)
  int16_t power;    //Power consumption (mW)
}GPS_Data_t;
```

Figure 5.9: Data struct for storing drift data collected from the sensors during a sample period where Coord_t and Diagostic_t are shown in Appendix C.10 - C.11

The struct is populated with data as each sensor completes its sampling. If a sensor fails or is unable to return valid data, the field is left blank and the program continues to sample from other sensors. This ensures that the program is robust when handling sensor fail error to meet the criteria for acceptance test AT004 in table B.5. Once the sensors have finished sampling, the data is condensed into a packet structure and stored in memory. The diagram below shows the structure of a single packet

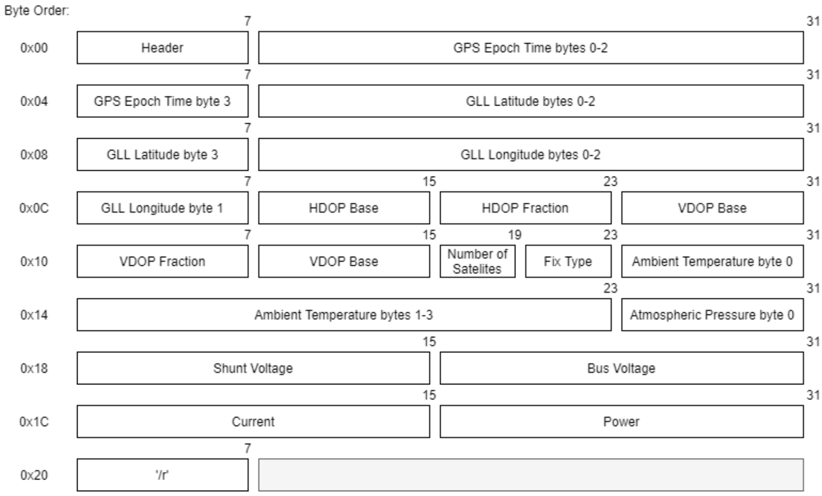

Figure 5.10: Diagram showing the structure of a drift data packet including byte position, size and data being collected

Each Packet begins with a Header. This is an 8-bit value to give information about the data in the payload. This value consist of a 4-bit identifier (0x0 for drift data) as well as a 4-bit number indicating the sample number (1 - 4) before transmission. Data is stored sequentially in little endian format as shown in figure 5.10 above. A '
r' character is used to indicate the end of the packet. This increases the total data requirement from 35 to 37 bytes per sample however, by adding the tail and the header, data integrity is maintained and allow for the standardisation of data transmission.

IMU data however, is of uniform type therefore, no special structures needed to be created. Data from the IMU is stored in an 8-bit buffer array with the most significant byte of the measurement first. Much like the drift buffer, The data was combined into a packet with a header created at the beginning. The header was given the value 0x57 or *"W"* to identify the packet as an IMU data packet. Then the data occupies the remaining bytes with the final byte of the packet assigned to the '<cr>' character to indicate the end of the packet.

Data is stored in the flash chips in packet structure form in the first page of the first available flash chip. Packets are stored sequentially until the device enters transmit state. All data is downloaded from memory and uploaded to the Iridium transmission buffer. The device initiates 2 transmission sessions. First the drift data is uploaded and transmitted, Then the IMU data.Upon successful transmission, the data is sent via satellite network to the Rock7 Rockblock server. The data is saved to a user's account and sent to their email address where the data can be downloaded as an attachment. The diagram below shows the flow of data from the sensors to the user

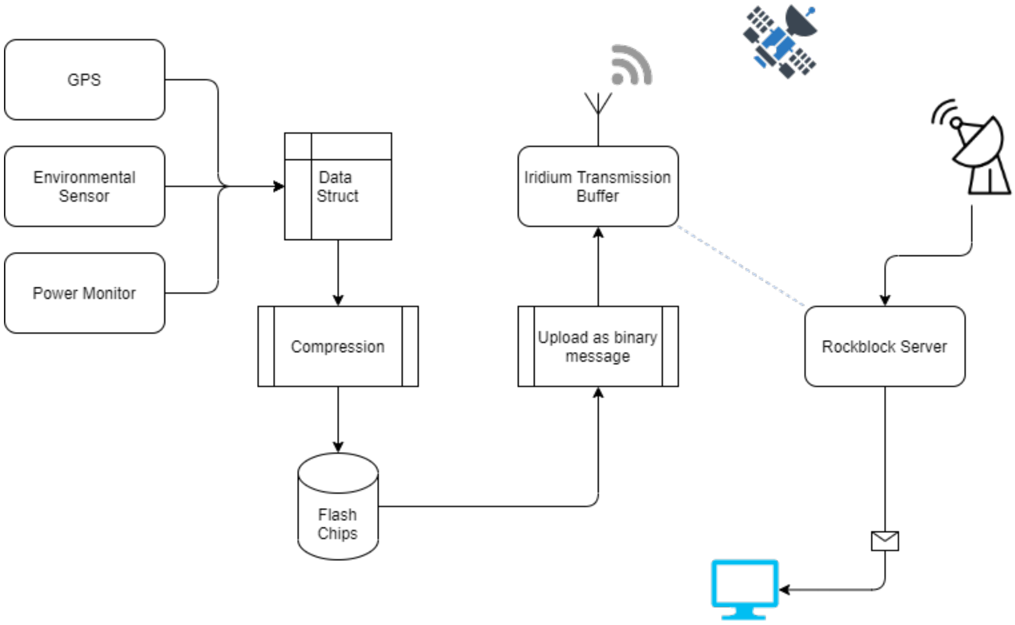

Figure 5.11: Diagram showing the flow of data during a cycle of the buoy. The data is sampled by the sensors and converted into packet form where it is stored until it is ready to be transmitted. The transmitted data arrives at a server and is sent via email to the user

Chapter 6

Testing

A final version of the firmware is validated using the standards outlined in IEEE1012[1]. A series of unit tests were written to validate the subsystems and ensure that each module conforms to the outlined specification. Due to time constraints, rigorous data validation tests were not performed. In addition,IMU data and wave simulation testing will not be included.All subsystems are tested as a proof of concept using the unit tests outlined in the design methodology and the subsytem tests outlined in Appendix E.1 to E.8. Finally, due to the 2020 COVID pandemic, final system evaluation could not be conducted in Antarctica.

Once subsystem testing was completed, the following full system tests were conducted

[1]IEEE Standard for System, Software, and Hardware Verification and Validation (IEEE, 2017)

Table 6.1: Description of accelerated system test protocol.

SYS001	
Description	Accelerated System Test
Test Protocol:	The Buoy is fully assembled with all sensors connected and configured. The sample interval is set to 10 seconds with transmission occurring every 4 samples. Batteries are inserted and the device is placed inside the enclosure.The buoy is left outside in an area with an unobstructed view of the sky. The system is left to run for an hour and the incoming data is monitored through the Rock-block data portal.
SYS002	
Description	Power Test
Test Protocol:	The buoy was connected to an external power supply with all modules powered up and enabled. The INA219 power monitor was connected to an external data logger. The data logger measures the battery current, shunt voltage and load voltage of the system, The device was set with half an hour intervals and data was recorded for a single life cycle. The buoy was also set to output time-stamped state transitions to synchronise the current draw to each state of the system
SYS003	
Description	Freezer Test
Test Protocol:	The Device was placed in a freezer for an hour to test the performance of the device in low temperatures. The device was modified to prevent transmissions from occurring. The freezer was set to $-20°C$ and the buoy status was visually monitored. After the test, the buoy was placed in a room-temperature environment where another accelerated test was performed.
SYS004	
Description	Full System Test
Test Protocol:	All modules were assembled and the buoy placed in a power off state. The sample frequency was set to once every 30 minutes with IMU data logging every 2 hours. At the end of the sample period, the device transmitted two data packets: 4 x drift data packets and 1 x IMU data packet. The data was monitored through the rock-block message portal.

6.1 System Tests

In this section, the results of the system tests outlined in Appendix 6.5 are discussed.

6.1.1 Power Test

A power test was conducted to monitor the current consumption of the buoy in various states. The INA219 sensor was disconnected from the system and connected to a data logger which sampled the Bus Voltage, Shunt Voltage, Current and Power at a sample rate of 1Hz. The buoy sample interval was set to half an hour. The device was connected to a bench-top power supply and the supply voltage was set to 7.2V input with positive and negative leads connected to where the battery was. The device was placed in a location with partially-obstructed line of site and set to run for a full cycle. The Results in Appendix F.1 shows the current consumption of the device over a single buoy period.

The average current consumption is calculated as follows:

$$I_{avg} = \frac{1}{T}\int_0^T i(t)dt = \frac{1}{T}\sum_{k=0}^{N} i(k)\Delta t \tag{6.1}$$

where the time step Δt is 1Hz and T is the total time taken for the buoy to complete 1 cycle. Then, The average current consumption and cycle duration was calculated for each phase in the buoy cycle. The results are shown in the table below

Cycle Phase:	**Phase Duration (s):**	**Average current (mA):**
Initialization State	20	494.37
1st Sample State	45	97.79
1st Sleep State	1797	115.00
2nd Sample State	8	127.96
2nd Sleep State	1797	114.41
3rd Sample Sate	7	128.17
3rd Sleep State	1797	112.87
4th Sample State (incl IMU)	12	129.71
Transmit State	135	157.01
Full Cycle:	10033	114.09

Table 6.2: Average current draw (mA) and cycle

6.2 Remote Deployment

Remote testing of the system was conducted in the Southern Ocean during the SCALE[2] Antarctica Expedition. 6 prototype systems were brought on-board and carried to the Weddel Sea with the objective of testing the suitability, basic sensing capabilities, remote communication capability and GPS signal acquisition capabilities.However, during the expedition, the initial power system began to experience instabilities resulting in system failiures. Due to time and resource constraints, alternative power supplies were made for 3 systems. 2 systems were deployed in the 1st and 2nd Marginal Ice Zone (MIZ1 and

[2]Southern Ocean Seasonal Experiment http://scale.org.za/

MIZ2) respectively with One system being deployed on the Helideck of the Ship. These systems were tested in the electronics lab before deployment. The device was deployed with a DS18B20 temperature sensor and a UBlox Neo-7m

Table 6.3: Table showing the parameters the GPS was configured with before deployment

Model:	Ublox Neo-7M
Baud Rate:	115200 bit/s
Data bits:	8
stop bits:	1
parity:	None
Active Networks:	GPS, GLONASS
Satelites:	3 - 6
NMEA Messages:	GLL, GSA, ZDA

Deployment procedure

The Buoy was switched on and sealed in the enclosure which was fastened to the tripod and placed on the deck of the ship. The buoy was placed in a basket along with three crew members who were fastened to the basket with personal harnesses. The Basked was attached to a crane, hoisted over the side of the ship and lowered towards the surface of the ocean. The crew members then identified a suitable Ice floe to place the buoy on. The floe had to have a diameter greater than 2m and visually capable of supporting the weight of the buoy. Once an ice floe was selected, the basked was maneuvered to hover 1m above the desired location.Figure 6.1 shows the deployment of the buoys in the Marginal Ice Zone using this procedure.

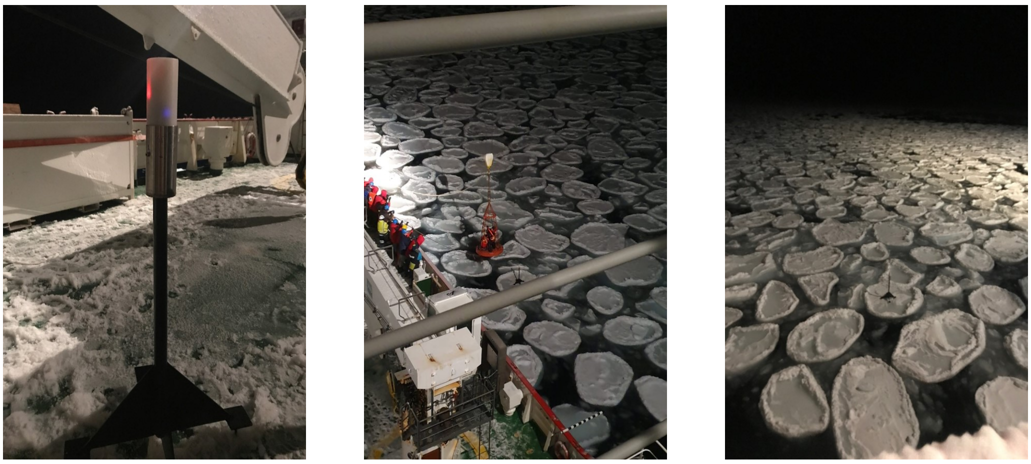

(a) SHARC Buoy System **(b)** Deployment Proceedure **(c)** Successful Deployment

Figure 6.1: Figures Showing the Fully Assembled SHARC Buoy device in a deployable state (a), The deployment procedure (b) and the results of a successful deployment showing a SHARC Buoy tethered to an Ice floe (c)

The buoy was then deployed from the basket with enough force for the spikes to penetrate into the sea ice thereby tethering the stand to the ice floe. Once complete, the buoy tracked GPS coordinates, signal diagnostic and ambient temperature. The conditions of the deployment are shown in the table below.

Table 6.4: Deployment conditions for buoy 1 (2019-WC-SB01) and buoy 2 (2019-WC-SB02) including deployment coordinates, time and environmental conditions

Buoy Serial Number:	2019-WC-SB01	2019-WC-SB02
Latitude:	$56°59'59.70"S$	$57°17'11.28"$
Longitude:	$0°0'36.96"E$	$0°1'18.30"E$
Date:	26th July 2019	28th July 2019
Time:	22h15	03h15
Air Temperature:	$-10.7°C$	$-17.5°C$

Results

The First Buoy transmitted one message after deployment before losing contact. The second buoy failed to transmit any messages. The 3rd buoy survived on the helideck for 1 week. The batteries were then changed and the buoy continued to transmit data continuously. GPS data collected from the transmission packets was compared to the GPS data recorded from the ship and the results are shown in the figure Figure F.3.

Figure F.4 shows the ambient temperature sampled by the buoy during its journey from Antarctica to East London. The data collected was compared to the data from the ship's on-board weather station.

6.3 Final Evaluation

The platform was evaluated both on a subsystem and full system level. Validation of the system occurred using the Acceptance tests AT001 to AT005 outlined in Chapter 3. Table E.9 shows the results of the acceptance tests and the traceability of the subsystems.

The full system was evaluated using Acceptance Tests AT007 to AT009. Due to project timeline constraints, rigorous calibration tests (AT006) could not be performed on all the required subsystems. The results of the Acceptance tests are shown in the table below.

Table 6.5: Results of the full system acceptance tests indicated by a ✓in the appropriate column

	Full System Acceptance:		
Unit Test:	**Fully Satisfied:**	**Partially Satisfied:**	**Not satisfied:**
AT006		✓	
AT007	✓		
AT008		✓	
AT009			✓

Full system calibration was partially satisfied. The power monitor circuit was calibrated successfully for the power supply and the IMU successfully passed the self-test however, additional IMU calibrations could not be performed. The extent of IMU functionality demonstrated by this platform is to prove functionality by initializing and sampling at a fixed known rate. Long-term data logging and wave measurements fall outside the scope of this project.It is recommended for future research to create an acceptance test for extensive IMU calibrations. Finally pressure measurements are difficult to verify without a calibrated barometer. In future work, verification of the environmental sensor should be conducted at a location with a calibrated weather station.

The system successfully completed low temperature tests in a $-20°C$ freezer and could function normally afterwards. However, visual means (LED's, active visual monitoring) were used to monitor the performance in the freezer. In the future, more extensive low temperature tests should be conducted. An additional improvement is to link the device to a data-logger and conducted low-temperature data validation tests to ensure proper operation of the buoy in low temperatures.

6.3.1 System Validation

Once the testing was completed, the final system was evaluated against the system requirements. This ultimately proves if the steps undertaken in chapter 3 had successfully fulfilled the requirements outlined by the stakeholders and evaluate the achievements of the device. These results are shown in table 6.6 below.

Table 6.6: Results of the platform evaluation and how each functional requirement was addressed.

Functional Requirement	Validation	Discussion
FR001	Fully Met	*The System shall have a protective enclosure against precipitation and frost*
FR002	Fully Met	*Enclosure shall be from strong, corrosion resistant materials with strong thermal Characteristics*
FR003	Partially Met	*The Device will protect electronics from internal humidity* - This requirement was partially met. When the device transitioned from sub zero temperatures to room temperature, condensation formed both inside and outside the device. While the electronics continued to work, this could result in unexpected failures and needs to be addressed in the next iteration.
FR004	Fully Met	*The Electronics will be elevated above the ground by 1 m to protect against freezing over*
FR005	Fully Met	textitSystem will transmit data via iridium modem
FR006	Fully Met	*System shall contain a global positioning (GNSS) device*
FR007	Fully Met	*device shall be battery powered*
FR008	Fully Met	*All Subsystems shall be rated for extreme temperatures*
FR009	Fully Met	*Device shall measure Ambient Temperature*
FR010	Fully Met	*Device shall measure Atmospheric Pressure*
FR011	Partially Met	*Device shall contain an Inertial Measurement Unit (IMU) to record acceleration (3-axes) and rotation (3-axes) of the ice floe.* - A proof of concept was implemented with the IMU capable of sampling all 6 axes for a total of 336 bytes of data. This is insufficient to calculate significant wave height.
FR012	Fully Met	*Device to contain sufficient memory for data storage*
FR013	Fully Met	*Device to contain a processing unit to control sensors and process data*
FR014	Fully Met	*Device to be optimised for low-power consumption and power event handling*
FR015	Unsatisfied	*Device shall be factory calibrated prior to shipping and delivered in a state where it can be deployed at a moment's notice* - the sensors were insufficiently calibrated to fully meet this requirement.
FR016	Fully Met	*The Device will cost less than currently available systems.* - The overall cost for a single system is: R8,421.13

6.4 Discussion

6.4.1 Power Requirements

The Initialization State is the most power intensive state drawing 494.37mA. This can be attributed to the Rockblock 9603 modem which draws 450mA to charge the on-board super capacitors. The effects of placing the modem to sleep can be seen throughout the data in Figure F.1 and Table 6.2 where the average current barely increases above 130mA. The effects of putting the buoy to sleep mode when the device is inactive results in a significant drop in current consumption as Te average current consumed during sample mode is roughly 10-15mA larger than the current consumption during sleep mode. However, this is not true for the first sample state which results in the lowest current consumption at any point in the operational cycle of the buoy.

The 4th sample state has the largest average current draw and the longest phase duration of all the sample states. This is to be expected as the inclusion of IMU sampling results in a longer data acquisition time as well as a higher current consumption. Finally, The Transmit state was expected to have the second highest current consumption since the Iridium modem was turned back on. At this point, the current draw increased to 250mA as shown in figure F.1. This occurred twice during the transmission phase. Despite this spike in consumption, the average current over the phase was 157.01mA despite multiple transmission attempts.A visual representation of the data in Table 6.2 is given in Appendix F.2

The duration of each state has a significant impact on the average current consumption of the buoy. While the initialization state current and the Transmission state had significantly higher current consumption, the phase duration of these states were significantly smaller than the sleep states. The long periods of inactivity dominated the power cycle resulting in an average current of 114.09mA. The duration of the sample states were small as a result of fast data acquisition and sampling speeds. However, the 1st sample state had the longest duration. This was due to a failure to acquire a GPS signal with 30 seconds which resulted in a timeout. The 4th Sample state also had a relatively long phase duration due to the inclusion of the IMU in the sample routine. Finally, the longest, active state was the Transmit State. During this state, multiple attempts were made to successfully transmit a packet of data and failed resulting in the relatively long phase duration. Overall, it took 10033 seconds or (2 hrs 47.217 min) whereas each sleep-state was found to be extremely consistent. This shows that the sample and transmit states have a non-negligible duration which can affect the accuracy of the sampling resulting in time delays and desynchronisations. This needs to be accounted for in the future.

6.4.2 System Performance

Figure F.3 shows that data collected from the Buoy's GPS correlated well with the data from the ship. However, large gaps appear in the Buoy's data-set. This can be attributed to signal loss or failure to acquire GPS position. In addition. the positional error appears larger for coordinates greater than $50°S$ and smaller as the trajectory approaches East

London, This could suggest that the GPS satellite signal is much weaker closer to the Antarctic continent and may be attributed to either the strength of the antenna or the spread of GNSS satellites in the region.

Figure F.4 shows that the temperature measured by the sensor was wildly inaccurate. This may be due to poor calibration of the sensor or external influences from the ship. Additionally, Missing packets resulted in large "spikes" in the data. The data, however does show a trend towards warmer temperatures which is also reflected by the ship data. Therefore, the sensor was able to characterise the change to warmer temperatures however, the data is too inaccurate to be valid. This data from version 1 of the buoy was captured with the DS18B20 thereby showing it was not practical for this application. The new sensor (BMP280) could not be verified by remote testing due to cancellations of the 2020 Antarctic expedition.

6.4.3 Mechanical Features

The mechanical features of the system successfully met the functional requirements FR001, FR002, FR004. FR003 was partially met as preliminary freezer tests resulted in condensation both inside and outside the system. In spite of this, the electronics continued to work however, a revision of the design should be made to reduce the internal humidity of the system when it transitions from a sub-zero environment to room temperature.

The mechanical features of the system, while robust, were quite bulky and heavy. The stacked PCB design allowed for robust, modular development of the system and resulted in increased mechanical strength. However, the result was increased physical size of the device and increased cost. For future iterations, a single PCB with all the components should be created. By reducing reliance on off-the-shelf development boards, the performance, size and power consumption of the system can be more carefully controlled. More over, a single PCB design requires less physical hardware to secure the system to the enclosure such as Hex spacers, screws and washers. This can significantly reduce the price of fabrication. This design was also found to create points of failures within the device. By having separate PCBs, additional wires were required to connect the boards. If a wire loses contact or breaks, the device stops working. Finally, by reducing the electronics size, more batteries could be included which can provide more power for the system.

6.4.4 Power System

The power system was the largest constraint to the device. The physical size of the enclosure limited the number of batteries included in the system and therefore lifespan of the buoy. The initial decision was to use $LiSoCl_2$ D cell batteries.These were chosen for their high specific energy and low temperature resistance. 2 3.6V batteries were connected 2 in series and 2 in parallel resulting in 7.2V into the LDO. However, in low temperature environments, the internal resistance of the batteries dropped significantly resulting in system brownouts and unexpected resets. These were exchanged for AA $LiFeS_2$. These batteries had higher stability at lower temperatures at a cost of significantly reduced specific energy. In addition, 4 cells were required in parallel to produce the required voltage thereby increasing the battery requirement.

The result was a maximum survivable period of 8 days in low temperatures $< 0°C$ and 10 days in Standard temperature. The seasonal requirement for operation is at-least a month. In order to meet this requirement, the power system requires significant revision. The Average load current was estimated to be 114.09mA over a 2 hour cycle. for a period of 30 days, the total energy consumed is $114.09 \times (30days) \times (24hours)$ or $82,114.8mA$ Future improvements to meet this requirement would be to use batteries with higher specific energy, couple the power system with an energy harvester or use a rechargeable power source. Additionally, the load current can be reduced significantly by implementing more power saving features such as MOSFET switches to turn off unneeded sensors or configuring devices such as the GPS for power saving mode.

6.4.5 Future work on wave measurements

The IMU was successfully integrated into the project however, the sampling requirements resulted in extremely large data sets requiring complex data management algorithms. Morever, the constraints of the Iridium data buffer significantly impacted the type of data that could be transmitted. The recorded time series requires compression algorithms/software processing algorithms which fall outside the scope of this course. Therefore, in terms of the project goals, the IMU only partially satisfies the requirements and more firmware development is required for wave data measurements to become fully realisable.

The MPU6050 is a low cost, 6 axis inertial measurement. This more than satisfies the requirements for analysing waves in terms of spectra, co spectra and significant wave height. The majority of devices in the field use high precision, expensive IMUs with low cost devices similar to the MPU6050 to verify the measurements. This shows that there is still room for investigation into the accuracy and performance of low cost IMUs for complex functions.

6.4.6 Short-burst Data Modems vs Telephone modems

The current version of the SHARC buoy uses a short-burst data modem with a maximum transmission buffer size of 340 bytes. This resulted in extreme data constraints which reduced the functionality of the system. Despite this complexity, the device was well integrated into the system and was able to reliably transmit data even through the enclosure. Short Burst Data is a very data limiting protocol and is not a feasible solution for real-time, raw IMU data. In future version, the Iridium 9522A would be a more feasible solution as the data buffer is much larger (1960 bytes). Alternatively, an iridium device with a sim card or continuous real time data transmission protocol.

The modem required the most design consideration. The device dominated the current sample and had the highest current consumption of all components. Therefore, the majority of software optimization was focused on optimizing the power cycle of the device.

Despite having an extremely large current cycle, the average current consumption over a 2 hour cycle was reduced significantly therefore successfully meeting the functional requirements.

6.4.7 Evaluation against the State of the Art

The final evaluation for the system was against other devices in the field. Most of these devices have been field tested to a larger extent than this device and have a higher technological readiness level. Significantly more testing is required to verify the field performance against the operation of the system.

However, SHARC buoy consumes significantly less power than the majority of devices in the field. The mode supply voltage is 12V with some devices drawing up to 18V compared to the buoy's 7.2V operating voltage.

Finally, while the SHARC buoy has more primitive modules on board, the device can, more evenly, measure a wider range of variables. Most devices generate complex measurements from single modules such as a high-powered IMU or AHRS measurement system. Devices such as WIIOS and WII buoy only contain low powered modules to compliment the measurements of the higher-powered components. This provides a unique opportunity for SHARC buoy to provide a deeper insight into performance optimization in this region.

Overall, the system shows that it is unique and fits a niche as a low powered, modular sensing device however, more rigorous tests and calibrations are required to bring the device to an overall state of technological readiness.

Chapter 7

Conclusion

The capability of automated systems as a solution for long-term in-situ, monitoring was realised in the first iteration of the Southern Hemisphere Antarctic Research Collaboration (SHARC) Buoy. The Extensive design methodology resulted in the procurement of a set of robust set of firmware which was implemented on, and tested using the first and second hardware generation of the device. The design process was heavily guided through active engagement with the key stake holders which lead to a set of user requirements to verify the performance of the system. A detailed set of specifications was derived allowing for component selection to take place. The buoy structure was designed to be modular allowing for fast, prototyping phases and long, testing phases in the lifecycle. A single, processor architecture was adopted. Hence, the firmware was designed to control the subsystems, sample and process sensor data as well as handle power events. A set of Acceptance tests and Unit Tests were written to validate the firmware thereby ensuring robust performance.

7.1 Acceptance Test validation

The mechanical subsystems were evaluated in this project however, the design of and testing of the hardware was not included in this project. All electronic subsection modules were successfully validated against the propsed acceptance tests. This was further reinforced by full system testing and short term deployments. The firmware successfully handled device non-critical failures. Controlled exits and initialisation resulted in robust communication with the sensor successfully retrieving data under non-ideal circumstances. The device was optimised for power consumption by setting a relevant processor power mode for each distinct phase of the cycle. This resulted in a significant decrease in current consumption during inactive phases. Extensive calibration testing was not performed as part of the project scope. Therefore, this requirement was only partially satisfied. Device performance during freezer tests showed promise however, more extensive testing is required to fully validate this performance.

7.2 User Requirement Verification

The average active current, and sleep current over a cycle was still extremely high failing to meet the current consumption outlined in specification SP012. The key contributors were the Iridium Modem's start-up current and the GPS operational mode. Additionally, The size of the mechanical enclosure physically constrained the size of the power source resulting in the requirements for survivability being left unsatisfied.

In spite of this, the full system software was successfully verified against the functional requirements of the project. The IMU was verified as a proof of concept. Additionally development is required to implement a wave measurement algorithm.

7.3 Full System Testing

The project concluded with a long term testing phase at home. The project encountered heavy time constraints due to the timing of the expeditions. In addition, due to the COVID-19 pandemic, all Antarctica expeditions were cancelled for 2020. Therefore, extensive field testing could not take place. Ultimately, the device passed the long term deployment test being able to execute code from start up and successful complete multiple sample cycles at the required sample frequency while accounting for signal acquisition and sensor integrity. The testing ended with the reception of data packets in the Rockblock portal with the packet structure and integrity maintained. The full system is currently expected to be deployed in 2021 through a German-led Antarctica Expedition to the Marginal Ice Zone in the East Antarctic Sea

7.4 Verification's against State of the Art

In comparison to other devices, the system requires a higher level of technological readiness in order to fully compare the performance. However, preliminary results show that the system has a significantly lower procurement cost as well as more power efficient than devices with similar specifications. These devices have more complex structures than SHARC Buoy and include higher-powered sensors that contribute to the expense of the project.

7.5 Final Remarks

In conclusion, the work presented by this dissertation successfully lays the foundation for future work and expansion of the SHARC Buoy project to take place. Significant revision to the power system and firmware optimisation are required to bring the device closer to completion. Given more time and development, SHARC Buoy can create a strong presence in Antarctic as a Multi-use system providing. Thereby solving the Antarctic Modeling problem ensuring research and collaboration overcomes adversity and provides deeper insight into the unknown continent.

Chapter 8

Recommendations

8.1 Improvements to Power Supply

As discussed in Section 6.4.1, The power system requires significant revision to improve the operational time time of the buoy. Using batteries with a higher specific energy can be a viable solution. Additionally, the power system can be revised to include a boost converter thereby allowing more batteries to be placed in parallel increasing the capacity of the power supply. An investigation needs to be conducted into the use of energy harvesters or renewable sources to compliment the power the power source. This can significantly improve the buoy's life cycle.

8.2 Improvements to Hardware

The current PCB stack configuration provides too many points of failures. It is recommended to design a single, horizontally mounted PCB with all the sensors and microcontroller. Additionally, Low-powered LED arrays can be implemented to provide visual feedback on the status of the buoy.

The device Enclosure should be redesigned to allow for a larger power supply. In addition, the enclosure should include a mechanism for de-humidifying the internal electronics.

Finally, a dedicated power board and communication module board should be designed to replace the breakout boards that the GNSS and Iridium Modem modules arive on. This will greatly reduce the form factor and reduce the reliance on connectors that can act as points of failiure

8.3 Improvements to Communication Modules

The gain of the GNSS antenna should be increased to provide a higher positional accuracy and shorter acquisition time.

The Rockblock 9603 module should be replaced with either a sim-card based modem or a modem with a larger data buffer.

8.4 Firmware Improvements

The firmware of the system was designed as a state machine. This technique is somewhat primitive since states are executed sequentially. This results in time delays as shown in Table 6.2. This can be revised by implementing a Real Time Operating System (RTOS) for critical time optimisation.

Additionally, the firmware power optimisation strategy needs to be expended to configure the GNSS for power saving modes. This will significantly reduce the current consumption of the overall system.

In this version of the firmware, a simple set of unit tests were implemented to verify the connectivity of the subsystems. It is recommended for future versions to include more extensive calibration tests for each subsystem built into the firmware or run through its own routine

Due to time constraints, a fully realisable wave data algorithm could not be implemented. This can be expended on in a future project conducting an investigation into the most suitable wave-measurement algorithm and can include full IMU calibration techniques, evaluation of the current IMU as well as open-ocean and open-ocean with rigid platform tests.

The latest hardware platform allows for critical components such as the IMU to connect an interrupt pin to an internal wake up line on the microcontroller. This feature can be expended in the future to allow for interrupts to be generated when a specific event is detected. These features can be expanded based on the following devices

GPS The device can be put to sleep and woken up when a GPS signal is acquired. Thereby reducing the reliance on polling for signal acquisition

IMU The interrupt pin can be configured to detect motion of a specified magnitude and frequency which can allow for more precise detection and measurement of significant wave height and dominant wave frequency. This feature can also be expanded to detect Ice Collisions.

Iridium The Rock block 9603 has a ring indicator pin which produces a logic high when a message is incoming to the modem. This feature can allow for ad-hoc programming of the device as well as asynchronous data retrieval thereby allowing for more precise monitoring of the device.

The move to a fully interrupt-based system will significantly improve power performance as well as reduce the reliance on timed-sequences.

8.5 Expansion of Nodes into a Network

This project resulted in the design and procurement of a single sensing node. To increase the sensing capability, the devices can be expended to form a network with an additional communication protocol (such as LORA) can provide inter-buoy communication. Future projects can include an investigation into optimal buoy topologies or designing firmware to facilitate inter-buoy communication.

8.6 Future Deployments

Following the completion of the new design, arrangements are being made to test and deploy the device through other groups. Contacts have been made with Alfred-Wegener Institute to deploy the device from the Polarstern Research Vessel. An additional prototype has been taken onboard the SA Aghulas II transporting researches to the SANAE IV base where the device will be tested on the continent before being deployed on sea ice.

Appendix A

Numerical modeling

A.1 Modeling of polar stochastic processes

In this section, modeling techniques for the polar region are explored. Here, the focus is given on developing models for Polar sea ice mechanics and dynamics. An overview of these models is given along with a description of the variables as well as the scope of each model.

A.1.1 Numerical Modeling of Sea Ice

The Hibler model is a numerical designed to investigate sea ice dynamics and thermodynamics in the Arctic region (Hibler, 1979). This model attempts to couple the sea ice dynamics to Sea ice thickness and uses this relationship to investigate the relationship between the effects of sea ice and the climate. Work so far has largely studied these effects independently using factors that largely ignore the inherent mechanical properties of Sea Ice (Hibler, 1979). Coupling these effects would allow for a more general descriptor of Sea Ice spread regions.

The model is based off Coon et al. (1974) AIDJEX (Hibler, 1979), who use plastic-elastic constitutive laws to describe large-scale sea Ice spreads. It is assumed that cracks, ridges, and leads are randomly distributed on large scales [1]. While the Hibler model is not as complex, it is more robust as it allows for larger time-steps and simplifies system boundaries. Here, sea ice is modelled using similar viscous plastic laws (Hibler, 1979) that allow for non-linear plastic flows to be modelled without severe limitations by large time-steps. The model uses the following components:

1. Momentum balance - air and water stress
2. Coriolis force
3. Inertial forces

[1] 100 km from Coon et al. (2007)

4. Constitutive laws - ice stress, strain, strength
5. Ice thickness distribution - accounting for open water patches, changes in thickness and Concentration
6. Ice strength

$$\frac{mDu}{Dt} = -mfk \times u + \tau_a + \tau_w - mg\nabla H + F \tag{A.1}$$

$\frac{D}{Dt}$ is the substantial time derivative, k is a unit vector, u is the sea ice velocity, m is the ice mass and f is the Coriolis parameter. Forces in the equation τ_a, τ_w represent the stress of the air and water respectively where F is the force related to the internal ice stresses. H is the sea surface dynamic height and g is the acceleration due to gravity. Assuming constant turning angles, The air and water momentum equations are as follows

$$\tau_a = \rho_a C_a |U_g|(U_g cos(\phi) + k \times U_g sin(\phi)) \tag{A.2}$$

$$\tau_w = \rho_w C_w |U_w - u|[(U_w - u)cos(\phi) + k \times (U_w - u)sin(\phi)] \tag{A.3}$$

where ρ_a and ρ_w are the densities of air and water, C_a/C_w are the drag coefficients, U_g is the geostrophic wind and U_w is the geostrophic ocean current

The Hibler model is the de facto numerical model for large scale ice process (Marquart et al., 2019). The model is used to describe an area of 10 - 100km^2, Small scale models are still in development (Marquart et al., 2019).

Numerical Modeling of Ocean Waves

Ocean waves are comprised of multiple spectral components with different magnitudes and wave periods knowledge of these spectral components is important for understanding the wave attenuation model (Williams et al., 2013) where, assuming the ice is modelled as a viscous fluid, wave energy is exponentially attenuated (Meylan et al., 2014)(Williams et al., 2013) with distance travelled into the ice due to partial reflections with the ice floes. The rate of attenuation is dependant on the wavelength however an exact mathematical relationship has not been found. The major issue with verifying these models is the lack of robust data availability (Meylan et al., 2014) thereby reaffirming the need for in-situ measurements.

Williams et al. (2013) describe three fundamental components of Waves in Ice Modeling. These are advection, attenuation, and ice breakage (Williams et al., 2013). Advection and Attenuation describe how energy transfer occurs between waves and ice and are dependant on the group velocity c_g and the attenuation factor $\hat{\alpha}$ which, in turn, are dependant on the frequency of the wave (Williams et al., 2013). Also, the properties of ice are significant. These include Young's modulus Y, Poisson Ratio ν, strain ϵ and viscous damping parameter Γ. The initial Floe Size Distribution and sea ice concentration are also considered. The assumption is that wave breakage feeds back into the model with a new Floe Size distribution (Williams et al., 2013).

Wave advection is described by the following energy model:

$$\frac{1}{c_g}(\partial_t + c_g\partial_x)S(\omega; x, t) = R_{in} - R_{ice} - R_{other} - R_{nl} \tag{A.4}$$

where R_{in} is the wind input energy, R_{ice},R_{nl},R_{other} represent the energy loss from ice, other sources as well as non linear energy exchanges. $S(\omega; x, t)$ represents the waves in terms of its energy spectral density (Williams et al., 2013) For this model, the energy input is considered to come only from the Rate of exchange between ocean and Ice. Hence all other energy rates are considered 0 and R_{ice} is defined in terms of $\hat{alpha}$ and S

$$\frac{1}{c_g}(\partial_t + c_g\partial_x)S(\omega; x, t) = -\hat{\alpha}(\omega, c, h, \langle D\rangle)S(\omega; x, t) \tag{A.5}$$

$\hat{\alpha} = \frac{\alpha}{\langle D\rangle}$ describes the average attenuation per ice floe. In terms of Ice thickness and wave period (Williams et al., 2013). By this definition, R_ice is quasi linear (Williams et al., 2013) since a wave with a significantly large Energy spectral density can break the floe decreasing the dimensions $\langle D\rangle$ and increase the dimensional attenuation factor $\hat{\alpha}$. The operator $(\partial_t + c_g\partial_x)$ serves as the lagrangian reference fram at a moving velocity c_g. Finally, by breaking the above model into:

$$\frac{dx}{dt} = c_g(\omega, t_*, x) \tag{A.6a}$$

$$\frac{dS(\omega; x, t)}{dx} = -\hat{\alpha}(\omega, x, t_*, S_*)S(\omega; x, t) \tag{A.6b}$$

we can describe the dynamics of the sea ice during a breaking event at a time t_* (Williams et al., 2013). Hence, the model is broken up into an advection model in A.6a and an attenuation model in A.6b.

The next step in the model is determining the mathematical model for wave energy. A stochastic approach is taken to define key wave parameters (Williams et al., 2013). The Significant wave height is found using the formula

$$H_s = 4\sqrt{m_0[n]} \tag{A.7}$$

$m_n[\eta]$ describes the mean square surface sea elevation of a particle and is derived from the Spectral Density S (Williams et al., 2013).

$$m_n[\eta] = \int_0 \infty S(\omega)\omega^n d\omega \tag{A.8}$$

The significant wave height can be considered 4 times the standard deviation of the surface elevation (Meylan et al., 2014). finally, by determining the significant wave height, the dominant wave period can be calculated as $\frac{1}{f_d}$ where f_d is the frequency at which the dominant wave period occurs (Meylan et al., 2014).

A.2 Modeling of GPS dilation of precision

Given a user's position on the earth, the distance from the user to the satellite is characterised by the equation:

$$r = s - u \tag{A.9}$$

where r is the distance from the user to the satellite, s is the distance from the earth's centre to the satellite and u is the distance from the earth to the user. By measuring the propagation time from the user to the satellite, The absolute distance $||r||$ can be calculated and hence, the pseudo-range can be calculated as

$$\rho_i = ||s_i - u|| + ct_b + v_{\rho_i} \tag{A.10}$$

where ρ_i is the pseudorange for satelite i, c is the speed of light, t_b is the clock offset and v_{ρ_i} is the noise of the pseudorange measurement and:

$$||s_i - u|| = \sqrt{(x_i - x_u)^2 + (y_i - y_u)^2 + (z_i - z_u)^2} \text{ for } i \in 1, 2, 3...N \tag{A.11}$$

where N is the number of satellites and (x_i, y_i, z_i) is the 3 dimensional position of satellite i. This represents a non-linear relationship for the line of sight of a satellite. Jwo (2001) explains that by creating a Taylor series centered on a nominal user position $(\hat{x_n}, \hat{y_n}, \hat{z_n})$ and ignoring the higher terms (Jwo, 2001). It then follows that:

$$\Delta\rho_i = \rho_i - \hat{\rho}_i = e_{i1}\Delta x_u + e_{i2}\Delta x_u + e_{i3}\Delta z_u \tag{A.12}$$

The terms e_{ij} represent the line of sight vector E_i whereas the term $\hat{\rho}_i$ is the pseudo-range at the nominal user's position. It follows that the vector E_i can be calculated as follows (Jwo, 2001).

$$e_{i1} = \frac{\hat{x_n} - x_i}{\hat{r_i}} \tag{A.13a}$$

$$e_{i2} = \frac{\hat{y_n} - y_i}{\hat{r_i}} \tag{A.13b}$$

$$e_{i3} = \frac{\hat{z_n} - z_i}{\hat{r_i}} \tag{A.13c}$$

$$\hat{r_i} = \sqrt{(\hat{x_n} - x_i)^2 + (\hat{y_n} - y_i)^2 + (\hat{z_n} - z_i)^2} \tag{A.13d}$$

Given n satellites, the equation (A.11) can be written as a matrix with the following form:

$$\mathbf{z} = \mathbf{Hx} + \mathbf{v} \tag{A.14}$$

$$\Delta\rho_i = \begin{bmatrix} \Delta\rho_1 & \Delta\rho_2 & \Delta\rho_3 & ... & \Delta\rho_n \end{bmatrix} \tag{A.15}$$

where

$$\mathbf{H} = \begin{bmatrix} e_{11} & e_{12} & e_{13} & 1 \\ e_{21} & e_{22} & e_{23} & 1 \\ e_{31} & e_{32} & e_{33} & 1 \\ ... & ... & ... & 1 \\ e_{n1} & e_{n2} & e_{n3} & 1 \end{bmatrix} \tag{A.16a}$$

$$\mathbf{x} = \begin{bmatrix} \Delta x_u \\ \Delta y_u \\ \Delta z_u \\ c\Delta t_b \end{bmatrix} \tag{A.16b}$$

$$\mathbf{v} = \begin{bmatrix} v_{\rho_1} \\ v_{\rho_2} \\ v_{\rho_3} \\ ... \\ v_{\rho_n} \end{bmatrix} \tag{A.16c}$$

The Matrix $\mathbf{H}$ is $n \times 4$ where $n \geq 4$ to calculate all the parameters for GDOP (Jwo, 2001). We can then solve for the vector $\mathbf{x}$ by taking the psuedo inverse of H i.e $\hat{\mathbf{x}} = (\mathbf{H}^T\mathbf{H})^{-1}\mathbf{H}^t\mathbf{z}$. Hence, given that the psuedo range is linearised, the quality of navigation is taken as the difference between the estimated position and the actual position (Jwo, 2001).

$$\tilde{\mathbf{x}} = \hat{\mathbf{x}} - x = (\mathbf{H}^T\mathbf{H})^{-1}\mathbf{H}^T v \tag{A.17}$$

$E\{\tilde{\mathbf{x}}\tilde{\mathbf{x}}^T\}$ describes the covariance between the errors in the components of the estimated position (Jwo, 2001) and is calculated as

$$E\{\tilde{\mathbf{x}}\tilde{\mathbf{x}}^T\} = (\mathbf{H}^T\mathbf{H})^{-1}\mathbf{H}^T E\{\mathbf{v}\mathbf{v}^T\}(\mathbf{H}^T\mathbf{H})^{-1}\mathbf{H} \tag{A.18}$$

where $E\{\mathbf{v}\mathbf{v}^T\} = \sigma^2 I$. If all components of σ are uncorrelated then the covariance becomes

$$E\{\tilde{\mathbf{x}}\tilde{\mathbf{x}}^T\} = \sigma^2(\mathbf{H}^T\mathbf{H})^{-1} \tag{A.19}$$

and thus the GDOP factor can be calculated from the RMS values of σ^2 i.e.

$$GDOP = \frac{\sqrt{\sigma_{xx}^2 + \sigma_{yy}^2 + \sigma_{zz}^2 + \sigma_{tt}^2}}{\sigma} \tag{A.20}$$

where σ_{xx}^2,σ_{yy}^2,σ_{zz}^2,σ_{tt}^2 are the RMS values of the x,y,z time components respectively. THe value GDOP can also be decomposed into the positional dilation of precision (PDOP), time dilation of precision (TDOP), horizontal dilation of precision HDOP, and vertical dilation of precision (VDOP) which characterise the effects satellite spread on the 3 dimensional position, time, horizontal position and altitude respectively.

A.3 Numerical Techniques for modeling ocean waves

A.3.1 Kuik Method

The Kuik method, developed by Kuik et al. (1988) is a computational technique for measuring and determining the directional characteristics of ocean waves. Measurement of these characteristics are derived from the pitch and roll of an ocean buoy are measured. By using an accelerometer, gyroscope or an inertial measurement system to measure the slope and heave of the 3 axes (Kuik et al., 1988), it is possible to reconstruct the sea state given a set of data provided the data is of a specific length sampled above the Nyquist frequency of dominant ocean swells. A major advantage of the Kuik method is that the parameters are estimated directly from the Fourier transform of the measured signal (Kuik et al., 1988) without assumptions about the model. Should the algorithm be used to measure waves in ice, no information is required about the dynamics of the model of the ice floe. This greatly improves the accuracy since ice floes can vary in width, distribution and area as well as change shape due to collisions, freezing and melting. Wind waves are described using a two-dimensional energy spectrum E with wave energy spread over a frequency f. The normalised distribution of energy over direction is defined according to Kuik et al. (1988) as

$$D_f(\theta) = \frac{E(f,\theta)}{\int_0^{2\pi} E(f,\theta)d\theta} \tag{A.21}$$

Finally, by computing the model per frequency, the distribution simplifies to $D(\theta)$ which can be approximated by a Fourier series with 4 terms (Kuik et al., 1988) derived from the pitch, roll and heave of a buoy. Finally, the model can fully characterise the wave spectrum by calculating the following parameters from the Fourier coefficients:

1. mean wave direction θ_0
2. directional width σ
3. skewness γ
4. kurtosis δ

The accuracy of the mean wave direction and width is affected by noise in the sampled data. small RMS values of noise can result in rapid increases of directional width by 1% to 5% (Kuik et al., 1988). Additionally, pitch and roll buoys are not free particles. They have an associated mass and therefore an associated inertia (Kuik et al., 1988). This results in a phase shift of the Fourier term by $\phi_i i \in x, y, z$ in the first harmonic (Kuik et al., 1988). This shift can result in an error of $0.5°$ for $\sigma > 25°$ to $1°$ for $\sigma < 10°$ (Kuik et al., 1988)

A.3.2 Welch-Earle Method

The Welch-Earle Method is an algorithm for calculating either directional and non-directional wave data depending on the assumptions of the input data (Earle, 1996). Data is derived from the vertical acceleration, roll and pitch of a buoy oriented perpendicular to the surface on either a vertically stabilised platform or a hull-fixed platform (Earle, 1996). Directional wave data is determined from both the acceleration, roll, pitch and heave from the buoy while non-directional wave data is calculated from time-series acceleration only. In this method, a digital time series representation of the vertical Acceleration along with 2 orthogonal Gyroscope measurements and Magnetometer readings relative to the earth's magnetic field is obtained. The method accounts for the response function of the buoy and provides corrections to phase differences as a result of the buoy's inertia (Earle, 1996). Full directional and non-directional wave data is characterised by calculating the spectra and co-spectra of the time series data. The first part of the method is developed by Welch (1967) and is used to calculate the power spectral density. Given a discrete time series data X(j) with a power spectral density P(f), |f|< $\frac{1}{2}$.this data segmented into a set of k-bins $X_k(j)|j \in 0, L-1$ (Welch, 1967). Each bin is multiplied by a selected window function W(k) of length L. Additionally, Bins are taken with a 50% overlap to produce better statistical averages (Earle, 1996) The Fast Fourier Transform (FFT) of the result is taken to for a periodograms I_k (Earle, 1996). Finally, the new power spectral estimator $\hat{P}(f_n)$ is calculated by taking the average of the K periodograms as shown in Welch (1967)

$$\hat{P}(f_n) = \frac{1}{K}\sum_{k=1}^{K} I_k(f_n) \tag{A.22}$$

where

$$f_n = \frac{n}{L}|n \in 0, 1, 2 ... \frac{L}{2} \tag{A.23}$$

Detrending is used to account for the effects of buoy motion on the time series. The inertia of the platform results in non-zero mean trends often as a result of constant wind or currents acting on the hull of the buoy (Earle, 1996). These must be discarded before the spectrum and co spectra are calculated. The resolution of the accelerometer is important for accurately tracking acceleration (Kohout et al., 2015). If the resolution is too small, low accelerations will not be recorded resulting in incorrect vertical accelerations being calculated. Kohout et al. (2015) found that a low-resolution IMU was unable to reliably flag that it had exceeded a boundary condition and hence it was discarded (Kohout et al., 2015)

The spectra and co-spectra of the directional and non-directional wave series can be calculated by computing the spectrum $S(x)$ as a function of frequency and direction (as is similar to the Kuik method). Earle (1996) show that characterisation of the co-spectra $C(x)$ and spectrum$S(x)$ can be achieved by calculating the first 4 Fourier coefficients. Finally, the sea state can be represented by calculating the following parameters

1. Longuet-Higgins directional parameters
   (a) a_0
   (b) a_1
   (c) b_0
   (d) b_1
2. Significant Wave Height H_0
3. Dominant Wave Period T_p
4. Total Degrees of Freedom TDF

5. Average zero-crossing period T_{av}
6. Zero-crossing period T_{zero}

This approach brings into account the possibility of spectral leakage however, this can be greatly minimised by sampling above the Nyquist frequency of the upper Wave frequency band (generally taken to be 0.5Hz) for a minimum of 1000 seconds (about 16 – 17 minutes). Additionally, spectral leakage can be reduced by selecting a window function with a gradual taper such as a half cosine or Hanning taper (Welch, 1967)

A.4 Temperature sensing measurement techniques

Thermistors

Modern thermistors have progressed significantly in the past decade. Up until recently, they have been considered inaccurate with uncertainty ranges of up to 5% (Tong, 2001). Thermistors are capable of providing accuracies of up to 0.01°. They consist of a semiconductor that changes its resistance in response to temperature (Childs et al., 2000). They have a faster response time than RTDs and work on the same principle for temperature measurement. However, where RTDs have a Positive temperature coefficient, thermistors have a negative temperature coefficient (Tong, 2001). These devices can operate over a substantial, albeit relatively limited, range of $-100° - 300°C$. The major trade-off with these devices is the lack of standards (Tong, 2001). Operating the device involves a large degree of uncertainty. Also, these devices are not powerful enough to accurately reach the desired ranges alone. They need to be coupled with similar devices. Finally, the response curve is non-linear. The relationship between resistance and temperature is (Childs et al., 2000):

$$R_T = R_0 e^{1-B(\frac{1}{T}-\frac{1}{T_0})} \tag{A.24}$$

where R_T is the temperature measured, R_0 is the resistance at a known temperature T_0, T is the temperature and B is a coefficient based on the properties of the thermistor. Finally, these devices are more prone to noise from excitation current.

Silicon Temperature Devices

Semiconductor temperature devices are suited to applications where the temperature ranges from -55 to 150 $°C$ these devices are capable of providing a stable output with a typical accuracy of $0.8°C$. These devices typically consist of diodes and transistors with a band gap voltage that changes with a change in temperature (Childs et al., 2000). These devices are advantageous in electronic application due to their small form, high accuracy and stability. These devices are relatively simple and have a good sensitivity to changes (Childs et al., 2000). Diodes are typically used in semiconductor devices. Here, the forward voltage drop across the p-n junction is linearly proportional to the Ambient temperature over a certain temperature range (typically 25K - 400K) (Childs et al., 2000). These devices are made out of either silicon or Gallium-Arsenide. Silicon is preferred as it has better stability at low temperatures and is cheaper however, this comes at the trade-off of a lower voltage output (Childs et al., 2000).

These Types of devices are readily available in IC forms and are manufactured in a variety of packages, types and compositions for any application. Typical devices are DS18B20, LM355 or BMP2080. Recent innovations in Silicon sensing have seen the rise of CMOS devices and Micro Electrical-Mechanical Systems (MEMS) being used more frequently (Mansoor et al., 2015). While these devices can suffer from deterioration due to self-heating, Mansoor et al. (2015) discuss that the low-power operation of these devices can offset this issue. This is advantageous for systems that are constrained by power consumption. However, a major disadvantage with these devices is that these devices work ideally with a purely DC signal.An AC coupled signal can cause significant errors in the output (Childs et al., 2000) (Mansoor et al., 2015). These errors can be the result of improper shielding and poor grounding. Hence proper shielding and grounding are required to reduce these errors. Finally, these devices require careful calibration before use.

A.5 Pressure sensing techniques

In this section, common pressure sensing techniques are discussed as well as their applications in remote sensing. Additionally, the numerical model of each sensor is given showing the relationship between the measured variable and the output signal.

Diaphragm based sensors

The current state of pressure sensing technology is driven towards Miniature MEMs version of large scale devices (Eaton & Smith, 1997). Most large scale pressure sensors consist of a diaphragm mounted on a device in a known way. The diaphragm is coupled to a device that converts the pressure to a mechanical movement which is then measured using a gauge. These senses often had a secondary sensor that would convert the mechanical movement to an electrical signal which was then measured (Eaton & Smith, 1997) these sensors determine pressure by measuring the deflection of a miniature diaphragm. This deflection is converted to an electrical signal. Typically, a reference pressure is provided as a measurement of a sealed chamber or absolute pressure port. Assuming the simplest version of this sensor i.e. a plate of uniform thickness (Eaton & Smith, 1997) The deflection w of the diaphragm is related to the pressure P by the following equation: (Eaton & Smith, 1997)

$$w(r) = \frac{Pa^4}{64D}(1 - (\frac{r}{a})^2)^2 \tag{A.25}$$

where r is the deformed radius of the diaphragm, a is the original radius and D is the rigidity of the diaphragm governed by the equation:

$$D = \frac{Eh^3}{12(1 - v^2)} \tag{A.26}$$

where E,h,v are Young's modulus, thickness and Poisson's ratio of the disc (Eaton & Smith, 1997). This technique suffers from a multitude of problems namely, the diaphragm is susceptible to plastic deformation and more robust diaphragms result in more complex relationships. The current relationship is nonlinear and can result in calculation errors. Eaten (1997) advocate for the use of MEMs based electronics on these principles.

Piezoresistive sensors

Piezoresistive sensors are electric devices constructed out of a semiconductor whose electrical properties change when a stress is applied (Eaton & Smith, 1997). these devices are mounted to a diaphragm and exhibit a linear change in resistance with a change in Pressure. Currently, these sensors take the form of single-crystal diaphragms with piezoelectric resistors diffused through the materials. The advantage of these devices is robustness towards hysteresis and measurement drift. At low temperatures, silicon exhibits near-perfect elastic behaviour and is 3 times the tensile strength of strain gauges(Eaton & Smith, 1997). The sensors are, however susceptible to thermal expansion and can exhibit significant temperature drift (Samaun et al., 1971). Additionally, these sensors require resistors with identical temperature Resistance characteristics otherwise the measurements will be inaccurate. Finally, additional compensation techniques are required.

Capacitive sensors

These sensors consist of parallel conductive plates. Assuming a constant, known dielectric, an external pressure causes the plates to deform which changes the capacitance C according to the relationship (Eaton & Smith, 1997)

$$C = \int\int \frac{\epsilon}{d - w(r)} dr d\theta \tag{A.27}$$

where $w(r)$ is the deformation of the plate, ϵ is the strain experienced on the plate and d is the distance of separation. The Pressure capacitance relationship can be approximated using a least-squares fit (Eaton & Smith, 1997) however this results in model errors of 1.5% and up to 11% at $w = \frac{1}{2}h$ the height of the plate. These sensors are more advantageous over piezoresistive sensors as they have higher pressure sensitivity and reduced susceptibility to temperature drift. However, these sensors are significantly susceptible to parasitic capacitance which can result in losses and errors. Additionally, these sensors are simple in design however they tend towards more complex circuit requirements.

Appendix B

Project Design

B.1 Stakeholder analysis

For this project, a stakeholder is defined as any user or set of users who will impact the overall project or be impacted by the final design of the project (Varvasovszky & Brugha, 2000). Therefore, the stakeholders for this project can be considered as any individual directly involved in the designing/building of the project or a user: i.e. an individual responsible for using the system or any data it generates. The approach was to first identify the key stakeholders of the project and identify their role and involvement. Information was obtained from face to face meetings with the stakeholders which was used to generate the table shown below.

Table B.1: Table showing the key stakeholders in the project, their level of involvement as well as their interests in the project

Stakeholder	Function	Involvement
Lead Scientist	Principal stakeholder: Initiates and funds the SHARC buoy project	Sets the user requirements, provides feedback on progress, organises expeditions.
Project Supervisor	Set the project timeline and provide feedback on progress.	Primary engagement with principle Stakeholder
Project Engineer	Translate specifications to subsystems.	Selecting hardware, sourcing materials as well as designing firmware for the buoy.
Deployment Team	Place the system in a selected location and ensure the device is communicating	Physical handling of the device, understanding how the system works.
User	Collect and archive data packets from the buoy	Interact with the data portal and decompression software.
Collaborators	Work with users on interpreting data from the system	Analysing generated data sets.

B.2 Acceptance test protocols

Table B.2: Acceptance test for subsystem connectivity testing

AT001	**Connection test**
Evaluation type:	Software unit test
Target:	Sensors
Test protocol:	microcontroller should be connected to the device on a specified communication port.The microcontroller then requests an acknowledgment from the device either by reading the id register or by asking the device to return an acknowledgment string.
Pass Condition	• microontroller receives acknowledgment • ID register read and valid
Fail Condition:	• Incorrect ID register value returned • NACK Returned • Invalid message string (timing error or framing error) • No data received (receiver timeout - malfunctioning device) • Failure to request read (transmission timeout - No device available)

Table B.3: Acceptance test for fault testing.

AT002	**Fault testing**
Evaluation Type:	System Recovery
Target:	Hardware subsystems
Test Protocol:	Connect Subsystem to a micro-controller and run Acceptance Test AT001 under the following circumstances • **Nack Test:** Change Acknowledgement string (USART Peripheral) or device ID (SPI/I2C) to an incorrect value. • **Corrupted Message Response Test:** modify the baud rate to produce a corrupted message. • **Disconnection Test:** Set the system to run a continuous cycle. Unplug the device while the system is running. Evaluate return status.
Expected Response	**Nack Test:** Controlled Exit and return "NACK_ERROR". System clears message buffer and retries.
	Corrupted Message: Controlled Exit return "MESSAGE_ERROR". System re-initialises communication peripheral with different baud rate and retries.
	Disconnection Test: Communication Timeout, controlled exit + return "TX_ERROR". Critical Failure: system recognises that device is missing and continues routine without it.
Pass Condition:	• Device returns status and handles faults in a predicted manner • Critical Failures handled without errors
Fail Condition:	• Device freezes during test • Device returns incorrect status • Segment Faults • Hard faults • Software Rest occurs during test

Table B.4: Acceptance Test for component selection

AT003	**Specification Test**
Evaluation Type:	Analytical
Target:	Hardware components
Test Protocol:	Evaluate Specifications of the components from the data sheet to determine if the specifications meet the requirements for the system
Pass Condition	• Specifications meet the desired requirements
Fail Condition:	• Specifications do not meet the requirement

Table B.5: Acceptance Test for Subsystem Robustness Testing

AT004	**Subsystem Robustness Test**
Evaluation Type:	Software
Target:	System, subsystem
Test Protocol:	Connect Subsystem to microcontroller and run a preset routine covering the following cycle • Intialisation • function • Deinitialisation Run this cycle 100 times consecutively.
Pass Condition	• Microcontroller sccessfully completes consecutive cycles
Fail Condition:	• failure to complete more than 1 consecutive cycle • failure to initialise (fails acceptance Test AT001) • failure to correctly deinitialise after completing routine • Subsystem does not restart the cycle when reset

Table B.6: Acceptance Test for accelerated system testing

AT005	**Accelerated System Test**
Evaluation Type:	Software
Target:	System
Test Protocol:	System to run firmware with all sensors initialised. Routine loaded on system that cycles between all the sensors and communication modules turning them on and off then cycling through deep sleep mode. This occurs over a 1 hour period
Pass Condition	• System successfully cycles through sensors with no timing delays • System completes an hour of accelerated testing with no intervention • Power Reset do not cause the device to lock up or malfunction
Fail Condition:	• System freezes at any point during the test • System unable to turn on any sensro • system unable to enter sleep mode • system encounters unexpected reset • system unable to run for an hour

Table B.7: Acceptance Test for Subsystem Calibration Testing

AT006	**Calibration Test**
Evaluation Type:	Statistical
Target:	Sensor Measurements
Test Protocol:	Connect Device to a data logger and set the measurand to a static value Record 100 sample points from the Device under test at a fixed frequency for a set amount of time. Measure against an accurate reference. Calculate mean and average value from data set and ensure it falls within the parameters given by the datasheet.Determine the disagreement between the average recorded value and average measured value and take the difference as the fixed offset bias. Repeat the Test twice more first by adjusting the value half through recording then by varying the value at a fixed rate
Pass Condition	• Calibration produces a consistent output well within the accepted error range when measured against a reference • Step testing bring the measured value to the correct value • device is capable of measuring over the specified range
Fail Condition:	• Test does not produce a predictable. consistent offset • Calibration values produces an invalid dataset • Device under Test fails at any point. • Calibrated Data set unable to replicate the measurand

Table B.8: Acceptance Test for Power Test

AT007	**Power System Test**
Evaluation Type:	Hardware
Target:	Power System
Test Protocol:	Connect the Power system to a Load of a known resistance. Connect an Ammeter and a Voltmeter respectively in series and in parallel. Measure the Current and Supply voltage at a fixed rate for 1 hour. Record the Battery Voltage before the Test and After the Test Then decrease the load to increase the current and Run until the Battery Voltage drops Below the Threshold for the Regulator. Measure the Output current and Supply Voltage.
Pass Condition	• Device cycles through routines for set period of time without failure • Device survives for specified period of time • Recorded values do not exceed the specs given from the datasheet of the components
Fail Condition:	• Power System depleted before test has finished • Device fails to perform routine at any point during the test • Mechanical/ Electrical failure occurs during test.

Table B.9: Acceptance Test for Low Temperature Test

AT008	**Low Temperature Tests**
Evaluation Type:	Hardware Robustness
Target:	Subsystem and full system
Test Protocol:	Connect subsystem to a datalogger and place in freezer. Set the freezer to $-20°C$ and run the system through an accelerated subsystem test as per AT003. Then take the device out the freezer and wait for it to thaw. Then run another accelerated subsystem test. Finally connect all subsystems together and place in enclosure. Put device in the freezer and run an accelerated system Test as per AT004. Repeat in Room Temperature Conditions
Pass Condition	• System completes routine cycles in both sub zero and room temperature environment • Subsystem Passes AT003 in $-20°C$ and Room Temperature
Fail Condition:	• Incorrect ID register value returned (SPI or I2C Address Incorrect) • Subsystem Fails AT003 in sub-zero and room temperature environment available • System fails AT004 in sub-zero and room temperature environment

Table B.10: Acceptance Test for final system deployment test.

AT009	**Deployment Test**
Evaluation Type:	Performance
Target:	Full System
Test Protocol:	Only to be performed once requirements for all other tests have been met. Ensure device is calibrated before hand and in a deployable state. Ensure power is turned on and sensors have been initialised. Deploy the system in a desired location and monitor the transmitted packages.
Pass Condition	• System acknowledges Deployment and routinely transmits full packets of data. • System survives for 1 month or longer
Fail Condition:	• No acknowledgement received • No packets received • Empty data received Failure within the first half an hour of deployment should result in immediate retrieval of the device.

B.3 Schematics and renders

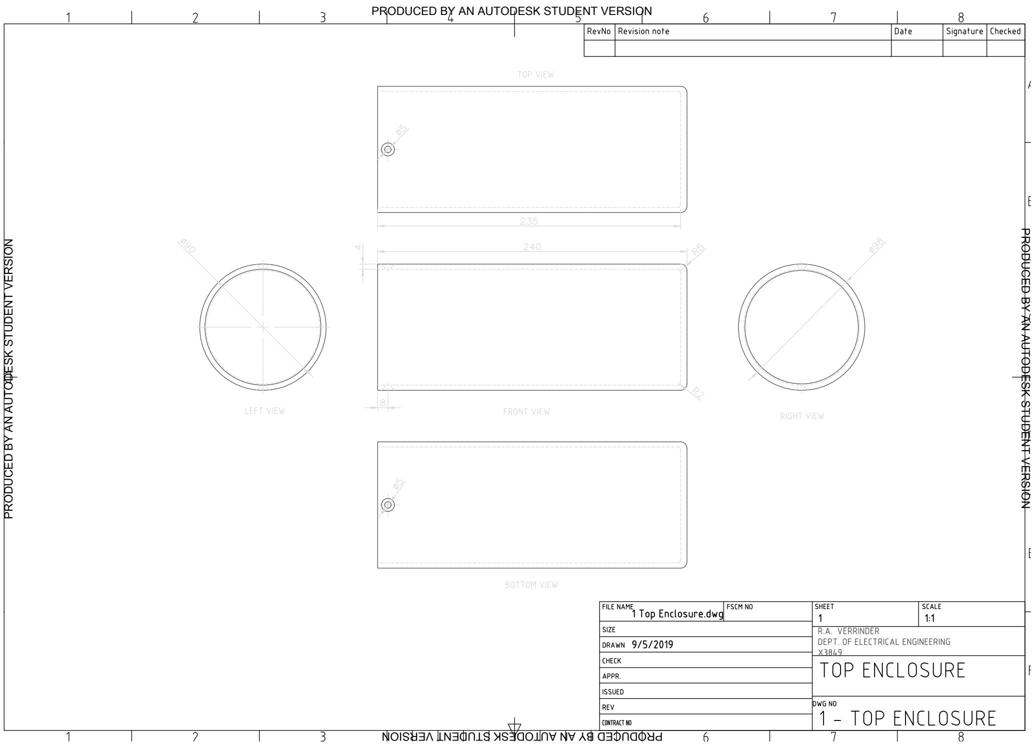

Figure B.1: Schematic of top enclosure which protects the electronics

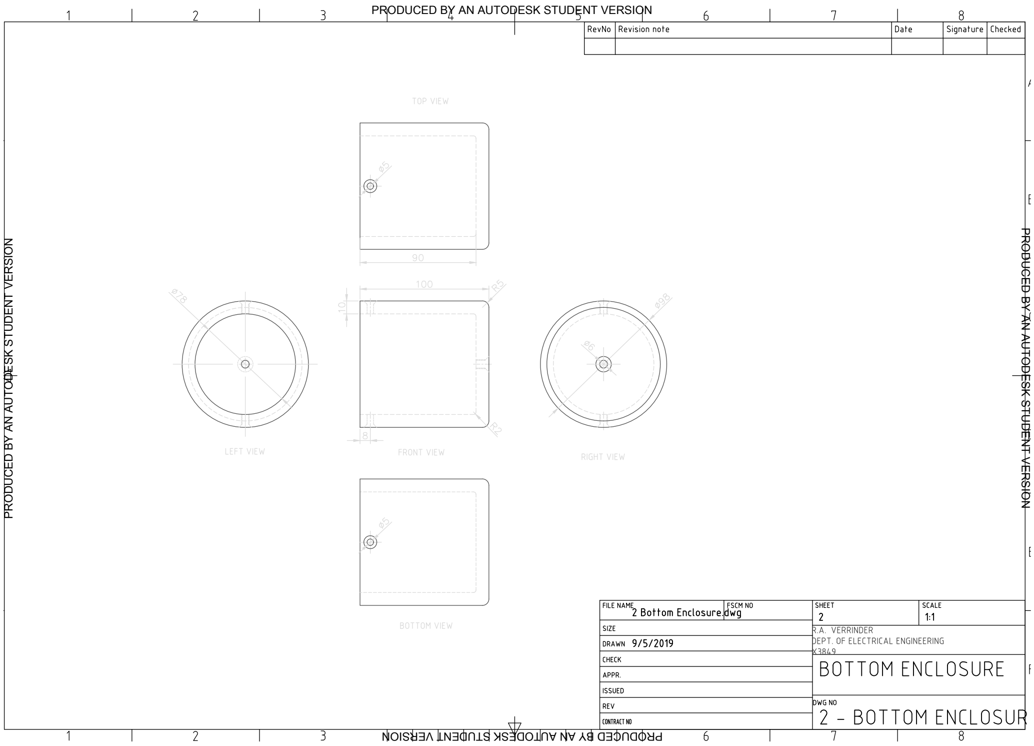

Figure B.2: Schematic of bottom enclosure for the batteries and power system.

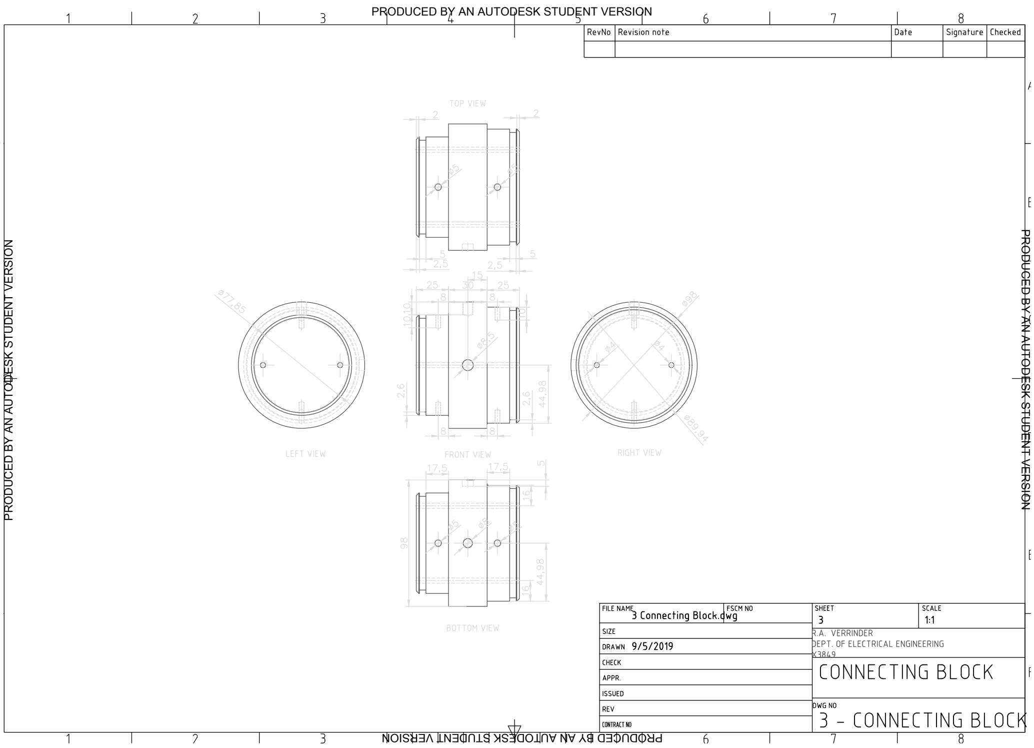

Figure B.3: Schematic of the connector block which provides a base for the electronics to be mounted on.

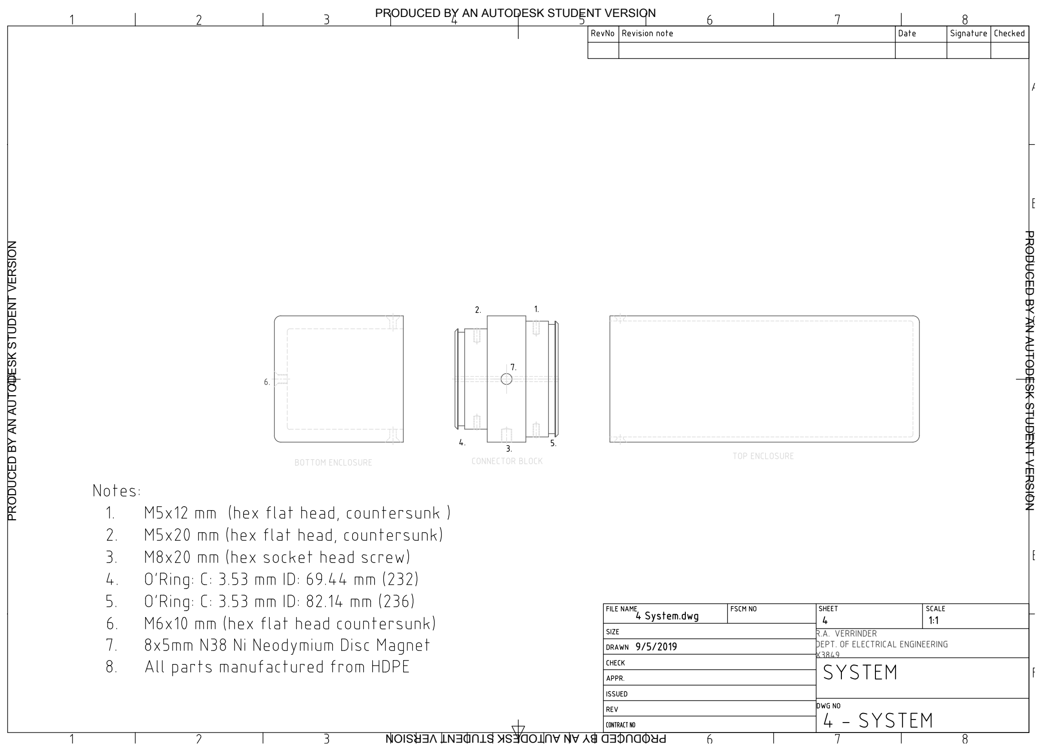

Figure B.4: Full enclosure schematic.

Appendix C

Software design

C.1 Events and interrupt handling protocols

Table C.1: Description of Interrupt generated by the iridium module on an external digital input line.

Ring Indicator	
Entry Condition	Buoy In any state other than reset with GPIO mapped to EXTI, with wake up from sleep mode. The WUP Pin receives a Digital High from Ring Indicator Pin on Iridium
Function	The user has transmitted a packet to the buoy. Download the packet and execute/store the data based on the packet structure
Exit Condition	Device has downloaded user data which has been used to update the system and store data.
Return State	If entry source was a wake up, device will return to sleep. Otherwise device will return to the main loop.

Table C.2: Description of routine for interrupts generated by the IMU on an external digital input line.

IMU Event Detection	
Entry Condition	Buoy In any state other than reset with GPIO wake up pin mapped to EXTI, with wake up from sleep mode. The WUP Pin receives a Digital High from Interrupt pin
Function	Device reads the interrupt source from the IMU, initializes I2C peripheral and begins sampling IMU data. Interrupt source determines the sampling rate, period and mode
Exit Condition	Device will exit when the IMU has finished sampling and the data has been stored into memory.
Return State	If entry source was a wake up, device will return to sleep. Otherwise device will return to the main loop.

Table C.3: Description of event handling routine for a brown out recovery event.

Brown out Detection	
Entry Condition	Buoy is in run mode or in Standby mode with Brown out detection voltage enabled. $V_{brownout}$ has been configured in option bytes. Event occurs when the voltage supplied to the microcontroller is less than $V_{brownout}$ causing the device to be held under reset. When the Voltage rises above the threshold, the device will enter the handler
Function	Device resets the relevant register flags and checks for data corruption. If no data is corrupted. Device will reload the last state and attempt to run it again. Otherwise the device performs a software reset
Exit Condition	$V_{supply} > V_{brownout}$, device successfully executes code in handler
Return State	Returns to main loop

Table C.4: Description of routine for handling low power events.

Low Power Detection	
Entry Condition	Device is in run or sleep, Power Voltage thresholds set in PWR and interrupt enabled. Event occurs when $V_{supply} < V_{power}$ generating an event interrupt.
Function	Device will read INA sensor and transmit final packet to base. All peripherals switched off, Device placed into shut down mode.
Exit Condition	No Exit
Return State	No return state

Table C.5: Description of routine for handling a software reset event.

Software Reset	
Entry Condition	The Microcontrollers NRST internal line is pulled low for a few seconds. This is triggered in any state by triggering a software reset in the NVIC
Function	Reset the buoy to an initial state. Clear any pending flags. Reset data in back up registers
Exit Condition	Successful reset of voltage domains
Return State	Return to Reset state and start of main loop

C.2 Initialization Routines

Table C.6: Color guide for the initialization routine flow diagrams.

Microcontroller (HAL) function
Sensor (API) function
Function return statement evaluation
Fail return status
Success return status

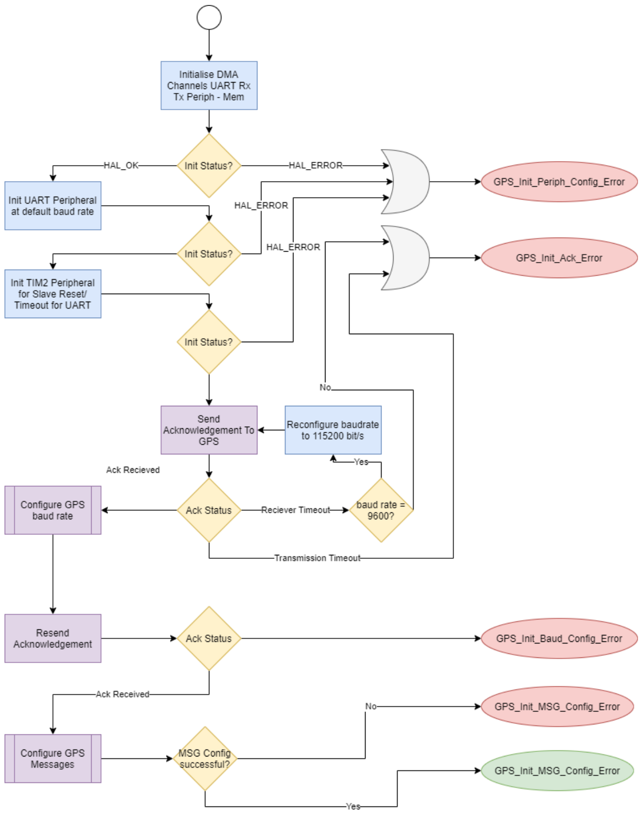

Figure C.1: Ublox Neo 7-m initialisation routine

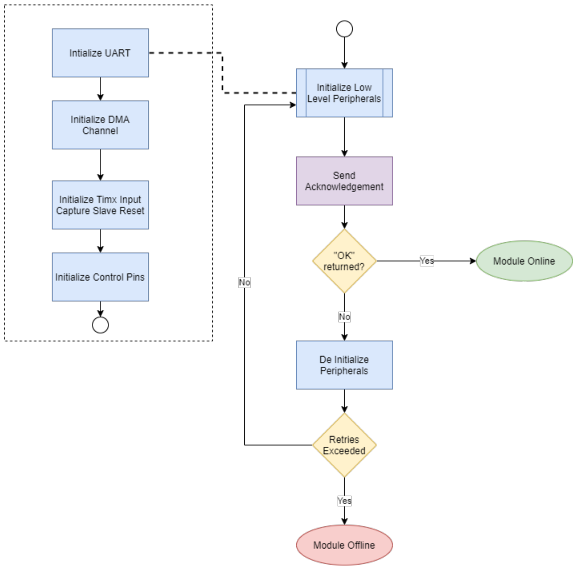

Figure C.2: Rockblock 9603 initialisation routine

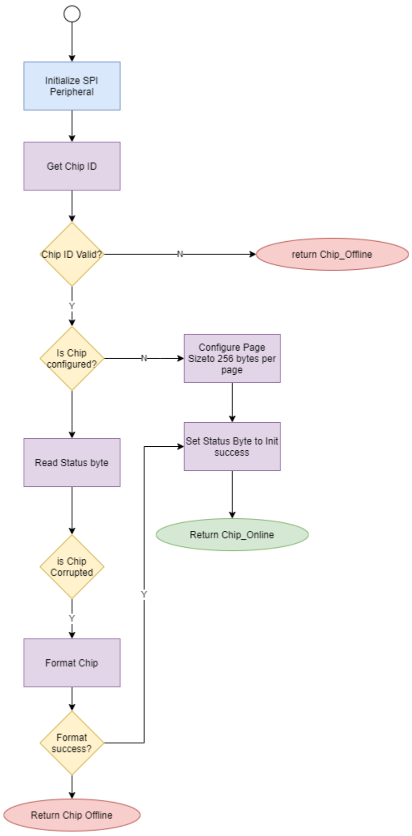

Figure C.3: AT45DB641E initialisation routine

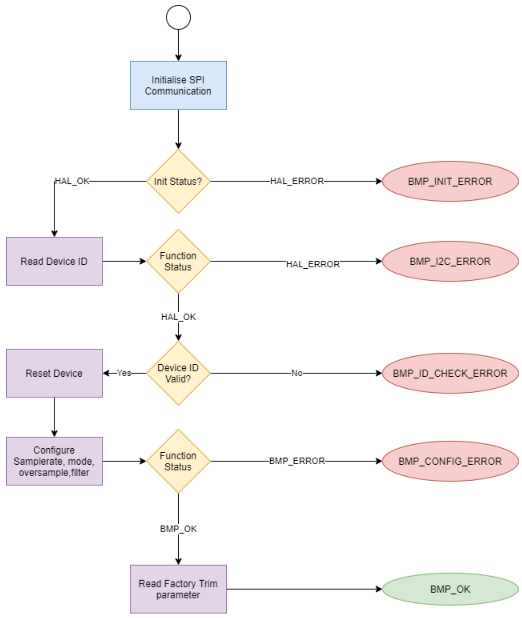

Figure C.4: BMP280 initialisation routine

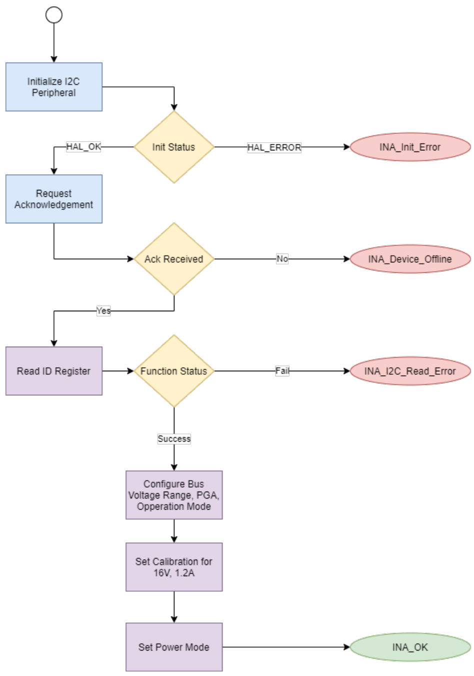

Figure C.5: INA219 initialisation routine

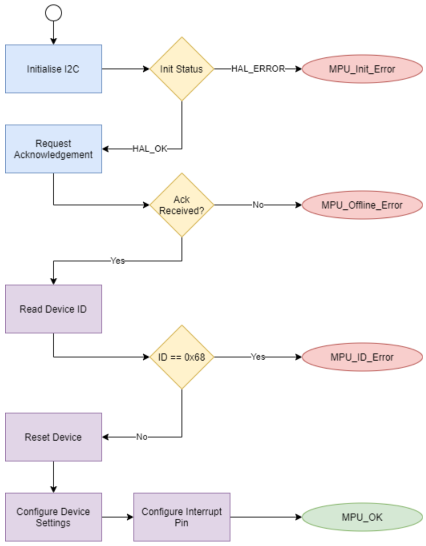

Figure C.6: MPU6050 initialization routine

C.3 Code

C.3.1 BMP280 Temperature compensation formula

```
/*
 * @brief Temperature Compensation algorithm
 *
 * @param T_val
 * @param t_fine
 * @param bmp_trim
 *
 * @retval int32_t
 */
int32_t BMP280_Compensate_Temp(int32_t T_val,int32_t* t_fine,
   BMP280_trim_t bmp_trim)
{
  //compensate Temperature from datasheet
  int32_t var1 = (((T_val>>3)-
     ((int32_t)bmp_trim.dig_T1<<1))*((int32_t)bmp_trim.dig_T2))>>11;
  int32_t var2 = (((((T_val>>4) - ((int32_t)bmp_trim.dig_T1)) *
     ((T_val>>4) - ((int32_t)bmp_trim.dig_T1))) >>
     12)*((int32_t)bmp_trim.dig_T3)) >> 14;
  int32_t temp = var1+var2; //for storage in global variable
  *t_fine = temp;
  return (temp*5 +128)/256;
}
```

Figure C.7: Function written to compensate a 32 bit Temperature reading for sensor irregularities using the 32 bit version of the recommended compensation formula from the datasheet (Bosch Sensortech, 2018). The formula uses the compensation parameters stored on the sensor

```
/*
 * @brief Pressure compensation formula
 *
 * @param P_val
 * @param t_fine
 * @param bmp_trim
 *
 * @retval uint32_t
 */
uint32_t BMP280_Compensate_Pressure(uint32_t P_val,int32_t
   t_fine,BMP280_trim_t bmp_trim)
{
  //Compensation formula
  int32_t var1 = (int64_t)t_fine - 128000;
  int64_t var2 = var1*var1*((int64_t)(bmp_trim.dig_P6));
  var2 = var2 + (((int64_t)bmp_trim.dig_P4)<<35);
  var1 = ((var1 * var1 * (int64_t)bmp_trim.dig_P3)>>8) + ((var1 *
     (int64_t)bmp_trim.dig_P2)<<12);
  var1 = (((((int64_t)1)<<47)+var1))*((int64_t)bmp_trim.dig_P1)>>33;
  //check for divide by 0 error
  if(var1 == 0)return 0;
  int64_t P = 1048576 - (int32_t)P_val;
  P = (((P<<31)-var2)*3125)/var1;
  var1 = (((int64_t)(bmp_trim.dig_P9)) * (P>>13) * (P>>13)) >> 25;
  var2 = (((int64_t)(bmp_trim.dig_P8)) * P) >> 19;
  P = ((P + var1 + var2) >> 8) + (((int64_t)(bmp_trim.dig_P7))<<4);
  return (uint32_t)P;
}
```

Figure C.8: Function written to compensate a 32 bit pressure reading for sensor irregularities using the 32 bit version of the recommended compensation formula from the datasheet (Bosch Sensortech, 2018). The formula uses the compensation parameters stored on the sensor

C.3.2 INA219 Calibration Algorithm

```
/*
 * Function Name INA_Status_t INA219_Calibrate_16V_1_2A(float
    *I_MBO, float *V_MBO, float *P_Max)
 * @brief: The following function writes a 16 bit value to the
    calibration register which
 *       is used to adjust the current, bias voltage and power.
    Here, A LSB value is
 *       calculated based on the user requirements and selected
    from a range. It would
 *       be advisable to calculate the value manually and replace
    it in the function below
 *       please note: the following function has values calculated
    manually. These can be
```

```
 *       changed based on the configuration settings.
 *       The values are calculated for 16V bus voltage range with a
    2A expected current and
 *       a 160mV shunt voltage range
 *
 *   Step 1: V_Bus_Max = 16V
 *       V_Shunt_Max = 160mV
 *       R_Shunt = 0.1 Ohm
 *
 *   Step 2: Max Possible I = 1.6A
 *
 *   Step 3: Let I Max Expected = 1.2A
 *
 *   Step 4: Min LSB = 36.6 uA/LSB
 *       Max LSB = 292.97 uA
 *
 *       Choose LSB = 100 uA
 *   Step 5: Set Calibration value = 4096
 */

INA_Status_t INA219_Calibrate_16V_1_2A(float *I_MBO, float *V_MBO,
   float *P_Max)
{
  //set Current Step Size
  ina.INA219_I_LSB = 100.0/1000000.0;
  uint16_t I_cal_val =
     (uint16_t)(0.04096/(ina.INA219_I_LSB*INA219_R_SHUNT));
  ina.INA219_P_LSB = 20*ina.INA219_I_LSB;
  float I_max = ina.INA219_I_LSB*32767;
  if(I_max > 1.6) //max possible current
  {
    *I_MBO = 1.6;
  }else
  {
    *I_MBO = I_max;
  }
  float Vshunt_max = *I_MBO*INA219_R_SHUNT;
  if(Vshunt_max > 0.16)
  {
    *V_MBO = 0.16;
  }
  else
  {
    *V_MBO = Vshunt_max;
  }
  *P_Max = *I_MBO*16;

  //write I_Cal_val to register
  uint8_t temp[2] = {(I_cal_val&0xFF00)>>8,(I_cal_val&0x00FF)};
  if(HAL_I2C_Mem_Write(&ina.ina_i2c,INA219_I2C_Address,CALIBRATION_REG,1,temp,2,
     != HAL_OK)
```

```
  {
    return INA_I2C_WRITE_ERROR;
  }

  return INA_OK;
}
```

Figure C.9: Calibration routine for INA219 Current sensor for a maximum current of 1.2A, maximum Bus Voltage of 16V and maximum shunt voltage of 160mV

C.3.3 Data Structs

```
/*
 * Coordinate Object
 *
 * Stores the Cordinates of GPS in the form DDMM.mmmm
 * where
 *        DD    -  Degrees
 *        MM    -  Minutes
 *        mmmm  -  Fractional minutes
 * Variables:
    Name.............Type..............................Description
 *
    lat..............float32_t..........................GPS
    Lattitude
 *
    longi............float32_t..........................GPS
    Longitude
 */
typedef struct
{
  float_t lat;
  float_t longi;
}Coord_t;
```

Figure C.10: Coord_t Data structure to store incoming GPS coordinates as IEEE754 32-bit floats

```
/*
 * Diagnostic Object
 *
 * Structure to Hold the GPS data signal diagnostics
 *
 * Variables:
   Name............Type...............................Description
 *
   PDOP............DOP_t..............................Positional
   Dilation of Precision (3D)
 *
   HDOP............DOP_t..............................Horizontal
   Dilation of Precision
 *
   VDOP............DOP_t..............................Vertical
   Dilation of Precision
 *
   num_sats.........uint8_t............................Number of
   Satelites used to obtain positional Fix
 *
   fix_type.........uint8_t............................number
   between 1-3 describing the type of fix obtained
 *
 * Fix types
 * 1 - No Fix
 * 2 - 2D Fix (No altitude)
 * 3 - 3D Fix
 */

typedef struct
{
  DOP_t PDOP;
  DOP_t HDOP;
  DOP_t VDOP;
  uint8_t num_sats;
  uint8_t fix_type;
}Diagnostic_t;
```

Figure C.11: Data Structure for storing GPS signal diagnostic information

Appendix D

Supplementary Tables

Table D.1: List of data services provided by Iridium for transmission of data over the satellite network including the bandwidth and purpose of the service taken from (Iridium Satellite Communications, 2016)

Service Name	**Purpose**	**Supporting Modems**	**Bandwidth**
Short Burst Data (SBD)	Sending short messages in bursts.	• 9603/9602 • Iridium Edge • 9523	• 340 bytes upload & 270 bytes download • 1960 bytes upload & 1890 bytes download
Router-based Unrestricted Digital Interworking Connectivity Solution (RUDICS)	Continuous transfer of large real-time data from a large array of devices to a host.	• 9523 • 9522B (*depreciated*)	• 6 – 10 Kbytes/min
Circuit Switch Data (CSD)	Continuous transmission of large volumes of data over a dial-Up network using a SIM Card.	• 9523 • 9522B (*depreciated*)	• 6 – 10 Kbytes/min

Table D.2: Strategies used by the devices to transfer data from remote locations. Table includes transmission technologies and services used as well and transmission strategies and transmission intervals where given. Prices are converted to Rands (R) via (Oanda Corporation, 2021).

Device Name	**Service**	**Modem**	**Bandwidth**	**Transmission Strategy**
WIIB	Iridium SBD	9602	340 bytes	Data condensed into one 340 byte packet. (transmission intervals unavailable)
WIIOS	Iridium SBD	9602	340 bytes	Data condensed into one 340 byte packet transmitted every 5 hours.
NDWB	Iridium RUDICS	9522B	6 - 10 Kybtes/min	raw inertial sample points transmitted every minute
SKIB	Iridium SBD (long range) ZigBee (short range)	• 9602 • Xbee Pro	• 340 bytes • 50 Kbps	• GPS data transmitted every 10 minutes. • Raw data transmitted when host is in range.
SWIFT	Iridium Ethernet	Iridium: Geoforce SmartOne (tracking) Unspecified SBD Modem (telemetry) Ethernet: Digi Xpress ethernet bridge	Iridium: N/A 1960 Ethernet: 935 kb/s	Data transmitted through SBD modem. variable packet sizes ranging from 4 - 1228 bytes in length

SIMB	Iridium or ARGOS	9603	340	single packet transmission of 275 bytes
Polar ISVP	Iridium	9602	340 bytes	User configured packet sizes and transmission intervals
Trident	Iridium	9603	340 bytes	single packet transmission of 16 bytes

Appendix E

Test Protocols

E.1 Unit Tests

Table E.1: Unit Test 1: Hardware Verification test outlining procedure, test cases and relation to acceptance tests

Unit Test 1:	Hardware Verification
Input:	1. Hardware Module 2. Function Pointer to hardware module's initialization function
Output:	Return Status
Tasks:	1. Connect Sensor to micro-controller 2. Supply system with power 3. run test protocol AT001 4. exit upon reception of return status
Test Case:	1. Sensor Connected and Powered on - AT001 2. Nack Test - AT002 3. Sensor Disconnected - AT002

Table E.2: Unit Test 2: GPS Connection Test test outlining procedure, test cases and relation to acceptance tests

Unit Test 2:	GPS connection test
Input:	None
Output:	GPS Serial Output
Tasks:	1. Connect GPS to external Power 2. place system in open environment free of obstructions 3. set timeout to 5 minutes 4. wait for device to lock on to a gps signal 5. evaluate return status
Test Case:	1. Open field, no obstructions - signal acquisition 2. Open Field, Partial obstructions - slow signal acquisition 3. Open Field, Full Obstructions - no signal acquisition 4. Indoors, Partial Obstruction - slow signal acquisition 5. Indoors, Full Obstructions - no signal acquisition

Table E.3: Unit Test 3: GPS Data Validity Test test outlining procedure, test cases and relation to acceptance tests

Unit Test 3:	GPS Data Validity Test
Input:	NMEA Message String
Output:	Evaluation Result
Tasks:	1. Compare input packet structure to NMEA standard 2. Compare packet address to accepted message strings and talker IDs 3. Calculate checksum and compare to transmitted checksum byte
Test Case:	1. Valid GSA message string 2. Valid GLL message string 3. Valid ZDA message string 4. Valid NMEA message with unrecognised address 5. Valid NMEA message with invalid checksum 6. Invalid message structure, 7. Null String

Table E.4: Unit Test 4: Memory Verification test procedure, test cases and relation to acceptance tests

Unit Test 4:	Memory Module Validity Test
Input:	None
Output:	Return Status
Tasks:	1. Connect To Memory Module 2. Verify Read Operation 3. Verify Write Operation 4. Verify Delete opperation
Test Case:	1. byte 2. Page of ordered Data 3. Page of Un-ordered Data 4. random length of data

Table E.5: Unit Test 5: Power Module Verification test outlining procedure, test cases and relation to acceptance tests

Unit Test 5:	Power Module Verification Test
Input:	Power Source Of Known Voltage
Output:	Output Voltage
Tasks:	1. Connected Power Module to a variable input source 2. Connect voltmeter 3. Set Voltage to a known value and measure the output 4. The Output value should be 5V for $5V < V_{SS} < V_{max}$
Test Case:	1. 5V Input - 5V output 2. 7.2V Input - 5V output 3. 0V Input - 0V output 4. 4.2V - 4.2V output

Table E.6: Unit Test 6: Transmission test test outlining procedure, test cases and relation to acceptance tests

Unit Test 6:	Iridium Transmission Test
Input:	message buffer
Output:	Transmission status
Tasks:	1. upload a message of known size to the module 2. Initiate a Transmission 3. evaluate return status
Test Case:	1. null message 2. 1 byte message 3. 50 byte message 4. 120 byte message 5. 340 byte message 6. binary message 7. ascii message

Table E.7: Unit Test 7: Temperature Verification test test outlining procedure, test cases and relation to acceptance tests

Unit Test 7:	Environmental Sensor Temperature Validation Test
Input:	Ambient Temperature
Output:	Sensor Temperature Value
Tasks:	1. place sensor in an environment where the temperature is known 2. Measure Ambient Temperature ADC value and read from sensor 3. perform temperature compensation 4. compare value to external measurement
Test Case:	1. $\pm 25°$ (Standard Temperature and Pressure) 2. $10°$ (Cold Test) 3. $0°$ (Sub Zero Test) 4. $-20°$ (Extreme Freeze Test)

Table E.8: Unit Test 8: Inertial Measurement Unit test outlining procedure, test cases and relation to acceptance tests

Unit Test 8:	Inertial Measurement Unit Validation Test
Input:	None
Output:	Test return status
Tasks:	1. perform Self-Test, verify self test values within 14% of the factory set value 2. enable all axes and read data 3. enable interrupt pin and test response in Interrupt handler 4. set device to sleep, wake up and take a reading
Test Case:	1. Device Connected 2. Device Disconnected 3. Device at Rest 4. Device in motion

E.2 System Tests

Table E.9: Results of subsystem acceptance tests for each of the identified modules. Modules that were successfully validated were marked with a ✓, failed tests were marked by an X and tests that could not be applied to a subsystem were marked by an N/A

	AT001	**AT002**	**AT003**	**AT004**	**AT005**
GPS	✓	✓	✓	✓	✓
Iridium Modem	✓	✓	✓	✓	✓
Flash Chips	✓	✓	✓	✓	✓
Power Module	N/A	N/A	✓	N/A	N/A
Env Sensor	✓	✓	✓	✓	✓
Power Monitor	✓	✓	✓	✓	✓
IMU	✓	✓	✓	✓	✓

Appendix F

Test results

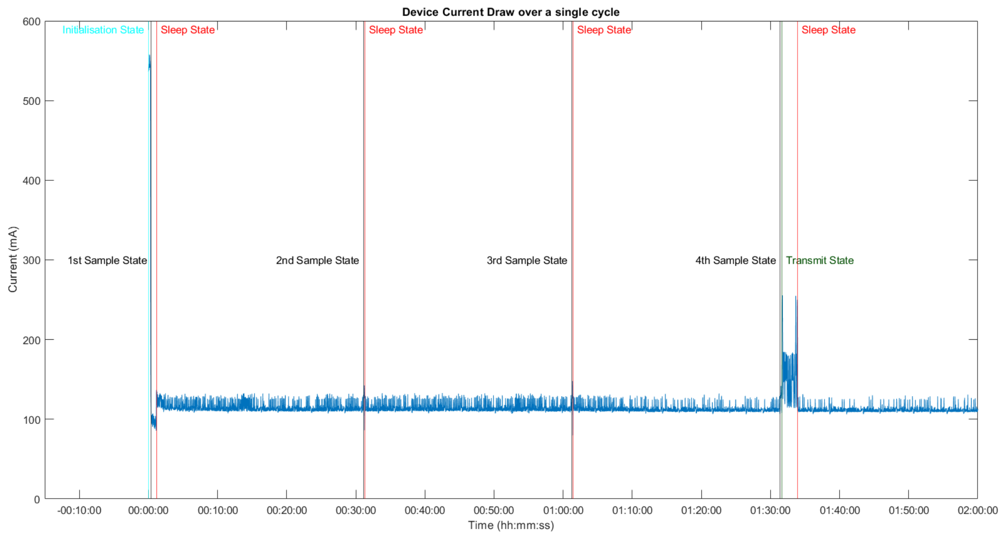

Figure F.1: Graph showing a typical current cycle of the buoy during the various phases. Data was sampled at 1Hz with all modules connected, sample intervals set to 30 mins the INA219 sensor connected to an external data logger and the device placed in a partially obstructed environment.

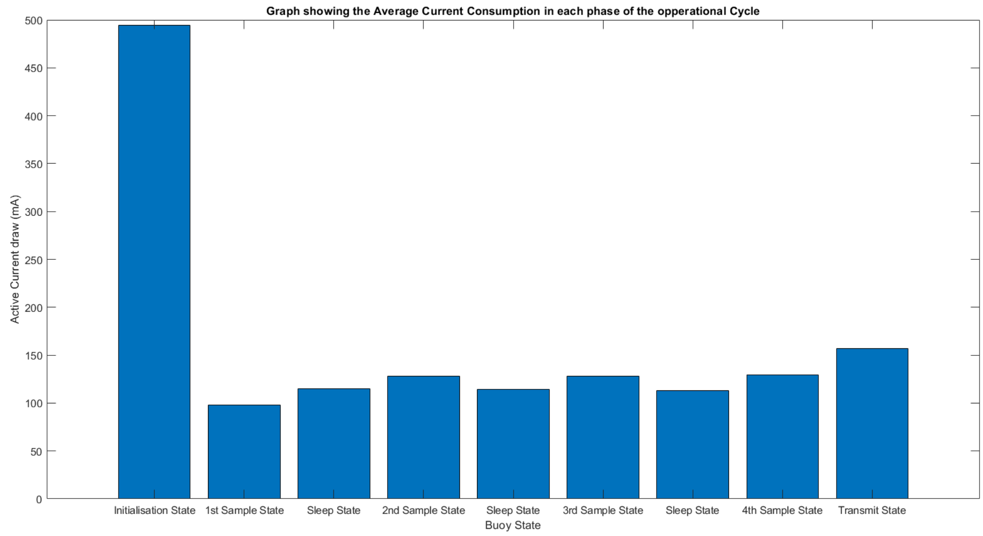

Figure F.2: Average Current consumption at each phase in the life-cycle of the buoy. Ordered chronologically

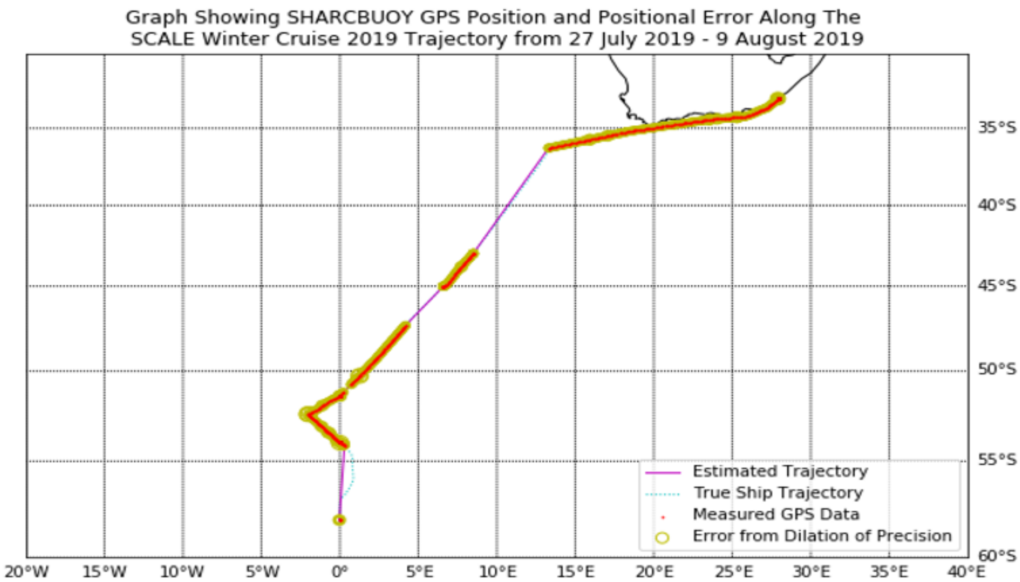

Figure F.3: The GPS trajectory of the Aghulus 2 ship from the Marginal Ice Zone to East London. The plot shows the estimated position (magenta) taken from the buoy samples (red) compared to the actual trajectory (cyan). The positional error (PDOP) of each measurement is shown as an exaggerated area around the measured position

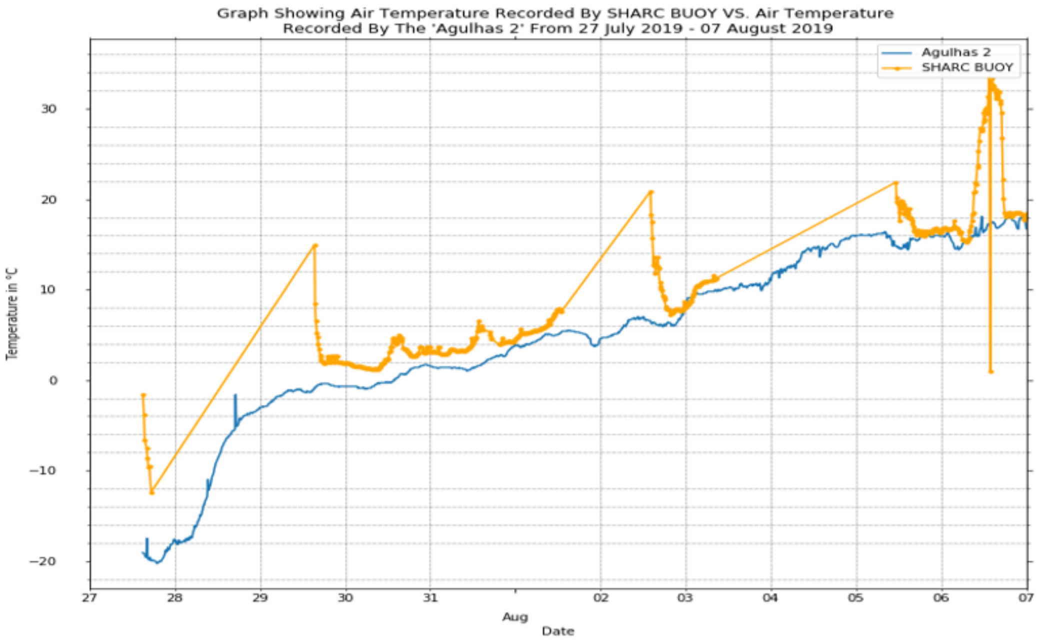

Figure F.4: Air Temperature recorded by the buoy (yellow) over 11 days compared to the air temperature recorded by the ship (blue)

Bibliography

Ackley, S. F., Stammerjohn, S., Maksym, T., Smith, M., Cassano, J., Guest, P., Tison, J.-L., Delille, B., Loose, B., Sedwick, P., & et al. (2020). Sea-ice production and air/ice/ocean/biogeochemistry interactions in the Ross Sea during the PIPERS 2017 autumn field campaign. *Annals of Glaciology*, *61*(82), 181–195.

Adafrut. (2014, April 8). *Ultimate gps module - 66 channel w/10 hz updates - mtk3339 chipset*. [Online]. Available at https://www.adafruit.com/product/790 (Accessed February 25, 2021)

Ahmad, N., Ghazilla, R. A. R., Khairi, N. M., & Kasi, V. (2013). Reviews on various inertial measurement unit (imu) sensor applications. *International Journal of Signal Processing Systems*, *1*(2), 256–262.

Alberello, A., Bennetts, L., Heil, P., Eayrs, C., Vichi, M., MacHutchon, K., Onorato, M., & Toffoli, A. (2019). Drift of pancake ice floes in the winter Antarctic marginal ice zone during polar cyclones. *arXiv preprint arXiv:1906.10839*.

Alberello, A., Bennetts, L., Heil, P., Eayrs, C., Vichi, M., MacHutchon, K., Onorato, M., & Toffoli, A. (2020). Drift of pancake ice floes in the winter Antarctic Marginal Ice Zone during polar cyclones. *Journal of Geophysical Research: Oceans*, *125*(3), e2019JC015418.

Al-Zareer, M., Dincer, I., & Rosen, M. A. (2018). A review of novel thermal management systems for batteries. *International Journal of Energy Research*, *42*(10), 3182–3205.

Arrigo, K. R., & Thomas, D. N. (2004). Large scale importance of sea ice biology in the Southern Ocean. *Antarctic Science*, *16*(4), 471–486.

Barber, D. G. (2005). Microwave remote sensing, sea ice and Arctic climate. *La Physique au Canada*, *61*, 105–111.

Barber, N. F., & Ursell, F. (1948). The generation and propagation of ocean waves and swell. I. Wave periods and velocities. *Philosophical Transactions of the Royal Society of London. Series A, Mathematical and Physical Sciences*, *240*(824), 527–560.

Besenhard, J. O. (2008). *Handbook of battery materials*. John Wiley & Sons.

Bishop, G., & Klobuchar, J. (1990). Ranging errors due to disturbances in the polar ionosphere. *Proceedings of the 3rd International Technical Meeting of the Satellite Division of The Institute of Navigation (ION GPS 1990)*, 175–179.

Bonvoisin, J., Mies, R., Boujut, J.-F., & Stark, R. (2017). What is the "source" of open source hardware? *Journal of Open Hardware*, *1*(1), 1–18.

Bosch Sensortec. (2021). *Out of the box sensor support*. [Online]. Available at https://www.bosch-sensortec.com/products/environmental-sensors/humidity-sensors-bme280/ (Accessed February 26, 2021)

Bosch Sensortech. (2018). *Bmp280 - digital pressure sensor* [Rev. 1.19]. [Online]. Available at https://www.bosch-sensortec.com/media/boschsensortec/downloads/datasheets/bst-bmp280-ds001.pdf

Bruncin. (2021). *IMB digital temperature chain.* [Online]. Available at https://www.bruncin.com/products/temperature-chain/ (Accessed February 25, 2021)

Carsey, F. D. (1992). *Glossary of ice terminology.* American Geophysical Union.

Childs, P. R., Greenwood, J., & Long, C. (2000). Review of temperature measurement. *Review of scientific instruments*, *71*(8), 2959–2978.

Coon, M. D., Maykut, G. A., & Pritchard, R. S. (1974). Modeling the pack ice as an elastic-plastic material. *AIDJEX Bulletin No. 24: Arctic ice dynamics joint experiment. Seattle: University of Washington*, 1–106.

Coon, M., Kwok, R., Levy, G., Pruis, M., Schreyer, H., & Sulsky, D. (2007). Arctic ice dynamics joint experiment (AIDJEX) assumptions revisited and found inadequate. *Journal of Geophysical Research: Oceans*, *112*(C11S90).

Crisp, J. (2003). *Introduction to microprocessors and microcontrollers.* Elsevier.

C/S2ESC - Software and Systems Engineering Standards Committee. (1996). Ieee guide for developing system requirements specifications. *IEEE Std 1233-1996*, 1–30.

C/S2ESC - Software and Systems Engineering Standards Committee. (1998). Ieee/eia guide - industry implementation of international standard ISO/IEC 12207 : 1995 (ISO/IEC 12207) - software life cycle processes - life cycle data. *IEEE/EIA 12207.1-1997*, 1–38.

De Santi, F., De Carolis, G., Olla, P., Doble, M., Cheng, S., Shen, H. H., Wadhams, P., & Thomson, J. (2018). On the ocean wave attenuation rate in grease-pancake ice, a comparison of viscous layer propagation models with field data. *Journal of Geophysical Research: Oceans*, *123*(8), 5933–5948.

DeConto, R. M., & Pollard, D. (2003). Rapid cenozoic glaciation of Antarctica induced by declining atmospheric CO 2. *Nature*, *421*(6920), 245–249.

Digikey. (2021). *Ds18b20+par.* [Online]. Available at shorturl.at/dsPS7 (Accessed February 25, 2021)

Doble, M. J., & Bidlot, J.-R. (2013). Wave buoy measurements at the Antarctic sea ice edge compared with an enhanced ECMWF WAM: Progress towards global waves-in-ice modelling. *Ocean Modelling*, *70*, 166–173.

Doble, M. J., Wilkinson, J. P., Valcic, L., Robst, J., Tait, A., Preston, M., Bidlot, J.-R., Hwang, B., Maksym, T., & Wadhams, P. (2017). Robust wavebuoys for the marginal ice zone: Experiences from a large persistent array in the Beaufort Sea. *Elementa: Science of the Anthropocene*, *5*(47).

Earle, M. D. (1996). Nondirectional and directional wave data analysis procedures. *NDBC Technical Document 96-01, John C. Stennis Space Center, Mississippi.*

Eaton, W. P., & Smith, J. H. (1997). Micromachined pressure sensors: Review and recent developments. *Smart Materials and Structures*, *6*(5), 530–539.

Emery, W., Fowler, C. W., & Maslanik, J. (1997). Satellite-derived maps of Arctic and Antarctic sea ice motion: 1988 to 1994. *Geophysical Research Letters*, *24*(8), 897–900.

Fong, W., Ong, S., & Nee, A. (2008). Methods for in-field user calibration of an inertial measurement unit without external equipment. *Measurement Science and technology*, *19*(8), 085202.

Galin, N., Worby, A., Markus, T., Leuschen, C., & Gogineni, P. (2011). Validation of airborne FMCW radar measurements of snow thickness over sea ice in Antarctica. *IEEE Transactions on Geoscience and Remote Sensing*, *50*(1), 3–12.

GIS Geography. (2020, December 26). *Gps accuracy: Hdop, pdop, gdop, multipath & the atmosphere*. [Online]. Available at https://gisgeography.com/gps-accuracy-hdop-pdop-gdop-multipath/ (Accessed February 24, 2021)

Globalstar. (2021). *Globalstar satellite technology bringing satellite communications and tracking to you*. Globalstar. [Online]. Available at https://www.globalstar.com/en-za/ (Accessed February 14, 2021)

Grosfeld, K., Treffeisen, R., Asseng, J., Bartsch, A., Bräuer, B., Fritzsch, B., Gerdes, R., Hendricks, S., Hiller, W., Heygster, G., et al. (2016). Online sea-ice knowledge and data platform. *Polarforschung*, *85*(2), 143–155.

Guimarães, P. V., Ardhuin, F., Sutherland, P., Accensi, M., Hamon, M., Pérignon, Y., Thomson, J., Benetazzo, A., & Ferrant, P. (2018). A surface kinematics buoy (SKIB) for wave–current interaction studies. *Ocean Science*, *14*(6), 1449–1460.

Haas, C., & Nicolaus, M. (2016). *The international programme for antarctic buoys*. [Online]. Available at https://www.ipab.aq/ (Accessed February 28, 2021)

Hibler, W. D. (1979). A dynamic thermodynamic sea ice model. *Journal of Physical Oceanography*, *9*(4), 815–846.

Hogweard. (2015). *A map of antarctica and the surrounding oceans*. Wikimedia Commons. [Online]. Available at https://commons.wikimedia.org/wiki/File:Antarctica_and_the_Southern_Ocean.svg (Accessed February 13, 2021)

Hoppmann, M., Nicolaus, M., Hunkeler, P. A., & König-Langlo, G. (2015). Field measurements of the atmosphere, ocean, sea ice and sub-ice platelet layer at Atka Bay in 2013. *120*(3), 1703–1724.

Hošeková, L., Malila, M. P., Rogers, W. E., Roach, L. A., Eidam, E., Rainville, L., Kumar, N., & Thomson, J. (2020). Attenuation of ocean surface waves in pancake and frazil sea ice along the coast of the Chukchi sea. *Journal of Geophysical Research: Oceans*, *125*(12), e2020JC016746.

IEEE. (2017). IEEE Standard for System, Software, and Hardware Verification and Validation. *IEEE Std 1012-2016 (Revision of IEEE Std 1012-2012/ Incorporates IEEE Std 1012-2016/Cor1-2017)*, 1–260.

Inmarsat. (2021). *Stay connected*. Inmarsat. [Online]. Available at https://www.inmarsat.com/en/index.html (Accessed February 14, 2021)

Intel. (2015). *Intel® Edison Development Platform* [Product Brief]. [Online]. Available at https://www.intel.com/content/dam/support/us/en/documents/edison/sb/edison_pb_331179002.pdf

Intelsat. (2021). *Imagine here*. Intelsat. [Online]. Available at https://www.intelsat.com/ (Accessed February 14, 2021)

Iridium. (2021). *About us*. Iridium. [Online]. Available at https://www.iridium.com (Accessed February 14, 2021)

Iridium Satellite Communications. (2016). *Iridium® mobile satellite services [Brochure]*. [Online]. Available at https://www.iridium.com/iot-products/ (Accessed December 15, 2020)

Iridium Satellite Communications. (2019). *Iridium 9603*. [Online]. Available at https://www.iridium.com/products/iridium-9603/ (Accessed December 15, 2020)

Iridium Satellite Communications. (2020). *Iridium 9522b (end of life - nov19)*. [Online].

Available at https://www.iridium.com/products/iridium-9522b/ (Accessed December 15, 2020)

Iridium Satellite Communications. (2020). *Iridium 9602*. [Online]. Available at https://www.iridium.com/products/iridium-9602/ (Accessed December 15, 2020)

Iridium Satellite Communications. (2020). *Iridium® IoT product comparison [Brochure]*. [Online]. Available at https://www.iridium.com/file/24127/?dlm-dp-dl-force=1&dlm-dp-dl-nonce=5bb4c013b0 (Accessed December 15, 2020)

Jabbar, M. A. (2001). *Multi-link iridium satellite data communication system* (Msc. thesis). University of Kansas, Lawrence, USA.

Jordehi, A. R. (2016). Parameter estimation of solar photovoltaic (pv) cells: A review. *Renewable and Sustainable Energy Reviews*, *61*, 354–371.

Jwo, D.-J. (2001). Efficient DOP calculation for GPS with and without altimeter aiding. *The Journal of Navigation*, *54*(2), 269–279.

Kennicutt, M. C., Bromwich, D., Liggett, D., Njåstad, B., Peck, L., Rintoul, S. R., Ritz, C., Siegert, M. J., Aitken, A., Brooks, C. M., et al. (2019). Sustained Antarctic research: A 21st century imperative. *One Earth*, *1*(1), 95–113.

Kennicutt, M. C., Chown, S. L., Cassano, J. J., Liggett, D., Massom, R., Peck, L. S., Rintoul, S. R., Storey, J. W., Vaughan, D. G., Wilson, T. J., et al. (2014). Polar research: Six priorities for Antarctic science. *Nature News*, *512*(7512), 23.

Kennicutt, M. C., Kim, Y. D., Rogan-Finnemore, M., Anandakrishnan, S., Chown, S. L., Colwell, S., Cowan, D., Escutia, C., Frenot, Y., Hall, J., et al. (2016). Delivering 21st century Antarctic and Southern Ocean science. *Antarctic Science*, *28*(6), 407–423.

Kistler. (2011). *ServoK-Beam Accelerometer Force Feedback Capacitive Accelerometer* [a-03.11]. [Online]. Available at https://manualzz.com/doc/28248639/servok-beam-accelerometer

Kohout, A., Williams, M., Dean, S., & Meylan, M. (2014). Storm-induced sea-ice breakup and the implications for ice extent. *Nature*, *509*(7502), 604–607.

Kohout, A., Smith, M., Roach, L., Williams, G., Montiel, F., & Williams, M. (2020). Observations of exponential wave attenuation in Antarctic sea ice during the PIPERS campaign. *Annals of Glaciology*, *61*, 1–14.

Kohout, A. L., Penrose, B., Penrose, S., & Williams, M. J. (2015). A device for measuring wave-induced motion of ice floes in the Antarctic marginal ice zone. *Annals of Glaciology*, *56*(69), 415–424.

Kohout, A. L., Smith, M., Roach, L. A., Williams, G., Montiel, F., & Williams, M. J. M. (2020). Observations of exponential wave attenuation in Antarctic sea ice during the PIPERS campaign. *Annals of Glaciology*, *61*(82), 196–209.

Kuik, A., Van Vledder, G. P., & Holthuijsen, L. (1988). A method for the routine analysis of pitch-and-roll buoy wave data. *Journal of Physical Oceanography*, *18*(7), 1020–1034.

Lee, C. M., Cole, S., Doble, M., Freitag, L., Hwang, P., Jayne, S., Jeffries, M., Krishfield, R., Maksym, T., & Maslowski, W. (2012). Marginal Ice Zone (MIZ) program: Science and experiment plan (No. APL-UW 1201).

Lee, S., Wu, Y., & Mortari, D. (2016). Satellite constellation design for telecommunication in antarctica. *International Journal of Satellite Communications and Networking*, *34*(6), 725–737.

Lei, R., Gui, D., Heil, P., Hutchings, J. K., & Ding, M. (2020). Comparisons of sea ice motion and deformation, and their responses to ice conditions and cyclonic activity in the western arctic ocean between two summers. *Cold Regions Science and Technology*, *170*, 102925.

Leppäranta, M., Zhanhai, Z., Haapala, J., & Stipa, T. (2001). Sea-ice kinematics measured with GPS drifters. *Annals of Glaciology*, *33*, 151–156.

Lever, J. H., Ray, L. R., Streeter, A., & Price, A. (2006). Solar power for an antarctic rover. *Hydrological Processes*, *20*(4), 629–644.

Liquid Robotics. (2016). *The new economics of marine environmental monitoring*. Liquid Robotics.

Littelfuse. (2021). *Pr303j2 - pr series*. [Online]. Available at https://www.littelfuse.com/products/temperature-sensors/leaded-thermistors/interchangeable-thermistors/ultra-precision-pr/pr303j2.aspx (Accessed February 25, 2021)

Lund, B., Graber, H. C., Persson, P. O. G., Smith, M., Doble, M., Thomson, J., & Wadhams, P. (2018). Arctic sea ice drift measured by shipboard marine radar. *Journal of Geophysical Research: Oceans*, *123*(6), 4298–4321.

Maksym, T., Stammerjohn, S. E., Ackly, S., & Massom, R. (2012). Antarctic sea ice—: A polar opposite? *Oceanography*, *25*(3), 140–151.

Manimekalai, P., Harikumar, R., & Raghavan, S. (2013). An overview of batteries for photovoltaic (pv) systems. *International Journal of Computer Applications*, *82*(12).

Mansoor, M., Haneef, I., Akhtar, S., De Luca, A., & Udrea, F. (2015). Silicon diode temperature sensors—a review of applications. *Sensors and Actuators A: Physical*, *232*, 63–74.

Marquart, R., MacHutchon, K., Skatulla, S., Vichi, M., & Bogaers, A. (2019). Modelling the dynamics of ice in the Antarctic marginal ice zone. *In Proc. of the 25th International Conference on Port and Ocean Engineering under Arctic Conditions*.

Mazarakis, N. (2019, September 5). *Why Douglas sea state 3 should be eliminated from good weather clauses*. [Online]. Available at https://www.stormgeo.com/products/s-suite/s-routing/articles/why-douglas-sea-state-3-should-be-eliminated-from-good-weather-clauses/ (Accessed February 28, 2021)

Meng, X., Wang, J., & Han, H. (2014). Optimal gps/accelerometer integration algorithm for monitoring the vertical structural dynamics. *Journal of Applied Geodesy*, *8*(4), 265–272.

Metocean. (2016). UpTempO Iridium Data Collection. [Online]. Available at https://www.metocean.com/product/polar-isvp/ (Accessed January 17, 2021)

Meylan, M. H., Bennetts, L. G., & Kohout, A. L. (2014). In situ measurements and analysis of ocean waves in the Antarctic marginal ice zone. *Geophysical Research Letters*, *41*(14), 5046–5051.

NEO-7 U-Blox 7 GNSS modules data sheet. [Rev. R07]. (2014). [Online]. Available at https://www.u-blox.com/sites/default/files/products/documents/NEO-7_DataSheet_%28UBX-13003830%29.pdf

Oanda Corporation. (2021, January 22). *Currency converter*. [Online]. Available at https://www1.oanda.com/currency/converter/ (Accessed December 15, 2020)

ORBCOMM. (2021). *Africa's leader in internet of things solutions multi-network connectivity. leading edge devices. powerful applications.*. ORBCOMM. [Online]. Available at https://www.orbcomm.com/africa/ (Accessed February 14, 2021)

Parkinson, C. L. (2004). Southern ocean sea ice and its wider linkages: Insights revealed from models and observations. *Antarctic Science*, *16*(4), 387.

Planck, C. J., Whitlock, J., Polashenski, C., & Perovich, D. (2019). The evolution of the seasonal ice mass balance buoy. *Cold Regions Science and Technology*, *165*, 102792.
Planck, C. J., Whitlock, J., Polashenski, C., & Perovich, D. (2019). The evolution of the seasonal ice mass balance buoy. *Cold Regions Science and Technology*, *165*, 102792.
Polashenski, C., Perovich, D., Richter-Menge, J., & Elder, B. (2011). Seasonal ice mass-balance buoys: Adapting tools to the changing arctic. *Annals of Glaciology*, *52*(57), 18–26.

QStarz. (2013). *Bt-q1000ex*. [Online]. Available at http://www.qstarz.com/Products/GPS%20Products/BT-Q1000EX-10HZ-F.html (Accessed February 25, 2021)

Rabault, J. (2018). An investigation into the interaction between waves and ice. *arXiv preprint arXiv:1810.07022*.

Rabault, J., Sutherland, G., Gundersen, O., & Jensen, A. (2017). Measurements of wave damping by a grease ice slick in svalbard using off-the-shelf sensors and open-source electronics. *Journal of Glaciology*, *63*(238), 372–381.

Rabault, J., Sutherland, G., Gundersen, O., & Jensen, A. (2019). An open source, versatile, affordable waves in ice instrument for remote sensing in the polar regions. *arXiv preprint arXiv:1901.02410*.

Rabault, J., Voermans, J., Sutherland, G., Jensen, A., Babanin, A., & Filchuk, K. (2020). Development of open source instruments for in-situ measurements of waves in ice. *arXiv preprint arXiv:2003.02540*.

Roach, L. A., Dörr, J., Holmes, C. R., Massonnet, F., Blockley, E. W., Notz, D., Rackow, T., Raphael, M. N., O'Farrell, S. P., Bailey, D. A., et al. (2020). Antarctic sea ice area in cmip6. *Geophysical Research Letters*, *47*(9), e2019GL086729.

RS Components. (2021). *Nxp mpx5100ap*. [Online]. Available at https://ie.rs-online.com/web/p/pressure-sensor-ics/9227342/ (Accessed February 26, 2021)

Samaun, S., Wise, K., Nielsen, E., & Angell, J. (1971). An ic piezoresistive pressure sensor for biomedical instrumentation. *1971 IEEE International Solid-State Circuits Conference. Digest of Technical Papers*, *14*, 104–105.

Sarkar, S. (2018). A survey of new research directions in microprocessors.

Sea Bird Scientific. (2021). *Welcome to sea-bird scientific*. [Online]. Available at https://www.seabird.com/ (Accessed February 13, 2021)

Sea Technology Services. (2021). *Welcome to sea-bird scientific*. [Online]. Available at seatechnology.co.za (Accessed February 13, 2021)

Sharma, S., Jain, K. K., Sharma, A., et al. (2015). Solar cells: In research and applications—a review. *Materials Sciences and Applications*, *6*(12), 1145.

Simon, D. (2001). Kalman filtering. *Embedded systems programming*, *14*(6), 72–79.

SparkFun. (2017, April 20). *Gps receiver module smd - s1315f*. [Online]. Available at https://www.sparkfun.com/products/retired/14239 (Accessed February 25, 2021)

Spilker Jr, J. J., Axelrad, P., Parkinson, B. W., & Enge, P. (1996). *Global positioning system: Theory and applications, volume i*. American Institute of Aeronautics; Astronautics.

Steer, A. (2016). Sea ice earth systems [[Online; accessed December 16, 2020]]. [Online]. Available at https://github.com/adamsteer/adamsteer.github.io/blob/master/talks/phd.wrapup/images/seaice.earthsystem.png

Steer, A., Worby, A., & Heil, P. (2008). Observed changes in sea-ice floe size distribution during early summer in the western weddell sea [Ice Station POlarstern (ISPOL):

Results of interdisciplinary studies on a drifting ice floe in the western Weddell Sea]. *Deep Sea Research Part II: Topical Studies in Oceanography*, *55*(8), 933–942. https://doi.org/https://doi.org/10.1016/j.dsr2.2007.12.016

Studenovská, H., Lapcik, L., Bursikova, V., Zemek, J., & Barros-Timmons, A. (2003). Surface properties of polyethylene after low-temperature plasma treatment. *Colloid and Polymer Science*, *281*, 1025–1033. https://doi.org/10.1007/s00396-003-0871-8

Swart, S., du Plessis, M. D., Thompson, A. F., Biddle, L. C., Giddy, I., Linders, T., Mohrmann, M., & Nicholson, S.-A. (2020). Submesoscale fronts in the Antarctic marginal ice zone and their response to wind forcing. *Geophysical Research Letters*, *47*(6), e2019GL086649.

Tahsin, M., Sultana, S., Reza, T., & Hossam-E-Haider, M. (2015). Analysis of dop and its preciseness in gnss position estimation. *2015 International conference on electrical engineering and information communication technology (ICEEICT)*, 1–6.

TDK InvenSense. (2016). *MPU–9250 Product Specification* [Rev 1.1]. [Online]. Available at https://invensense.tdk.com/download-pdf/mpu-9250-datasheet/

Thomson, J. (2012). Wave breaking dissipation observed with "swift" drifters. *Journal of Atmospheric and Oceanic Technology*, *29*(12), 1866–1882.

Tong, A. (2001). Improving the accuracy of temperature measurements. *Sensor Review*, *21*(3), 193–198.

Trident Sensors. (2021). *Buoy Tracking Systems (2)*. [Online]. Available at https://www.tridentsensors.com/products/19-buoy-tracking-systems/21-buoy-tracking-2 (Accessed January 17, 2021)

Tuck, K. (2007). Tilt sensing using linear accelerometers. *Freescale semiconductor application note AN3107*.

Turner, J., Phillips, T., Marshall, G. J., Hosking, J. S., Pope, J. O., Bracegirdle, T. J., & Deb, P. (2017). Unprecedented springtime retreat of antarctic sea ice in 2016. *Geophysical Research Letters*, *44*(13), 6868–6875.

U-blox m9n standard precision module datasheet [Rev. R04]. (2020). [Online]. Available at https://www.u-blox.com/sites/default/files/NEO-M9N_DataSheet_%5C%28UBX-19014285%5C%29.pdf

U-Blox. (2020). *U-blox m9n standard precision module interface description* [Rev. R03]. [Online]. Available at https://www.u-blox.com/sites/default/files/NEO-M9N_Interfacedescription_%5C%28UBX-19035940%5C%29.pdf

USACE. (2014). [Online]. Available at https://www.erdc.usace.army.mil/Media/Fact-Sheets/Fact-Sheet-Article-View/Article/553850/crrel-ice-mass-balance-imb-buoy-program/

Vaisala. (2018). *Barocap barometer ptb110*. [Online]. Available at https://www.vaisala.com/sites/default/files/documents/PTB110-Datasheet-B210681EN.pdf (Accessed February 26, 2021)

Varvasovszky, Z., & Brugha, R. (2000). A stakeholder analysis. *Health policy and planning*, *15*(3), 338–345.

VECTORNAV. (2019). Vn-100 imu/ahrs high-performance embedded navigation.

Vichi, M., Eayrs, C., Alberello, A., Bekker, A., Bennetts, L., Holland, D., de Jong, E., Joubert, W., MacHutchon, K., Messori, G., et al. (2019). Effects of an explosive polar cyclone crossing the antarctic marginal ice zone. *Geophysical Research Letters*.

Vidal, C., Gross, O., Gu, R., Kollmeyer, P., & Emadi, A. (2019). Xev li-ion battery low-temperature effects. *IEEE transactions on vehicular technology*, *68*(5), 4560–4572.

Wadhams, P., Lange, M. A., & Ackley, S. F. (1987). The ice thickness distribution across the Atlantic sector of the Antarctic ocean in midwinter. *Journal of Geophysical Research: Oceans*, *92*(C13), 14535–14552.

Waveshare. (2016). *Uart gps module, NEO-7M-C Onboard, Straight/Vertical Pinheader*. [Online]. Available at https://www.waveshare.com/uart-gps-neo-7m-c-b.htm (Accessed March 6, 2021)

Welch, P. (1967). The use of fast fourier transform for the estimation of power spectra: A method based on time averaging over short, modified periodograms. *IEEE Transactions on audio and electroacoustics*, *15*(2), 70–73.

Willander, M., Friesel, M., Wahab, Q.-u., & Straumal, B. (2006). Silicon carbide and diamond for high temperature device applications. *Journal of Materials Science: Materials in Electronics*, *17*(1), 1–25.

Williams, T. D., Bennetts, L. G., Squire, V. A., Dumont, D., & Bertino, L. (2013). Wave–ice interactions in the marginal ice zone. part 1: Theoretical foundations. *Ocean Modelling*, *71*, 81–91.

Womack, A. C. S. (2020). *Atmospheric drivers of ice drift in the antarctic marginal ice zone* (Msc. thesis). University of Cape Town.

World Meteorological Organisation. (2010). *Manual on the global data-processing and forecasting system* (2010th ed., Vol. 1). World Meteorological Organisation.

Zhang, S., Xu, K., & Jow, T. (2003). The low temperature performance of li-ion batteries. *Journal of Power Sources*, *115*(1), 137–140.